PHOTONICS INSIGHTS

Electrically tunable optical metasurfaces

Fei Ding,*,† Chao Meng,*,† and Sergey I. Bozhevolnyi*
Centre for Nano Optics, University of Southern Denmark, Odense, Denmark

Abstract. Optical metasurfaces have emerged as a groundbreaking technology in photonics, offering unparalleled control over light–matter interactions at the subwavelength scale with ultrathin surface nanostructures and thereby giving birth to flat optics. While most reported optical metasurfaces are static, featuring well-defined optical responses determined by their compositions and configurations set during fabrication, dynamic optical metasurfaces with reconfigurable functionalities by applying thermal, electrical, or optical stimuli have become increasingly more in demand and moved to the forefront of research and development. Among various types of dynamically controlled metasurfaces, electrically tunable optical metasurfaces have shown great promise due to their fast response time, low power consumption, and compatibility with existing electronic control systems, offering unique possibilities for dynamic tunability of light–matter interactions via electrical modulation. Here we provide a comprehensive overview of the state-of-the-art design methodologies and technologies explored in this rapidly evolving field. Our work delves into the fundamental principles of electrical modulation, various materials and mechanisms enabling tunability, and representative applications for active light-field manipulation, including optical amplitude and phase modulators, tunable polarization optics and wavelength filters, and dynamic wavefront-shaping optics, including holograms and displays. The review terminates with our perspectives on the future development of electrically triggered optical metasurfaces.

Keywords: optical metasurfaces; electrical modulation; electro-optic materials; micro-electromechanical and nano-electromechanical systems.

Received Jun. 30, 2024; revised manuscript received Aug. 26, 2024; accepted Sep. 3, 2024; published online Sep. 27, 2024.

[DOI: 10.3788/PI.2024.R07]

1 Introduction

In the rapidly advancing field of photonics, optical metasurfaces have emerged as a groundbreaking technology, offering unparalleled control over light–matter interactions at the subwavelength scale with ultrathin surface nanostructures[1–28] and giving thereby birth to flat optics[12]. Optical metasurfaces, which are two-dimensional (2D) planar arrays of nanostructures (often called meta-atoms), manipulate optical fields through localized interactions, enabling functionalities that are challenging or downright impossible to achieve with traditional bulk optical components. These capabilities have propelled metasurfaces to the forefront of optical research leveraging the precise arrangement and design of meta-atoms to engineer the wavefront of light, with applications ranging from imaging and detection to display and information processing. In imaging, metasurfaces facilitate the development of flat lenses, known as metalenses, which deliver high-quality imaging without the bulk and weight associated with traditional lenses[29–48]. For detection, metasurfaces have advanced the creation of high-dimensional photodetectors, exploiting their capability to predictably and independently react to the phase, amplitude, polarization, and frequency of light at the nanoscale[49–64]. In display technology, metasurfaces enable flexible light-field modulation within ultracompact footprints, resulting in high resolution, fidelity, and capacity images[65–104]. Additionally, metasurfaces are pivotal in advancing information processing technologies, where they contribute to the development of compact, high-performance optical elements for photonic integrated circuits[105–120].

However, to date, most reported optical metasurfaces are static, featuring well-defined optical responses determined by their compositions and configurations set during fabrication, a circumstance that, in turn, severely limits their adaptability and responsiveness to dynamic environmental conditions or

*Address all correspondence to Fei Ding, feid@mci.sdu.dk; Chao Meng, chao@mci.sdu.dk; Sergey I. Bozhevolnyi, seib@mci.sdu.dk.

†These authors contributed equally to this work.

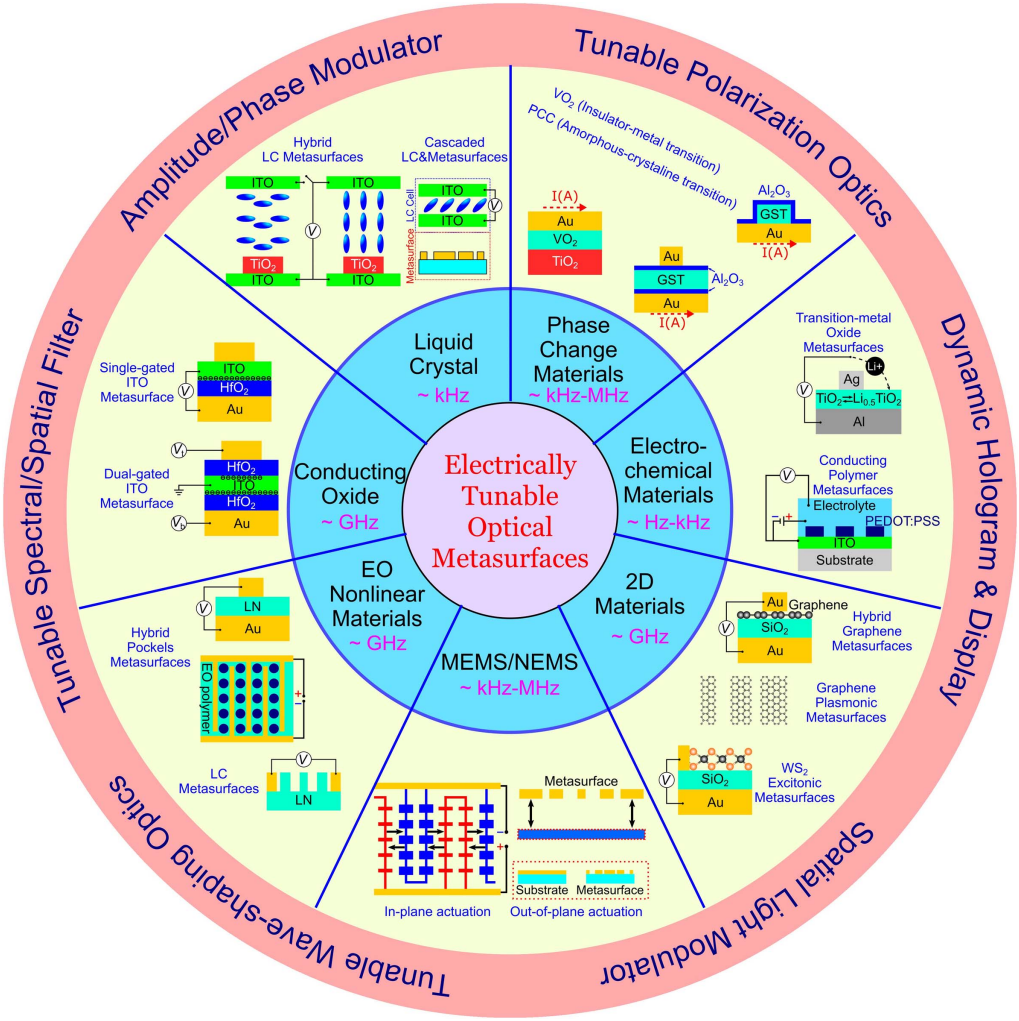

Fig. 1 Overview of electrically tunable optical metasurfaces: materials, configurations, and applications.

changing operational requirements. For more advanced integrated optical systems exploited in diverse applications, it would be highly desirable to develop dynamic optical metasurfaces with externally controlled, reconfigurable functionalities. To address this challenge, researchers have been exploring various strategies to introduce tunability and reconfigurability into metasurface functionalities[121–128]. Among these diverse strategies, electrically triggered optical metasurfaces have shown great promise due to their fast response time, low power consumption, and compatibility with existing electronic control systems. Electrically tunable metasurfaces leverage external electric fields to dynamically modify their optical responses by integrating metasurfaces with active electro-optic (EO) material compositions, whose refractive indices can be altered electrically, such as liquid crystals (LCs)[129–132], phase-change materials (PCMs)[133–138], transition metal oxides (TMOs)[135,139–141], conducting polymers[142–144], 2D materials[145–151], transparent conducting oxides (TCOs)[152–155], or EO nonlinear materials[156–159]. Alternatively, tunable metasurfaces can also be implemented by integrating with micro-electromechanical and nano-electromechanical systems (MEMS and NEMS)[160–162]. In these configurations, the optical properties of tunable metasurfaces can be controlled and modulated in real time with externally applied electrical fields, thereby enabling a wide range of dynamic functionalities (Fig. 1).

Our review offers a thorough and detailed examination of current advancements in electrically tunable optical metasurfaces. Delving into the fundamental principles underlying electrical modulation, we explore the diverse materials and mechanisms employed to achieve the tunability of metasurface operation and highlight the principal applications in active light-field manipulation, including amplitude and phase modulators, tunable polarization optics and wavelength filters, dynamic wave-shaping optics (beam steering and tunable meta-lenses), dynamic hologram and displays, as well as metasurface-based spatial light modulators. Regarding future perspectives, our review concludes by considering the challenges faced in this swiftly advancing field and proposing potential directions for further research and development.

2 Electrically Tunable LC Metasurfaces

To achieve dynamic optical metasurfaces, researchers have been exploring the integration of LCs with metasurfaces. LCs are a unique state of matter that exhibits properties between

conventional liquids and solid crystals[129–131]. Their molecular orientation can be precisely controlled using external stimuli such as electric fields, temperature, light, or pressure. This controllability allows LCs to dynamically modulate their refractive index, making them ideal candidates for creating reconfigurable and tunable optical devices. The combination of LCs and metasurfaces—referred to as LC metasurfaces—promises a new class of optical devices that are not only compact and efficient but also highly versatile and reconfigurable, opening possibilities for real-time applications in various fields such as adaptive optics, augmented reality, optical communications, and more [132]. In LC metasurfaces, the LCs can serve multiple roles: they can modify the dielectric environment of metasurfaces, complement the optical properties of metasurfaces, act as tunable wave plates, or directly function as meta-atoms through their anisotropic nature. By applying external stimuli, the orientation of LC molecules can be changed, leading to the dynamic control of the optical responses of metasurfaces. Numerous functionalities, such as reconfigurable color displays, dynamic beam steering, varifocal lenses, and tunable holographic displays, have been successfully demonstrated.

2.1 Electrically Tunable LC Metasurfaces by Complementing Meta-Atoms' Properties with LCs

Integrating LCs and homogeneous meta-atoms can enhance device performance, creating new capabilities. For instance, LC metasurfaces can enable spectral tuning to generate tunable structural colors[65,123,163]. By electrically adjusting the LC orientation, the reflected[164] or transmitted[165–167] colors can be dynamically varied to cover a wide range of the color palette. Franklin *et al.* introduced a reflective LC-plasmonic system that achieved full red-green-blue (RGB) color modulation by applying electric fields, as shown in Fig. 2(a)[164]. The reflective plasmonic nanostructure consists of an aluminum (Al) array, roughened to induce polarization-dependent plasmonic resonance. The LCs used in the device are high-birefringence LCs, which are crucial for modulating the effective refractive index of the plasmonic modes. The LC orientation is controlled by applying an electric field across the device, enabling the tuning of plasmonic resonances and dynamic control over the color of reflected light, covering the entire RGB spectrum. Based on nanoimprint lithography, the researchers were able to produce large-area, cost-effective samples, with the potential for scaling up to hand-held or notebook-sized displays. The as-fabricated device exhibits two distinct color states based on the polarization of incident light arising from the roughened surface morphology of the Al nanostructures. When an electric field is applied, the orientation of LC molecules changes, leading to a change in the effective refractive index of plasmonic modes. At low voltages, bulk LC reorientation occurs, resulting in polarization rotation and the superposition of the device's two orthogonal off-state modes. As the voltage increases, the LC molecules near the surface reorient, causing a red shift in the plasmonic resonance. Eventually, at high voltages, the LC molecules achieve vertical alignment, resulting in a saturation state where the color shifts to green and loses polarization dependence. They also showed the ability to achieve a full RGB color basis set through a combination of bulk and surface LC effects, which manipulate the phase retardation and polarization state of the incident light. By carefully controlling the voltage applied across the device, the researchers could transition the color of reflected light from red to blue or blue to red, with the highest voltage resulting in green [Fig. 2(a)], demonstrating the potential for high-resolution, full-color displays. As the spectrum shifts, the resonant strength changes, leading to various applications in amplitude modulation[168–172]. Staude's group reported electrically tunable transparent displays operating at visible, leveraging the unique properties of Mie-resonant silicon (Si) metasurfaces[21,173] and LCs to achieve dynamic optical control[169]. To ensure high-quality pre-alignment of the LC molecules, they applied photoalignment material AtA-2 to both the upper electrode and the fabricated Si metasurface, significantly enhancing the homogeneity and tuning accuracy of the device without damaging the metasurface structures. By applying a voltage across this LC metasurface cell, they could observe pronounced spectral shifts in the metasurface resonances, transitioning the metasurface in and out of the Huygens' regime, characterized by high transparency and efficient light manipulation. Notably, they achieved a maximum modulation depth of 53% at an operation wavelength of 669 nm with an applied voltage of 20 V. A practical display functionality was demonstrated by replacing the upper electrode with a patterned electrode forming the letters "FSU-ANU". The device exhibited pronounced modulation of transmitted light, with the letters becoming visible and more pronounced as the voltage increased, as displayed in Fig. 2(b).

Besides amplitude modulation, phase modulation and even phase-only spatial light modulators (SLMs) have also been demonstrated using LC-integrated homogeneous meta-atoms[168,174,175]. In 2019, Kuznetsov's group proposed a novel approach that combines dielectric metasurfaces with LCs to create a high-resolution, phase-only transmissive SLM capable of active beam steering with miniaturized pixel sizes[174]. Compared to traditional LC-based SLMs that achieve phase modulation only through the reorientation of LC molecules within thicknesses of several micrometers, intrinsically limited by large pixel sizes, mutual crosstalk between pixels, and high driving voltages, the metasurface-based SLM has significantly reduced pixel sizes and improved modulation capabilities. The metasurface SLM is designed based on Huygens' principle, where spectrally overlapped electric and magnetic dipole resonances are supported by disc nanoantennas made up of titanium dioxide (TiO_2), a popular material for visible metasurfaces due to its high refractive index and low absorption coefficient[40,74,176–179]. By applying a voltage to modify the LC orientation around nanoantennas, they observed significant spectral shifts in the metasurface resonances, resulting in sufficiently large phase modulation with reduced LC cell thickness and pixel sizes. Specifically, the device demonstrated evenly spaced phase retardation of approximately $2\pi/3$ between different LC orientations (i.e., 0°, 45°, and 90°), with high transmission efficiency within the range of 60%–90%, enabling a three-level-addressing possibility. The fabricated metasurface SLM comprises 28 individually addressable electrodes, each independently controlling the LC orientation of a pixel with three TiO_2 nanoantennas. Using three-phase-level addressing schemes, they successfully implemented dynamic beam steering with tunable deflection angles up to 11° at the working wavelength of 650 nm. To address the limitations associated with a small sample size, a larger device was designed. While this device is restricted to reversing the deflection direction and cannot adjust the deflection angle, it significantly enhances deflection efficiency, achieving a rate of 36% at 660 nm, as shown in

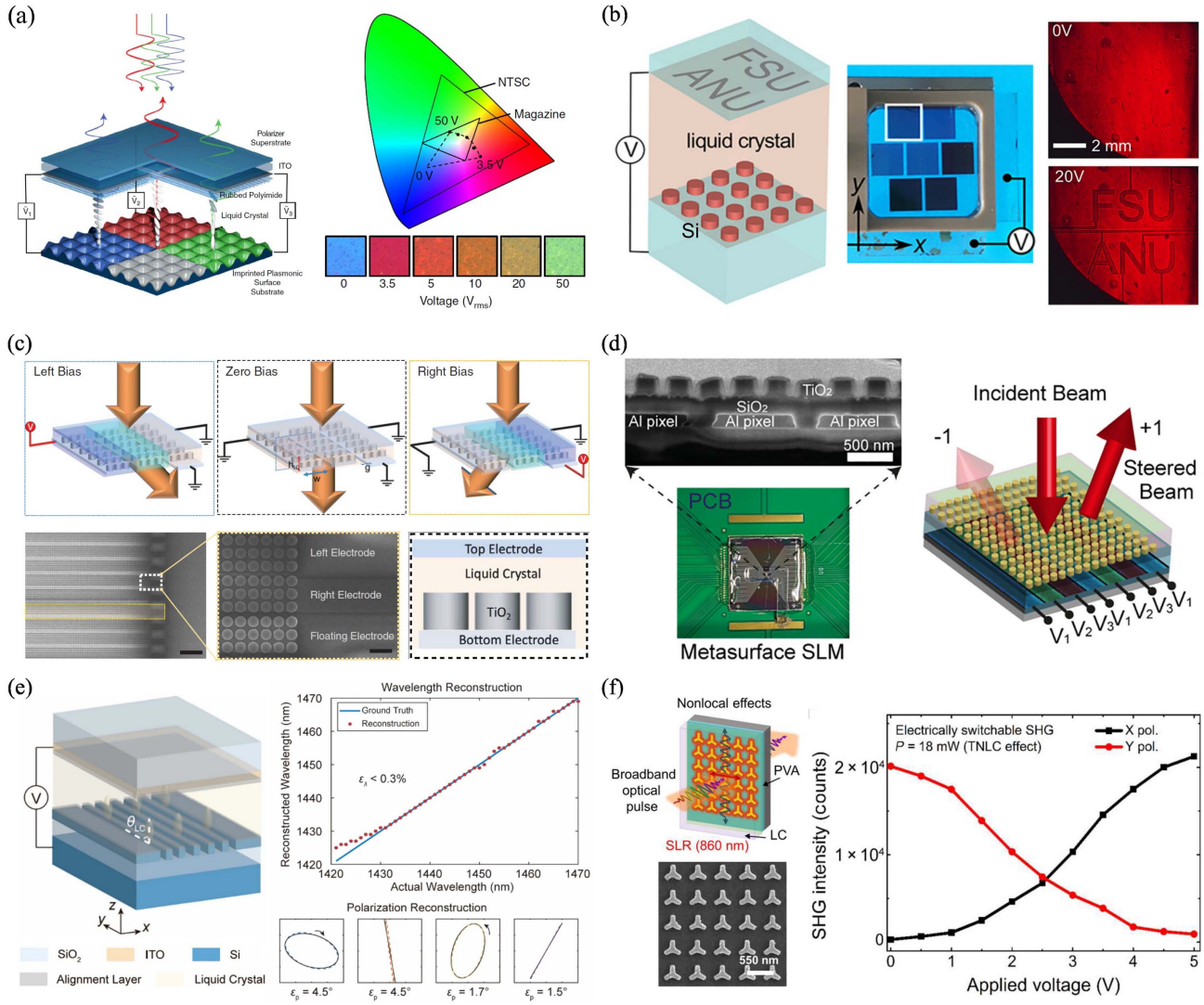

Fig. 2 Electrically tunable LC metasurfaces based on homogeneous meta-atoms. (a) LC-integrated tunable full-color plasmonic display. The LC-plasmonic system produces the RGB color basis set as a function of voltage. The letters appear and gradually become darker when the voltage increases from 0 to 20 V. Adapted with permission from Ref. [164] © Springer Nature. (b) LC-integrated Si metasurface for electrically tunable transparent display. Adapted with permission from Ref. [169] © American Chemical Society (ACS). (c) Electrically tunable transmissive metasurface SLM with three-level phase modulation for reversing deflection angles. Adapted with permission from Ref. [174] © the American Association for the Advancement of Science (AAAS). (d) Electrically tunable reflective metasurface SLM with continuous and full-phase modulation programmable beam steering. The incident light is diffracted preferentially into the $+1$ order when applied with a three-level voltage to create a supercell. Adapted with permission from Ref. [175] © ACS. (e) Tunable LC metasurface for computational spectropolarimetry. The reconstructed wavelengths and polarization states of the incident monochromatic light from 1420 to 1479 nm perfectly match the ground truth. Adapted with permission from Ref. [62] © Springer Nature. (f) Electrically switchable nonlocal metasurfaces for SHG. The second-harmonic intensity varies with applied voltages. Adapted with permission from Ref. [181] © AAAS.

Fig. 2(c). Although the study represents a significant advancement in the development of high-resolution, phase-only transmissive SLMs, it requires a thicker LC cell and cannot enable continuous and full-phase modulation, which, in turn, limits their functionalities and efficiencies. In 2023, Kuznetsov's group presented a groundbreaking solution by integrating a thin LC layer with a metasurface to realize a reflective metasurface SLM with full-phase modulation and high reflectivity in the visible spectrum[175]. As shown in Fig. 2(d), the metasurface SLM consists of a reflective design incorporating a bottom Al layer, a silicon dioxide (SiO_2) spacer, and a TiO_2 metasurface topped with an ultrathin LC layer of 500 nm. This design ensures high reflection

while facilitating continuous phase tuning from 0 to 2π by rotating the LC directors from an in-plane to an out-of-plane orientation, which modifies the refractive index seen by the incident light. The metasurface achieved a near-complete 2π phase shift with high reflectance at a wavelength of 650 nm, primarily due to the spectral tuning of the metasurface resonance induced by changes in LC orientation upon applying a voltage. Meanwhile, the reflectance remained above 50% throughout the phase tuning range, highlighting the efficiency of the design. By programming 96 individually addressable electrodes with a small pixel pitch of ~1 μm, the SLM demonstrated dynamic beam steering with a wide field of view (FOV) of up to 22°. Impressively, the beam steering efficiency reached up to 50%, among the highest reported for such devices, with minimal crosstalk between pixels due to the ultrathin LC cell.

Apart from amplitude and phase, polarization, as one of the intrinsic properties of light[180], can be manipulated and detected with LC-integrated homogeneous metasurfaces. Recently, Yang's group demonstrated a tunable LC metasurface capable of accurately measuring the polarization and spectrum of light with minimal hardware complexity[62]. As shown in Fig. 2(e), the metasurface consists of a one-dimensional (1D) Si grating embedded in an LC layer, which is covered with a transparent indium tin oxide (ITO) electrode for active modulation. The metasurface supports high-quality-factor (Q-factor) guided-mode resonances (GMRs) with rich spectral and polarization features that can be widely tuned by applying different bias voltages. The LC metasurface, combined with a polarizer and photodetector, transforms the Stokes vector that describes the state of polarization through a Mueller matrix, which depends on the wavelength and applied voltage. By sequentially altering the voltage applied to the LC metasurface, the system encoded the polarization and spectrum information into a series of intensity measurements. These measurements are then computationally reconstructed using a nonlinear least square fitting algorithm to retrieve the full Stokes parameters and the spectrum of the incident light. Simulations showed that the metasurface could accurately reconstruct the polarization state and the wavelength of the monochromatic incident light, even in the presence of noise. The polarization reconstruction error was found to be less than 5°, and the wavelength reconstruction error was below 0.5% with a signal-to-noise ratio (SNR) of 10 dB under no more than 10 measurements. The fabricated spectropolarimeter successfully reconstructed the polarization state and wavelength of the incident light, with the reconstructed peak positions and bandwidths agreeing well with the ground truth. Specifically, the system demonstrated the ability to reconstruct narrowband spectra with high accuracy (>99.7%) in the wavelength range from 1420 to 1470 nm with a separation of 1 nm, as shown in Fig. 2(e). The integration of a tunable LC metasurface with computational reconstruction techniques presents a significant advancement in the field of spectropolarimetry. The proposed system offers several advantages over traditional methods, such as compactness, high fidelity, and flexibility. However, the study also identified areas for improvement. The experimental spectral resolution was lower than predicted by simulations, likely due to fabrication imperfections and inhomogeneous LC alignment. Future work could focus on enhancing the Q-factor of the resonances, reducing system noise, and optimizing the metasurface design to improve performance.

In addition to LC-integrated linear metasurfaces, the integration of nonlinear metasurfaces with LCs presents a promising approach for developing actively tunable nonlinear optical devices. Sharma *et al.* explored the dynamic tuning of nonlocal second-harmonic generation (SHG) using a hybrid metasurface integrated with a twisted nematic LC layer[181]. The designed metasurface consists of 30 nm thick gold (Au) meta-atoms with threefold rotational symmetry, arranged in a square lattice with a period of 550 nm, which supports a strong nonlocal surface lattice resonance (SLR) mode at a fundamental wavelength of 860 nm for x-polarized incident light, resulting in polarization-selective SHG. The metasurface was fabricated on an ITO-coated glass substrate and encapsulated in a thin (~6 μm) LC cell. By increasing the applied voltage from 0 to 5 V, the LC molecules align in the z-direction, modulating the second harmonic (SH) signal with a large extinction ratio of >25 dB, originating from the alignment-induced changes in the effective refractive index, which shifts the SLR wavelength and thereby the SH signal. As shown in Fig. 2(f), the SH signals under x- and y-polarized excitation vary gradually when the applied voltage increases from 0 to 5 V. The SHG signal can also be all-optically controlled, with an abrupt enhancement observed at a threshold power of 30 mW due to the isotropic-to-nematic phase transition.

To offer greater flexibility and functionality for advanced applications, it is crucial to integrate LCs with phase-gradient metasurfaces composed of inhomogeneous meta-atoms. Gorkunov *et al.* successfully combined LCs with superperiodic polyimide metasurfaces to achieve efficient, electrically controllable anomalous refraction, as depicted in Fig. 3(a)[182]. Traditional metasurfaces typically rely on periodic arrangements of sub-wavelength elements to design basic building blocks and achieve desired optical functionalities. In contrast, the superperiodic design enhances this by creating unit cells composed of variously sized stripes, which induce distinct LC alignments. A semi-analytical approach was employed to model the formation of LC modulations and their optical performance, providing valuable insights into factors affecting anomalous refraction efficiency, such as LC orientational elasticity and optical anisotropy. The fabricated metasurfaces could deflect up to 60% of incident light into a specific oblique direction, superior to simpler periodic LC metasurfaces, which typically achieve much lower diffraction efficiencies. By applying a voltage across the LC layer, the metasurface could be switched between refracting and transmitting states within a few milliseconds. Impressively, the 10 μm periodic LC metasurface maintained a refraction efficiency above 50% across the wavelength range from 400 to 535 nm. This broadband and fast-switching performance is essential for applications requiring real-time control over light propagation. Using LC mixtures with higher optical anisotropy could enhance metasurface performance, allowing for sharper and deeper phase profiles. To increase the switching efficiency and deflection angle, Chung and Miller employed a large-scale computational inverse design approach to theoretically design an LC metasurface for beam steering[183]. By leveraging adjoint-based local optimization and particle-swarm-based global optimization, they achieved high-efficiency resonant behavior in multiple states, a feat that is difficult to achieve with intuition-based design approaches. For example, a single-grating Si metasurface could achieve diffraction efficiencies of 71% in the voltage-on state and 52% in the voltage-off state, with transmission-normalized (TN) efficiencies of 86% and 63%, respectively. This design showed a switching efficiency of 48%, significantly higher than previous designs.

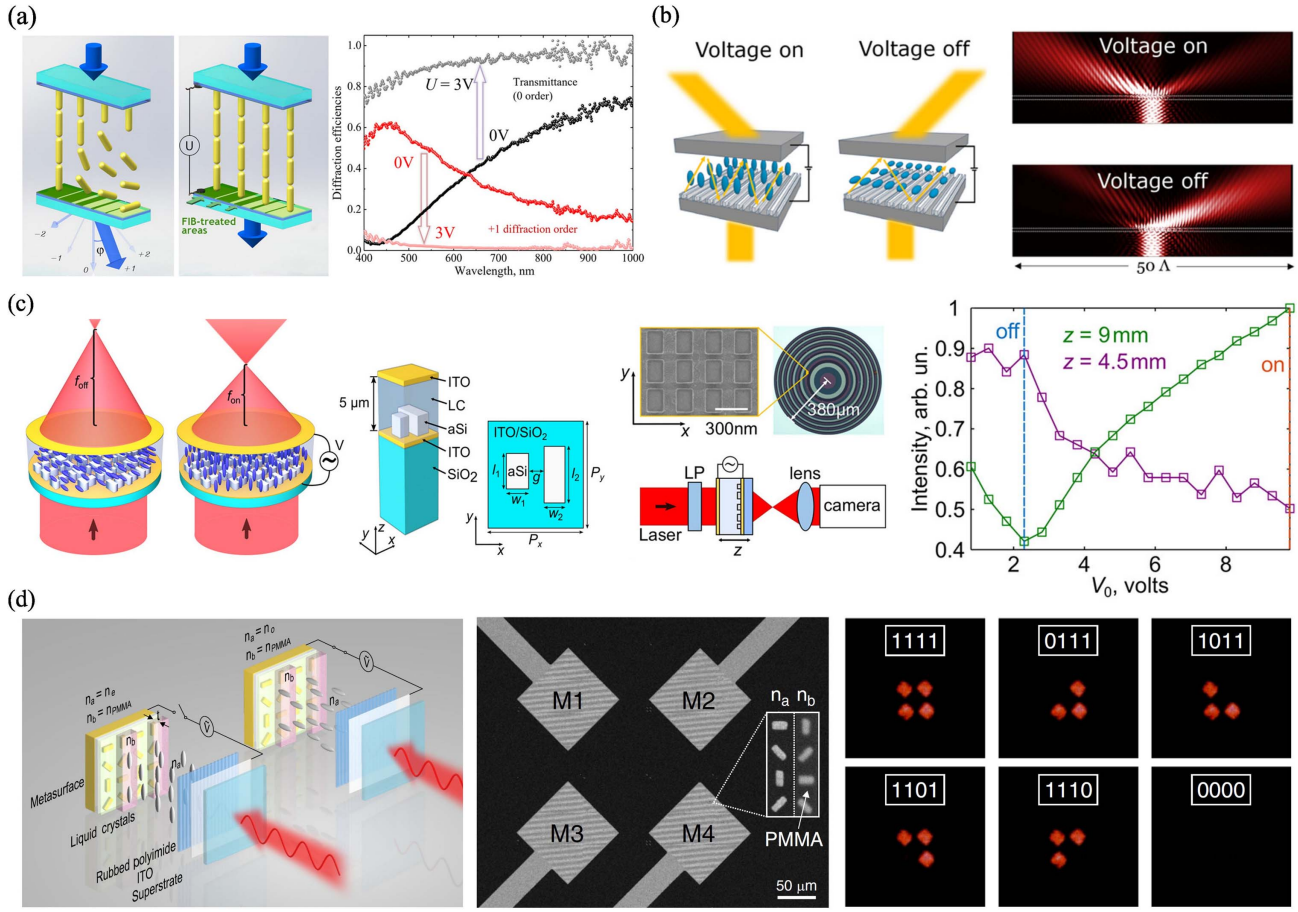

Fig. 3 Electrically tunable LC metasurfaces based on inhomogeneous meta-atoms. (a) Superperiodic LC metasurfaces for electrically controlled anomalous refraction. The device switches from anomalous refraction to direct transmission with an applied voltage of 3 V. Adapted with permission from Ref. [182] © ACS. (b) Inverse-designed LC metasurfaces for high-efficiency, large-angle, and tunable deflection. Adapted with permission from Ref. [183] © ACS. (c) LC-integrated varifocal metalens. The focal length continuously varies from 4.5 to 9 mm with an applied voltage. Adapted with permission from Ref. [184] © ACS. (d) Electrically controlled 4-bit DMSD for programmable displays. The programmable information sequence is dynamically generated by the DMSD. Adapted with permission from Ref. [191] © Springer Nature.

For higher efficiency and larger deflection angles, they developed a triple-grating Si metasurface with diffraction efficiencies of 78% (82% TN) in the voltage-on state and 78% (90% TN) in the voltage-off state, with a switching efficiency of 76%. Another design for ultra-wide-angle deflection (±72°) exhibited diffraction efficiencies of 62% and 76%, with TN efficiencies of 70% and 90%, respectively, as shown in Fig. 3(b). These high-efficiency designs are supported by dual-resonance structures with moderate Q-factor resonances in both operational states. The Q-factors were found to correlate with diffraction efficiencies, suggesting that high-Q-factor resonances are essential for achieving high performance.

By combining the resonance phase of metasurfaces with the tunable anisotropy of LCs, Shcherbakov and Shvets realized an electrically controllable LC-integrated metalens with continuously adjustable focal lengths[184]. As shown in Fig. 3(c), the proposed varifocal metalens adopts a Fresnel zone plate configuration, which divides the lens into concentric rings, each contributing to the phase modulation required to achieve the focusing functionality. The LC-encapsulated meta-atoms impart specific phase delays to incident light due to the supported electric and magnetic resonances[21,173], which can be adjusted by changing the orientation of the surrounding LC molecules *via* an applied voltage. The meta-atoms were optimized to provide a continuous and linear phase response as a function of the LC orientation, which is crucial for achieving smooth focal length adjustments. Simulations demonstrated that the varifocal metalens could achieve a continuous shift in focal length from 12 to 15 mm by varying the voltage applied to the LC layer. The fabricated bifocal metalens demonstrated high-contrast switching between two discrete focal lengths (9 and 4.5 mm) upon a voltage bias of $V_{PP} = 9.8$ V. The focal length could be smoothly adjusted by varying the applied voltage, demonstrating the feasibility of continuous varifocal tuning. The experimental results showed focusing efficiencies of 12.1% and 13.6% for the OFF and ON states, respectively, comparable to the simulation results. The Strehl ratios, which measure the quality of the focal spots, ranged from 0.72 to 0.83, indicating

near-diffraction-limited performance. The demonstrated varifocal metalens addresses the limitation of traditional varifocal lenses that rely on mechanical actuation, offering faster tuning speeds and scalability for various modern imaging applications. However, the efficiency needs to be further improved.

LCs and phase-gradient metasurfaces can be judiciously designed to provide complementary phase modulation. For instance, a metasurface can provide a geometric or Pancharatnam–Berry (PB) phase[185–190] while an LC layer adds a tunable transmission phase, enabling complex wavefront shaping[191,192]. In 2020, Liu's group demonstrated an electrically controlled digital metasurface device (DMSD) for dynamic image displays, as depicted in Fig. 3(d)[191]. The DMSD consists of an array of metasurface pixels, each of which can be individually addressed and reconfigured. Each pixel is composed of Au nanorods separated from an Au electrode by a PC403 spacer, with alternating columns covered by birefringent LCs with a refractive index of n_a and PMMA with a refractive index of n_b, where n_a can be dynamically changed via an applied electric field across the LCs and n_b is fixed. The rotated Au meta-atoms supply geometric phase and thus generate anomalous reflection in a specific direction, while the relative propagation phase between odd and even columns of the metasurface array can be dynamically controlled by varying the applied voltage, enabling dynamic control over the reflection and transmission properties of the metasurface. The fabricated DMSD prototype demonstrated excellent performance in terms of high-contrast light modulation (modulation ratio of 105:1), rapid switching within the millisecond time range, and good reversibility. Additionally, the four metasurface pixels could be independently addressed by activating corresponding electrodes, enabling 4-bit optical information programming. Moreover, this type of DMSD can generate and switch between arbitrary holographic patterns in real time, offering new possibilities for dynamic holography and optical information encryption. Based on this design principle, they achieved dynamic polarization conversion at visible wavelengths[192]. The dynamic functionality of the metasurface is achieved by electrically controlling the refractive index of the LC layer. The incident linearly polarized light undergoes phase modulation upon interaction with the metasurface, resulting in the generation of left-handed circularly polarized (LCP) and right-handed circularly polarized (RCP) light propagating along different directions. The phase delay between the output LCP and RCP light can be tuned by adjusting the applied voltage, enabling rapid and reversible polarization rotation up to 90° at 633 nm wavelength. By varying the applied voltage from 4 to 20 V, the polarization orientation of the reflected light could be dynamically tuned from 90° and 0°.

2.2 Electrically Tunable LC Metasurfaces with LCs Independently Acting as Tunable Wave Plates

In addition to complementing the optical properties of meta-atoms, LCs can function independently as tunable wave plates positioned either before[193–204] or after[205–209] polarization-multiplexed metasurfaces, promising advanced compound optical devices with high reconfigurability and versatility. In the following, we will discuss several examples of integrating independent LCs before multiplexed metasurfaces to achieve rapid switching between different functionalities.

Rho's group demonstrated an LC-empowered Si metasurface for electrically tunable color gradients and dark blacks[193]. As shown in Fig. 4(a), the device involves integrating an anisotropic elliptical-shaped Si meta-atom array with an LC cell, where the Si meta-atoms produce strong Mie scattering *via* lattice-induced quasi-GMRs and the LC layer is used to modulate the incident linear polarization, resulting in dynamic tuning between bright colors and dark blacks. The fabricated LC metasurfaces demonstrated a pronounced dependency on linear polarization. When the linear polarization was adjusted from 0° to 90°, the reflectance was dramatically modulated, resulting in dark black states when the scattering conditions were unfavorable. Additionally, high-resolution color prints with high contrast and vivid colors were achieved by segmenting grayscale images into multiple linear polarization zones, each occupied by meta-atoms with particular orientations to achieve the desired reflectance. The image brightness was electrically tuned from dark black to bright colors using an external electric field from 0 to 3.0 V/μm. By designing meta-atoms with varying dimensions within the same periodic structure, the researchers generated multicolored images that could be switched between visible and hidden states through LC-empowered linear polarization modulation [Fig. 4(a)]. The ability to dynamically tune the color with high contrast and resolution may open new possibilities for spectrum detection, high-performance displays, and advanced security systems. Guo *et al.* proposed a color filter for dynamic color tuning and spectral imaging, comprising a dichroic metagrating Fabry–Perot (FP) cavity and an LC cell[194], as illustrated in Fig. 4(b). The FP cavity features a thin silver (Ag) film at the bottom, a SiO_2 insulator layer in the middle, and Ag metagratings on top, which produces distinct transmissive colors for different polarizations. The LC cell, aligned parallel to the FP cavity, functions as a phase retarder to dynamically modulate the input polarization. The fabricated color filter enables a resonance shift of ∼300 nm by altering the input polarization *via* the LC cell. Consequently, the color appearance can be tuned from blue to deep red by varying the applied voltage. This broad tuning range covered the entire visible spectrum, demonstrating the device's capability for dynamic structural color applications. In addition, the filter was experimentally employed for spectral imaging of narrowband signals and colorful objects, achieving a spectral resolvability of around 10 nm, with the peak wavelength inaccuracy smaller than 5 nm. The device successfully reconstructed the spectra and images with high fidelity, indicating minimal color fading and noise.

Reconfigurable multifunctional metalenses have been demonstrated by combining polarization-encoded metalenses with independent LCs[195–198]. In particular, a tunable polarization-multiplexed achromatic dielectric metalens integrated with twisted nematic LCs in the visible spectrum was proposed by Duan and Hu[197], as shown in Fig. 4(c). The metalens is designed to achieve achromatic focusing and tunable focal lengths, addressing the chromatic aberration issue in conventional metalenses. The metalens is constructed from TiO_2 nanostructures with different cross-sectional shapes, arranged to achieve the desired phase profiles under two orthogonal polarization channels across multiple wavelengths. To ensure efficient broadband achromatic performance, a particle swarm optimization algorithm was adopted to optimize the nanostructures to minimize the matching error in phase compensation. The LC cell, consisting of LC molecules confined between orthogonally oriented alignment layers, converts the polarization of incident light. The fabricated metalens demonstrated achromatic focusing with minimal chromatic aberration across the visible spectrum from

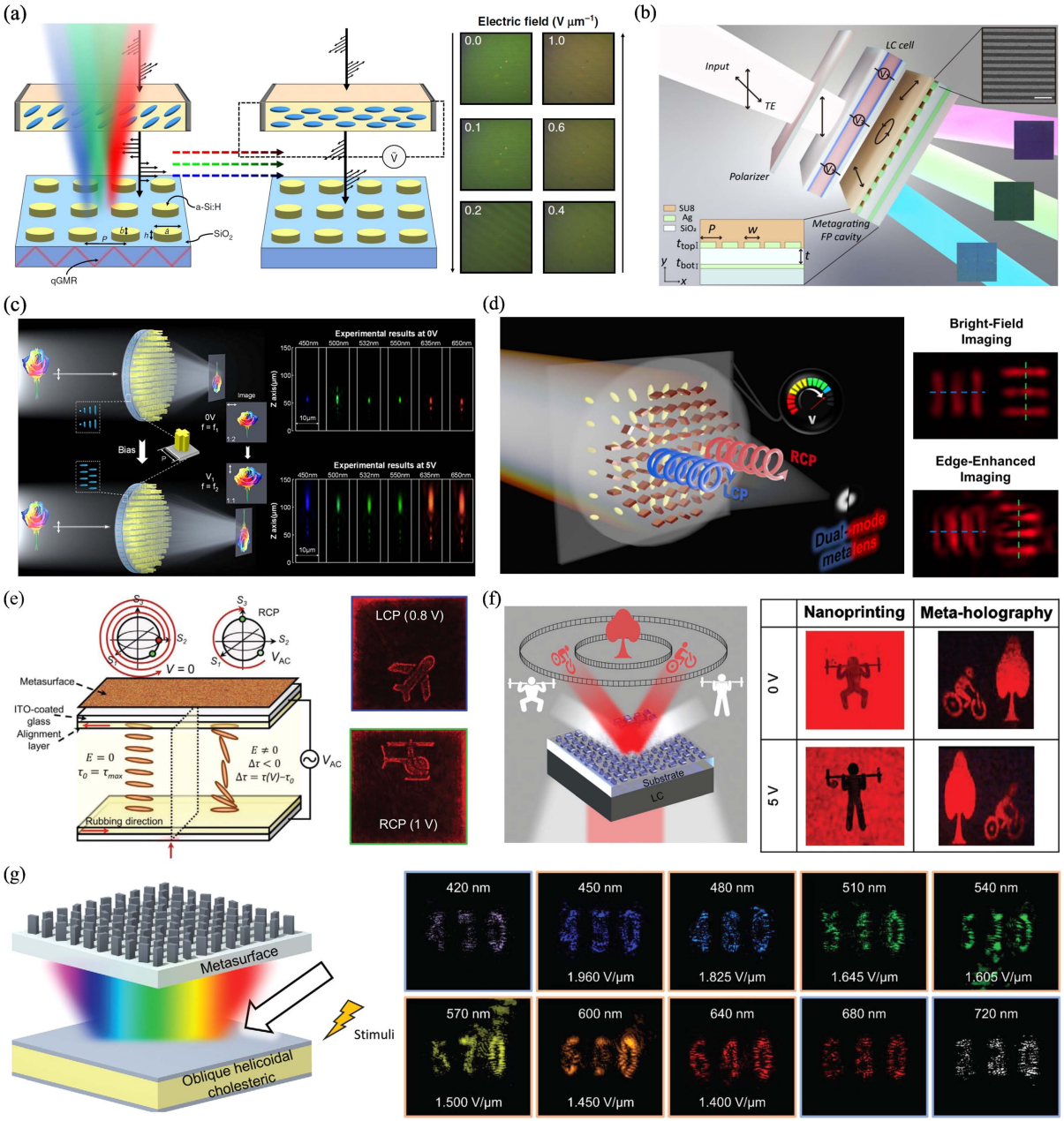

Fig. 4 Electrically tunable LC metasurfaces with independent LCs positioned before metasurfaces. (a) Electrically tunable structural color by combining an LC cell and an elliptical meta-atom array hosting enhanced Mie scattering via lattice-induced quasi-GMRs. The color is gradually modulated from green to magenta by adjusting the applied voltages to the LC cell. Adapted with permission from Ref. [193] © Springer Nature. (b) LC-driven metagrating FP color filter. Adapted with permission from Ref. [194] © the Electromagnetics Academy. (c) Polarization-multiplexed tunable achromatic metalens using twisted nematic LCs. The focal length shifts from 50 to 100 μm once the applied voltage changes from 0 to 5 V. Adapted with permission from Ref. [197] © ACS. (d) LC-integrated metalens for electrically switchable bright-field and edge-enhanced imaging. Adapted with permission from Ref. [198] © ACS. (e) Stimuli-responsive dynamic meta-holographic displays enabled by an LC modulator. The voltage-dependent display was realized in different polarization states. Adapted with permission from Ref. [199] © John Wiley and Sons. (f) Electrically driven LC meta-optics for simultaneous near-/far-field multiplexing display. Nanoprinting and meta-holography can be switched by changing the applied voltage. Adapted with permission from Ref. [202] © John Wiley and Sons. (g) Dynamic hyperspectral holography enabled by inverse-designed metasurfaces with LCs. Multicolor holographic images were realized by varying the applied electric field. Adapted with permission from Ref. [204] © John Wiley and Sons.

450 to 650 nm. By varying the applied voltage from 0 to 5 V, the focal length was dynamically tuned from ∼55 to ∼105 μm, enabling zoom imaging. Notably, the metalens achieved high focusing efficiency across the operational wavelength range. Apart from tunable achromatic lenses, customized dispersion-manipulated metalenses and color metaholograms could be implemented as well. Capitalizing on a spin-decoupled amorphous Si (α-Si) metalens integrated with an LC cell, Rho's group achieved real-time switching between bright-field and edge-enhanced imaging modes within milliseconds, as shown in Fig. 4(d)[198]. The metalens incorporates both geometric and propagation phases to encode two phase profiles: a hyperbolic phase for bright-field imaging and a spiral phase with a topological charge of +1 for edge-enhanced imaging. The rectangular a-Si meta-atoms, with varying dimensions and rotations, function as nanoscale half-wave plates (HWPs) that convert incident circularly polarized (CP) light from LCP to RCP and vice versa. The LC cell modulates the spin of the incident light, allowing the metalens to switch between two imaging modes. The metalens prototype demonstrated clear focal spots for LCP light and doughnut shapes for RCP light, with measured efficiencies reaching 32.3%, 31.7%, and 20.4% at wavelengths of 633, 532, and 450 nm, respectively. Additionally, the LC-integrated metalens rapidly transitioned between bright-field and edge-enhanced imaging modes by efficiently modulating the incident polarization with an applied voltage. The metalens can capture amplitude and phase information at the same time, making it particularly useful for imaging biological samples with weak amplitude fluctuations. The ability to electrically switch between imaging modes enhances the functionality of microscopy setups, providing versatile imaging solutions within a single device.

By combining polarization-dependent metaholograms and independent LCs that modulate the incoming light, electrically controlled holographic displays have been implemented[199–204]. Rho's group explored the integration of LC modulators with metaholograms to develop ultracompact, stimuli-responsive holographic displays capable of real-time operation, as shown in Fig. 4(e)[199]. The metaholograms employ an asymmetric spin-orbit interaction to achieve full-phase modulation and high transmittance for both LCP and RCP light, accomplished by optimizing the dimensions and orientations of rectangular α-Si nanostructures to encode the desired phase shifts. The LC cells could respond to various external stimuli, enabling dynamic control of the polarization state of outgoing light, resulting in switchable holographic images in real time. Particularly, the application of an electric field reoriented the LC molecules, modulated the polarization state of the input light, and eventually achieved real-time switching between different holographic images [Fig. 4(e)], with a response time of approximately 20–30 ms. Besides the electric field, other stimuli, such as heat and surface pressure, could trigger the LC modulator to achieve dynamic holographic images. The capability of dynamically switching holographic images in response to multiple stimuli makes these displays ideal for smart sensing applications. For example, they can be used as holographic labels for temperature-sensitive products or as interactive holographic displays that respond to touch. To address the challenges associated with creating multifunctional metaholograms that can be dynamically tuned, Li *et al.* proposed and experimentally demonstrated an electric-driven, LC-integrated metasurface capable of simultaneous dynamic displays in both near-field and far-field scenarios, as depicted in Fig. 4(f)[202]. The metasurface comprises α-Si nanopillars with varying geometries, systematically arranged to form an architectural database that enables independent phase and amplitude modulation under orthogonal polarizations. This design allows for the realization of near-field and far-field displays simultaneously. The LC cell, confined between treated glass substrates, contains twisted nematic LC molecules whose orientation can be controlled by applying an external electric field, facilitating dynamic modulation of the polarization state of incident light. By varying the applied voltage, the device dynamically switched between two nanoprinting images with high fidelity in the near-field. Simultaneously, different holographic images were successfully reconstructed in the far-field by adjusting the LC driving voltage, demonstrating the device's capability for real-time holographic image switching. While the study presents significant advancements, the information capacity is still limited. To achieve high-capacity metaholograms, other degrees of freedom (DoFs) of light, such as wavelength, should be employed. Recently, Rho's group presented a pioneering approach to dynamic hyperspectral holographs. By integrating inverse-designed metasurfaces with oblique helicoidal cholesteric LC (Ch_{OH}), they demonstrated a highly tunable platform capable of real-time spatial and spectral modulation[204], which holds significant potential for applications in security, display technology, and interactive systems. The metasurface was designed using a computational phase-retrieval process that optimized the placement of meta-atoms to achieve the desired holographic images at multiple wavelengths. The geometric phase with anisotropic meta-atoms was used to ensure broadband operation and high efficiency across the visible spectrum. The Ch_{OH} cell is composed of a mixture of twist-bend nematic LCs and a chiral dopant. This composition allows the LC molecules to form an oblique helicoidal arrangement, which can be dynamically controlled by varying the applied electric field, resulting in the precise tuning of the reflection wavelength. The fabricated LC metasurface successfully displayed 10 independent holographic images with high fidelity and minimal crosstalk at distinct wavelengths, ranging from 420 to 720 nm, as shown in Fig. 4(g). The Ch_{OH} cell demonstrated precise spectral tuning capabilities. By adjusting the electric field, continuous tuning of the reflection wavelength across the visible spectrum was achieved, with the passband below 30 nm, enabling wavelength-multiplexed high-resolution holography without significant overlap between operating wavelengths.

2.3 Electrically Tunable LC Metasurfaces with Directly Pixelated LC Cells

The previously discussed LC metasurfaces employ LCs as an additional index-changing layer on top of functional metasurfaces with direct and indirect interactions. Instead, LCs can be directly patterned as meta-atoms with improved modulation efficiency, increased functional diversity, faster response time, better optical properties, and customizable designs. These benefits make patterned LC meta-atoms an alternative for advanced optical applications and next-generation photonic devices[210–213]. The first example we would like to highlight is a novel SLM that integrates LC-tunable FP nanocavities as individual meta-pixels to achieve high-resolution multispectral operation with continuous 2π phase modulation and high reflectance across RGB wavelengths[212], superior to previously discussed

metasurface-based LC SLMs that are typically limited to monochromatic operation[174]. As shown in Fig. 5(a), the FP-SLM device consists of an array of FP nanocavities, each formed by a thin (sub-micron) layer of LC sandwiched between two partially reflective distributed Bragg reflectors (DBRs). The FP nanocavities are optimized to support multiple resonances across the visible spectrum, enabling continuous 2π phase modulation from 400 to 800 nm. The FP-SLM includes two sets of conducting electrodes, where a thin layer of ITO on the top acts as a common electrode, while the bottom comprises pixelated Al electrodes that individually bias the LC orientation. Applying a bias to individual pixels allows for the local modification of the LC orientation, which creates a varied refractive index landscape and eventually leads to different local phase delays. A proof-of-concept device with 96 individually addressable linear electrodes was fabricated, with each electrode having a width of 1 μm and a separation gap of 140 nm, achieving a pixel pitch of 1.14 μm. To characterize the device, they first verified electrode control and measured reflectance spectra under various biases. Based on interferometric measurements, large phase shifts of $\sim 2\pi$ were demonstrated for RGB wavelengths. They further programmed the FP-SLM device to implement multispectral beam steering by applying voltage profiles to create 0-2π linear phase gradients, which resulted in beam steering with an FOV of $\sim 18°$ and absolute efficiencies exceeding 40%. Specifically, different super-cell configurations (5, 8, and 12 electrodes) were used to achieve tunable beam steering angles, with the highest efficiency observed for the 8-pixel super-cell [Fig. 5(a)]. Additionally, a tunable lens with adjustable focal lengths and numerical apertures (NAs) was demonstrated for a fixed wavelength by reprogramming the device. It is also possible to focus multiple wavelengths at the same focal distance with efficiencies ranging from 16% to 27% for NA = 0.1. The proposed FP-SLM architecture overcomes the limitations of traditional LC-SLMs and metasurface-based devices by enabling high-resolution multispectral operation with small pixel sizes. The integration of LC-tunable FP nanocavities allows for continuous phase modulation with high reflectance at multiple wavelengths, making it suitable for applications in displays, optical computing, and more. To decrease the number of material constituents for high-capacity displays, Lu's group used a single-material LC layer to achieve versatile and electrically switchable vectorial holography[213]. As shown in Fig. 5(b), the LC superstructure, a general LC meta-atom, is designed with a checkerboard distribution of blue and red LC directors, each encoding spin-multiplexed phase holograms for LCP and RCP light based on geometric phases. This configuration allows the LC directors to impart arbitrary polarization and amplitude control at varying spatial positions. The authors designed and fabricated LC superstructures to demonstrate vectorial LC holography with programmable polarization control. A notable example is a vectorial LC-holographic clock displaying distinct time information based on the polarization keys (analyzer). Two sets of phase holograms were nested within a single LC element to display the hour and minute hands independently under RCP and LCP light, respectively. When illuminated by linearly polarized (LP) light, the overlapping areas encoded with vectorial information could be deciphered using specific polarization keys,

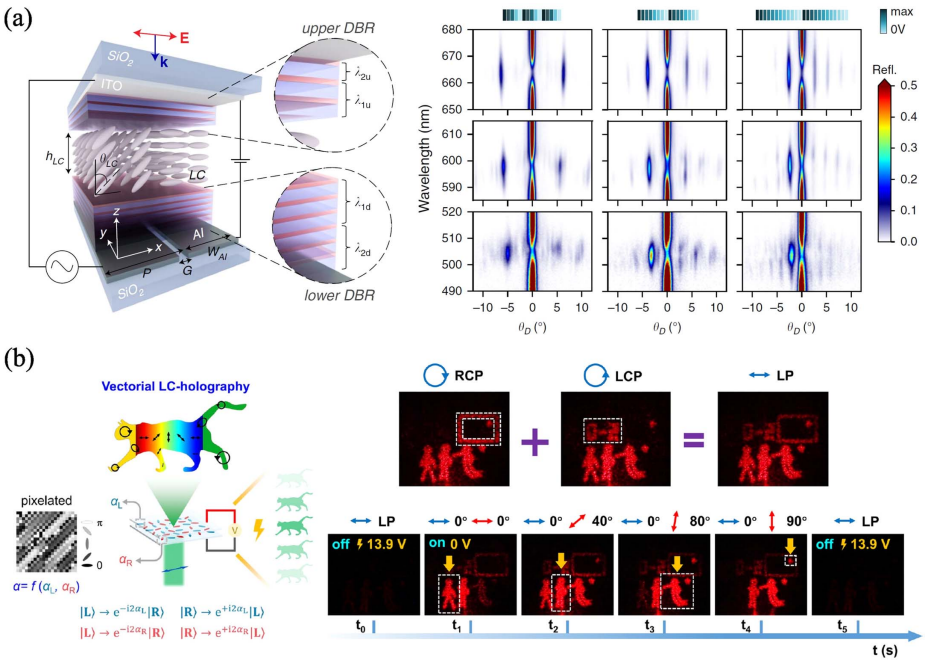

Fig. 5 Electrically tunable LC metasurfaces with directly pixelated LC cells. (a) High-resolution multispectral SLMs with continuous 2π phase modulation based on LC-coupled FP nanocavities. Programmable beam steering was achieved by selectively applying voltage patterns (top panel) to the electrodes to create linear phase profiles. Adapted with permission from Ref. [212] © Springer Nature. (b) Pixelated LC superstructures for generating vectorial holographic images with spatially varied amplitudes and phase differences. The LC-holographic video of a football match was addressed by both the electric field and polarization keys. Adapted with permission from Ref. [213] © Springer Nature.

demonstrating the ability to encode and retrieve complex vectorial data. They further explored the continuous control of both holographic amplitude and vectorial distributions by designing holographic images of the moon phases, encoded with continuously varying LP profiles. The experimental results showed high-quality holographic images with precise control over the vectorial information, confirming the efficacy of the design. Leveraging the dynamic tunability of LCs, the authors demonstrated an active time-sequence vectorial holographic video. They encoded different phases of a football match into the LC superstructure, which could be dynamically displayed by applying an electric field and varying the polarization keys [Fig. 5(b)]. The resulting holographic video showcased high-quality, time-sequenced images, illustrating the potential for real-time vectorial holography applications.

The integration of LCs with optical metasurfaces harnesses the strengths of both components, where metasurfaces offer high spatial resolution and precise light control, and LCs enable dynamic modulation of optical properties. Given that LCs are well-established materials suitable for large-scale production, this synergistic combination can revolutionize photonics by offering unprecedented light control in compact, lightweight, and highly integrated devices. However, several challenges remain in the development of LC-integrated dynamic metasurfaces. The fabrication process is complex and costly due to the precise alignment required between the metasurface and the LC layer, and ensuring material compatibility can be difficult. Additionally, LCs are sensitive to temperature changes, affecting performance and overall stability. The tuning range is limited by the extent of the refractive index change in the LCs, and their response time, currently in the tens of milliseconds, must be further reduced to meet the demands of high-speed photonic systems. Addressing these hurdles will require innovations in both device design and fabrication techniques.

3 Electrically Tunable PCM Metasurfaces

PCMs, whose morphologies and optical properties can be drastically altered through the electrical stimulus, offer a versatile platform for electrically tunable metasurfaces, superior to thermal annealing[214–217] and optical writing[218–225], where bulky heating plates/chambers and ultrafast lasers are necessarily needed.

3.1 Electrically Tunable Vanadium Dioxide Metasurfaces

Vanadium dioxide (VO_2) is one of the appealing volatile PCMs known for its sharp insulator-to-metal transition (IMT) close to room temperature at around 341 K, where it undergoes a reversible change from a monoclinic phase with insulating properties to a tetragonal phase exhibiting metallic behavior[139,141,226]. The IMT in VO_2 involves a change in electronic structure accompanied by a structural phase transition linked to the *d*-orbital electrons of vanadium atoms. This transition is accompanied by significant changes in electrical and optical properties, making VO_2 a material of great interest for numerous applications once integrated with electrical electrodes, including smart windows[227,228], integrated photonics[229–231], and metasurfaces[232–234].

The application of electrically controlled VO_2 metasurfaces for amplitude modulation is a rapidly evolving area of research[235–238]. Particularly, the use of continuous VO_2 films in these metasurfaces demonstrated significant potential for dynamic optical devices due to the uniform phase transition characteristic across the entire surface, ensuring a consistent modulatory effect over large areas[235,238]. In 2016, Werner's group presented a novel plasmonic metasurface design comprising a VO_2 thin film sandwiched between two continuous metallic layers, enabling the dynamic modulation of mid-infrared waves through external electrical stimuli, as illustrated in Fig. 6(a)[235]. In addition to supporting desired resonant modes, the upper mesh-patterned Au antenna layer is connected to two big Au pads that function as electric electrodes to flow the applied current and thus induce Joule heat conduction into the VO_2 thin film, eventually resulting in electrically controlled IMT. This configuration allows for the demonstration of several electrically triggered functionalities, including switchable reflection, a rewritable photonic memory effect, and the tuning of spatially dependent infrared images. Impressively, they successfully showcased substantial modulation in optical reflectance, ranging from nearly 0% to around 80% at a wavelength of 3.05 μm. Later in 2021, Wang *et al.* extended the application of VO_2-film-based technologies into the realm of flexible and electrically tunable metasurfaces[238]. They overcame the traditional limitations of integrating PCMs into flexible metadevices by utilizing mica sheets as substrates, which can withstand high temperatures while retaining flexibility. The Au-VO_2-Au infrared meta-absorber demonstrated remarkable tunability and durability, with the infrared absorption adjusted from 20% to 90% through electrically induced phase transitions of VO_2 with a transferred graphene Joule heater.

Despite relatively large modulation depths, these VO_2-film-empowered metasurfaces are constrained by relatively large energy consumption owing to the large thermal mass of continuous VO_2 films. For instance, an input power of ∼1 μJ per unit cell per pulse is required to activate the IMT[235]. Additionally, the modulation speed is typically at the sub-second level since the applied thermal energy needs time to be dissipated to recover the device. To decrease energy consumption and increase the modulation speed, one feasible approach is to pattern VO_2 into nanostructures with reduced thermal mass[236]. In 2017, Valentine's group introduced an efficient metadevice capable of spectral control in the near-infrared range by minimizing the thermal mass of a VO_2 PCM. In their design, a small VO_2 patch (120 nm × 120 nm × 37 nm) is precisely placed in the feed gap of an Au bowtie antenna to interact with an alumina (Al_2O_3) coated thick Au reflector [Fig. 6(b)], which allows for an experimentally measured spectral tuning range of up to 360 nm and a modulation depth of 33% at the resonant wavelength of 1588 nm with a faster switching speed of 1.27 ms, once the device is electrically switched by injecting the current flow through the intrinsic bus bars connected to large external Au electrodes. The device design facilitates integrated and localized heating, leading to lower power consumption. Specifically, the required current to transition the entire 24 μm × 24 μm sample was determined to be 56 mA with an applied voltage of 2.2 V, leading to a power usage of 123.2 mW and a switching energy per pixel of ∼21 nJ, 47 times smaller than the film-based VO_2 metasurface[235]. Regarding endurance, this current-driven VO_2 metasurface can maintain its good performance in terms of modulation depth and speed after being modulated for over 24,000 cycles, indicating its potential for long-term operation up to millions of cycles without failure. In addition to planar 2D configurations, VO_2 can be patterned as complicated two-and-a-half-dimensional (2.5D) or three-dimensional (3D)

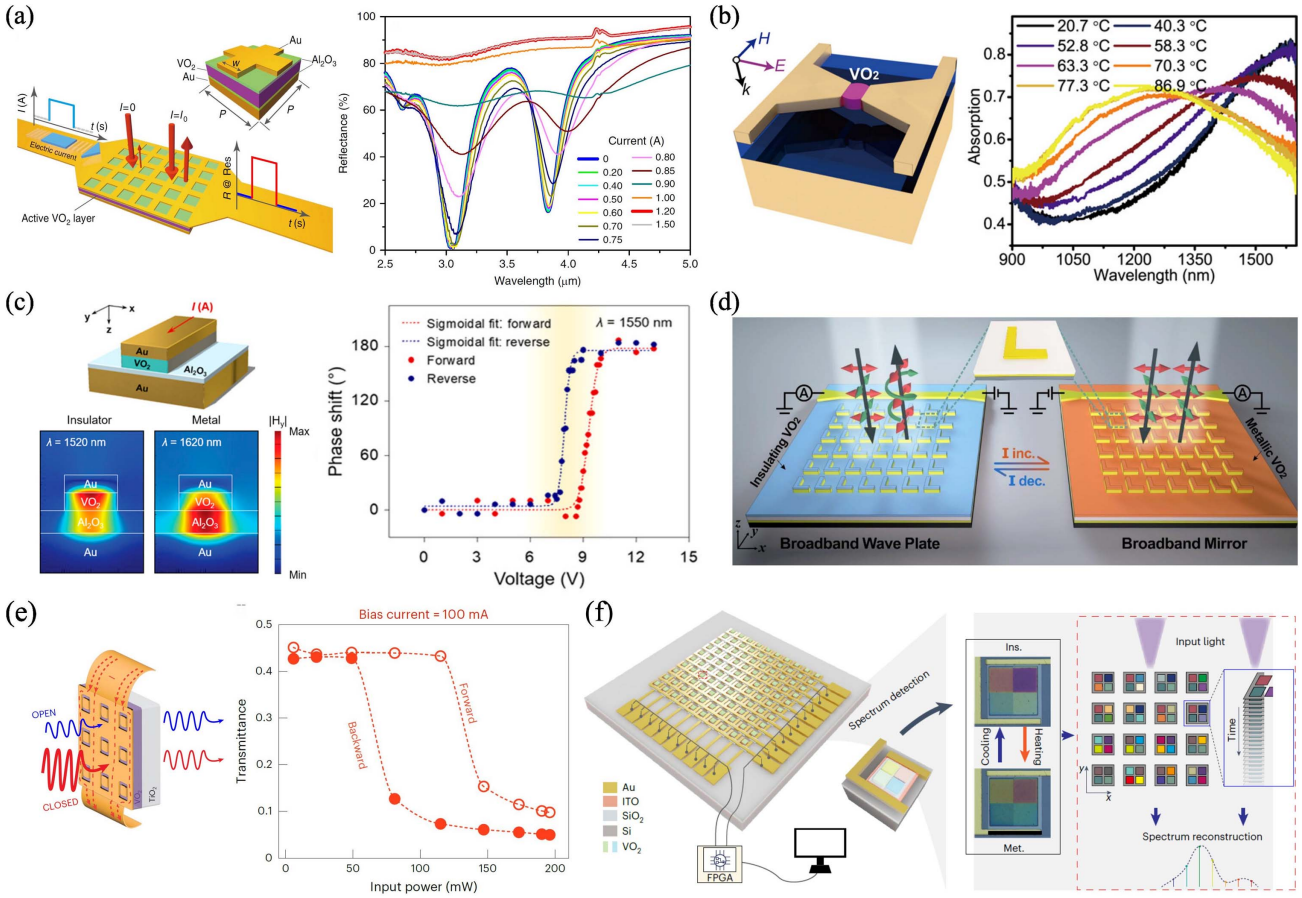

Fig. 6 Electrically tunable VO_2 metasurfaces. (a) A hybrid metasurface absorber consisting of two continuous Au layers sandwiching a thin VO_2 layer for electrically triggered reflection control in the mid-infrared range. A continuous spectral tuning is achieved before saturation when the applied electrical current increases. Adapted with permission from Ref. [235] © Springer Nature. (b) Dynamically reconfigurable metadevice for reflection modulation in the near-infrared range by positioning nanostructured VO_2 patches within the feed gap of Au bow-tie antennas. The absorption spectra vary with the device temperature. Adapted with permission from Ref. [236] © ACS. (c) Electrically tunable VO_2 metasurface for continuous phase modulation of reflected light in the near-infrared range. A reversible voltage-dependent hysteresis loop is shown in the phase shift when the applied voltage varies between 0 and 13 V. Adapted with permission from Ref. [241] © ACS. (d) Electrically driven VO_2 metasurface for broadband dynamic polarization control. When VO_2 transits from the insulating to the metallic phase through the applied current, the metasurface transforms from a broadband HWP or QWP to a mirror. Adapted with permission from Ref. [244] © John Wiley and Sons. (e) Electrically tunable VO_2-Au metasurface for transmission switching and optical isolation in the mid-infrared regime. The OPEN (transmitting) and CLOSED (non-transmitting) states are switched by electrical Joule heating from electrical bias and/or photothermal heating from incident light. Adapted with permission from Ref. [245] © Springer Nature. (f) Electrically programmable nanophotonic matrix consisting of VO_2 cavities on pixelated microheaters. Each unit spectral pixel (2×2 VO_2 cavities) can be individually controlled for spectrum detection. Adapted with permission from Ref. [249] © Springer Nature.

metasurfaces by employing the IMT-induced strain[237,239,240]. For example, Wang *et al.* expanded the utility of VO_2 in MEOMS (microelectro-opto-mechanical systems) to demonstrate a dynamic platform that exhibits over 50% optical modulation depth across a broad mid-infrared wavelength range when the cantilever array, each consisting of VO_2, chromium, and Au nanolayers, is reconfigured by electric currents[237]. The platform's multifunctionality was showcased through applications such as an active absorber and a reprogrammable EO logic gate, indicating its potential in communications, energy harvesting, and optical computing.

Apart from amplitude modulation, we delve into the more sophisticated applications of electrically triggered VO_2 metasurfaces in phase control[241,242]. In a groundbreaking study, Atwater's group introduced a reflectarray metasurface that can continuously modulate the phase of reflected light in the near-infrared range by electrically controlling the phase transition of integrated VO_2 layers from semiconducting to semi-metallic

states, as shown in Fig. 6(c)[241]. The PCM-based metasurface relies on a typical metal-insulator-metal (MIM) gap-surface-plasmon (GSP) unit cell[19], where a 40 nm thick patterned VO_2 stripe is embedded between an Au stripe and an Al_2O_3-coated Au reflector. The top Au stripes simultaneously act as a resistive heater through an electrical connection to an external circuit and support optical resonances. By applying an electric bias, the generated resistive heating induces local and controllable IMT in VO_2 to change the optical resonances. When in its insulating phase, VO_2 excites a magnetic dipole resonance at $\lambda =$ 1520 nm with the magnetic field densely concentrated between the back reflector and the top Au stripe. In the metallic phase of VO_2, the magnetic field predominantly resides within the Al_2O_3 layer, attributable to the diminished effective thickness of the composite dielectric layer comprising both Al_2O_3 and VO_2. Such alterations in the near-field attributes of the mode supported by the metasurface lead to significant modifications in both the amplitude and phase of the light reflected by the structure. At the wavelength of 1550 nm, there is a continuous phase shift from 0° to 180° when the applied bias is gradually increased from 0 to 13 V. Additionally, this phase modulation capability is remarkably broadband, offering significant phase shifts at multiple operation wavelengths. The initially measured response time is ∼15 ms for ON switching and ∼100 ms for OFF switching when high-intensity short pulses are applied. Capitalizing on this design concept, Proffit *et al.* numerically proposed electrically controlled broadband beam steering in the near-infrared range using binary phase control in VO_2-incorporated MIM phase nanoantenna arrays[242]. Through inverse design optimization, the beam steering performance at 1550 nm has been enhanced, achieving continuous beam steering over a 90° range with excellent agreement between theory and simulation results. Furthermore, the design demonstrates robustness against manufacturing imperfections and a broadband response from 1500 to 1700 nm.

In addition to dynamic amplitude and phase manipulation, the IMT in VO_2 also facilitates electrically tunable metasurfaces for active polarization control when combined with anisotropic meta-atoms to offer tunable birefringence. Here we highlight a significant achievement in the modulation of polarization states using a dispersion-free metasurface[243] integrated with PCM VO_2, as shown in Fig. 6(d)[244]. The metasurface employs a MIM structure to achieve optical anisotropy, in which the resonant mode dispersion of "L"-shaped Au antennas is compensated for by the thickness-dependent dispersion of the middle SiO_2 spacer, thereby leading to dispersion-free optical responses that can be tuned by the IMT in the topmost VO_2 layer. When VO_2 transits from an insulating to a metallic state around 341 K, the polarization state of light transitions from horizontal to vertical polarization or from circular to linear polarization across a broad wavelength range, mimicking the functionality of a tunable broadband HWP or quarter-wave plate (QWP). One of the most compelling demonstrations in the study is the proof of concept for dynamically independent control of multiple polarization displays. By applying electrical currents to separate channels within the VO_2 metasurface, the authors successfully manipulate various polarization states, enabling the encoding of 2^N states where N is the number of separated channels, thereby paving the way for advanced applications in display technology, encryption, camouflage, and information processing, among others.

The examples mentioned above demonstrate the advantages of using electrically controlled VO_2 metasurfaces for dynamic light manipulation in the linear regime. Figure 6(e) shows an electrically controlled VO_2-Au-integrated metadevice capable of simultaneously performing three distinct optical functions: switching, limiting, and nonlinear isolation, all tunable through current modulation rather than external heating mechanisms[245]. The metasurface consists of a resonant array of square coaxial apertures in an 80 nm thick Au film on top of a VO_2 film, which achieves a high optical transmission contrast when switched between the resonant and non-resonant configurations with Joule heating through the Au layer providing a bias for controlled heating. As an optical switcher, the device demonstrates an impressive experimental transmission ratio of ∼100 by varying the bias current at the design wavelength of 3.9 μm. When functioning as an optical limiter, the study showcases the ability to adjust the limiting threshold from 20 to 180 mW of incident laser power, indicating significant tunability. Furthermore, they discovered that by electrically heating the VO_2-Au metasurface near the critical IMT point, they could leverage the incoming light beam to supply the requisite additional heat, propelling the material through the edge of the IMT and realizing nonlinear optical isolation. They demonstrated an operational regime in which infrared light transmission was preferentially facilitated in one direction over its reverse, while still ensuring considerable transmission levels. Moreover, the capability to modulate the threshold for nonreciprocity was demonstrated by properly adjusting external heating through the electrical current. Compared to conventional nonlinear isolators, the required optical intensities are much lower since the VO_2 is initially heated close to the critical point of IMT. The measured isolation ratio is ∼5–9, a bit larger than other existing VO_2-empowered mid-infrared nonlinear isolators[246,247]. To further improve the isolation ratio, a high-Q-factor metasurface could be used[248], but at the expense of reduced bandwidths.

Very recently, He's group has made significant advancements in electrically tunable metasurfaces by developing a highly durable, ultrafast, and programmable nanophotonic matrix composed of VO_2 cavities on pixelated microheaters[249]. This matrix, which has been shown to endure over 10^6 switching cycles and operate at speeds exceeding 70 kHz, addresses several persistent challenges in the field, including speed, durability, and programmability. As shown in Fig. 6(f), the nanophotonic matrix features a 12×12 array of VO_2-based cavities integrated with individually addressable pixelated ITO microheaters, allowing precise control over each pixel. The matrix operates through indirect Joule heating, where the microheater modulates the phase of the VO_2 layer by adjusting the thermal dissipation power. The group demonstrated a video-rate color display by electrically addressing VO_2 in a matrix of 12 pixel × 12 pixel. Beyond display applications, the potential for spectrum detection was explored using a spatiotemporal modulation scheme. By integrating 2×2 VO_2 cavities on a single heater as a spectral pixel, the device can modulate light across different spatial and temporal domains. The study showcased accurate spectral detection using the matrix in both snapshot and tuning modes, further highlighting its versatility and potential in advanced nanophotonic applications.

3.2 Electrically Driven Phase Change Chalcogenide Metasurfaces

Phase change chalcogenides (PCCs) represent another class of PCMs that have seen extensive application in the field of

photonics[133,134,136–138,250]. These compounds, typically formed from chalcogen elements such as sulfur (S), selenium (Se), and tellurium (Te) from Group 16 of the periodic table, are combined with elements from Group 13, 14, or 15, including germanium (Ge), antimony (Sb), and arsenic (As)[251]. A distinctive feature of PCCs is their ability to undergo reversible transitions between amorphous and crystalline phases when subjected to thermal, electrical, or optical stimuli. This phase-change mechanism is deeply rooted in their atomic structure and bonding[252,253], where the rapid shift between states is driven by the movement of atoms into positions that either enhance long-range order (crystalline) or disrupt it (amorphous). Such structural transformations lead to significant and non-volatile alterations in their optical properties, which require zero static energy to hold the programmed states, superior to the volatile IMT in VO_2. These changes are harnessed in metasurfaces to dynamically modulate light interaction with engineered meta-atoms[134,214–216,218,219,221,222], leveraging PCCs' remarkable characteristics including a high refractive index contrast ($\Delta n \geq 1$), non-volatility with long retention time exceeding 10 years, ultrafast switching speeds in the range of 10 ns to 100 ns, robust switching endurance of over 10^9 cycles, low-energy transitions down to a few aJ of energy per cubic nanometer, and compatibility with CMOS manufacturing processes. The subsequent section will delve into the applications of dynamically triggered PCC metasurfaces through electrical stimuli.

GeSbTe (GST) or GeSbSeTe (GSST) alloys are a subset of PCCs with intriguing properties, which have been widely used in data storage technologies, such as rewritable CDs and DVDs, and more recently, in non-volatile phase-change random access memory[254–256]. They are also increasingly being explored for use in reconfigurable metasurface applications, where their phase transition capabilities enable dynamic control of light. Early in 2014, Bhaskaran and colleagues reported the first GST-integrated optoelectronic metasurface framework emerging as a new benchmark for high-resolution color pixels in display technology[257]. In line with lossy thin films for color rendering[258], this approach used lossy GST thin films or nanostructures, which are sandwiched between two conductive ITO layers on a reflective conductive base, as illustrated in Fig. 7(a). The transition of the GST layer from an amorphous to a crystalline state triggers a pronounced color transformation across the nanometer-thick film, showcasing its potential for crafting distinct pixels in display devices. Utilizing lithographic techniques, an array of these uniquely colored pixels was engineered, each capable of undergoing individual color shifts by positioning a nanoscale conductive tip. This advancement reduces pixel dimensions to hundreds of nanometers (e.g., 300 nm), facilitating the development of ultra-high-resolution displays. Following this general concept, the team introduced $Ag_3In_4Sb_{76}Te_{17}$ (AIST), another PCC alloy, which surpasses GST in terms of modulation capability for pixeled displays[259]. Additionally, continuous grayscale imaging was realized by manipulating the degree of crystallization with applied voltage. Although these two examples demonstrate the potential of using conductive nanoscale tips to electrically switch the PCC-integrated color pixels for high-resolution, flexible display technologies, this methodology carries specific limitations inherent to its execution and practical application. First, the precision required for a conductive tip to accurately switch individual pixels is high, especially as the pixel size decreases to improve resolution. While effective on a small scale, this approach may face challenges scaling up to larger displays with millions of pixels, where uniformity and precision across the entire display are critical. Second, the switching speed may be slower compared to other non-contact methods, which could potentially limit the refresh rate of the display, impacting applications that require fast updating of the visual content. Last, integrating a mechanism that relies on conductive tips for switching in a mass-produced display introduces complexity in manufacturing. Similarly, maintenance or repair of such displays could be more challenging, as the precise alignment and functionality of the conductive tips are crucial.

To realize a unique electrically controlled PCC metasurface platform, integrated electrodes offer an appealing solution with energy efficiency, rapid response, precise control, scalability, and compatibility with existing fabrication techniques. In 2021, two independent works have shown the possibility of using integrated resistive microheaters to switch PCC metasurfaces, which offer strong, reversible, non-volatile, and multi-state switching in the visible and near-infrared regimes with low energy consumption and full integrability with existing optoelectronic circuits[260,261]. In a groundbreaking study[260], Brongersma's group navigated this challenge of implementing electrically programmable antennas and metasurfaces by employing GST as the cornerstone material. They first demonstrated an electrically tunable antenna composed of a GST nanobeam stacked atop an Ag stripe with a length of 10 μm by properly fine-tuning both the thermal and optical parameters. Through pulsed currents heating the Ag nanostrip electrode, the GST antenna is switched between the amorphous and crystalline states, resulting in a scattering efficiency modulation of around 30%. Moreover, they have developed a reflective GST metasurface with an area of 5 μm × 5 μm on top of an Ag contact layer, whose operation hinges on the application of electrical pulses of varying intensity and duration, as shown in Fig. 7(b). Specifically, a prolonged (∼20 μs) but relatively weak electrical pulse is employed to transition the GST-Ag metasurface into a state of near-perfect absorption. Conversely, a short (∼500 ns) but intense pulse reverses this effect, rendering the GST-Ag metasurface highly reflective. The reflectance variation achieved in the experiment is notably substantial, reaching a maximum ratio of 4.5 at the wavelength of 755 nm. Figure 7(b) also illustrates the dynamic modulation of the reflected signal, which fluctuates in response to the application of reset and set pulses. This modulation demonstrates notable stability and consistency across multiple cycles, underscoring the device's reliable performance and the efficacy of the electrical tuning mechanism. Meanwhile, Hu's group reported a large-scale (up to 400 μm × 400 μm), electrically reconfigurable metasurface using GSST, a non-volatile PCC that possesses a wider transparent window across different structural states and a larger switching volume compared to GST compounds[261]. Through a smart design that combines geometrically optimized heaters with GSST meta-atoms, they have achieved precise and uniform phase transitions across the whole metasurface area with activated electrical pulses (e.g., a single ∼10 V, 500 ms pulse for crystallization and a single 20 V, 5 μs pulse for amorphization), as shown in Fig. 7(c). With a GSST metasurface composed of a periodic array of identical meta-atoms, they demonstrated binary switching with a large absolute reflectance contrast of 40% at $\lambda = 1.49$ μm and a relative reflectance modulation up to 400% at $\lambda = 1.43$ μm. In addition, quasi-continuous multi-state tuning with a record half-octave spectral

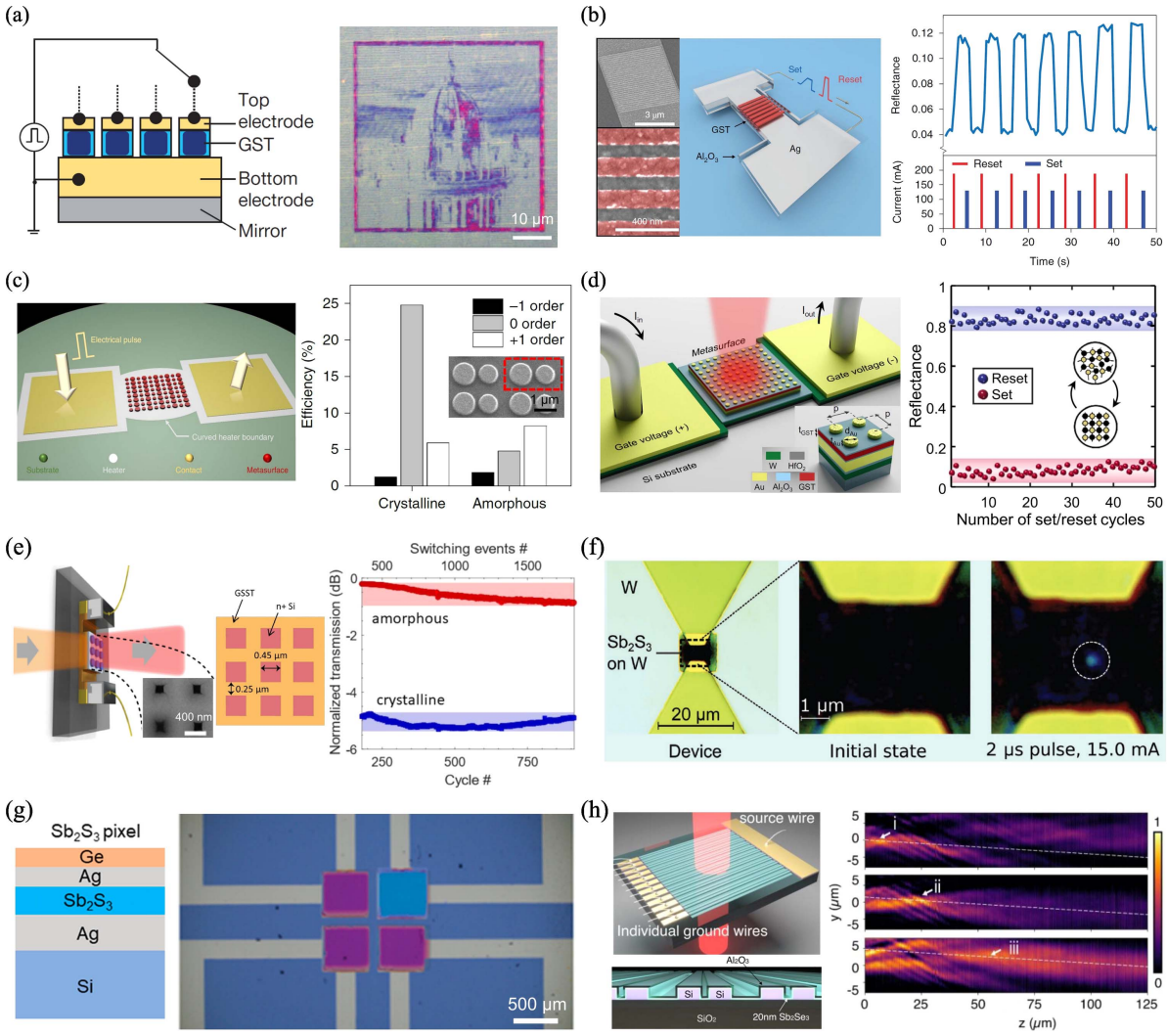

Fig. 7 Electrically tunable PCC metasurfaces. (a) GST metasurface emerging as an integrated optoelectronic framework for high-resolution electronic display, in which a nanoscale conductive tip is used to locally switch color pixels by applying a voltage between the two ITO layers. Adapted with permission from Ref. [257] © Springer Nature. (b) Electrically actuated GST-Ag metasurface for reflection modulation in the visible range. The absorption spectra vary with the device temperature. Reset and set pulses are applied through the Ag strip, heating the metasurface to facilitate a reversible transition between the amorphous and crystalline phases. Adapted with permission from Ref. [260] © Springer Nature. (c) Electrically reconfigurable metasurface beam deflector based on GSST meta-atoms on a metal heater. The deflection efficiencies are redistributed at the design wavelength of 1550 nm by switching the phase of GSST meta-atoms. Adapted with permission from Ref. [261] © Springer Nature. (d) Electrically reconfigurable heterostructure meta-device for non-volatile, reversible, multilevel, fast, and remarkable optical modulation in the near-infrared spectrum by integrating a robust resistive microheater with an Au-Al_2O_3-GST-Al_2O_3-Au metasurface. An absolute reflectance contrast reaching 80% can be achieved between the reflective and absorptive states during multiple electrical sets and reset pulses. Adapted with permission from Ref. [262] © Springer Nature. (e) GSST fishnet metasurface for electrically tunable transmission modulation. Low- and high-transmission states with a contrast ratio of 5.5 dB can be consistently switched using electrical pulses for 1250 cycles. Adapted with permission from Ref. [264] © John Wiley and Sons. (f) Electrically switchable W-Sb_2S_3 color filter. Adapted with permission from Ref. [266] © John Wiley and Sons. (g) Electrically tunable Sb_2S_3 SNOC pixels. Individual Sb_2S_3 SNOC pixels are controlled with a DC voltage of 10 V. Adapted with permission from Ref. [270] © ACS. (h) Electrically programmable Sb_2Se_3 metasurface as a phase-only transmissive SLM by independently controlling individual meta-molecules. Tunable focusing with different focal lengths is observed by selectively transitioning the phase of 2 (i), 4 (ii), and 6 (iii) central meta-molecules to the amorphous state while maintaining the rest in the crystalline state. Adapted with permission from Ref. [271] © ACS.

range from 1.19 to 1.68 μm was realized by controlling the voltages of crystallization pulses. The researchers also prototyped a polarization-insensitive phase-gradient metasurface consisting of two GSST meta-atoms to showcase the potential for dynamic optical beam steering at the wavelength of 1.55 μm [Fig. 7(c)]. This capability is particularly noteworthy as it leverages the non-volatile characteristics of PCC metasurfaces, enabling reconfigurable optics that can be dynamically altered without a constant power supply.

Despite significant achievements, these two examples have rather limited absolute reflectance contrasts (<40%) due to the interference from lossy metallic wiring with the incident light on the subwavelength scale of the PCC meta-atoms. In addition, the issue of crystallization filamentation leads to a direct current path through the PCC, hindering a uniform phase transition across the entire volume of the meta-atoms. To overcome these hurdles, Adibi's group has demonstrated an electrically reconfigurable heterostructure metadevice platform for non-volatile, reversible, multilevel, fast, and remarkable optical modulation in the near-infrared spectrum by combining a robust tungsten (W) microheater with an Au-Al_2O_3-GST-Al_2O_3-Au metasurface, enabling uniform electrothermal phase conversion of the continuous GST layer without compromising the optical efficiency, as shown in Fig. 7(d)[262]. This approach achieves an absolute reflectance contrast of up to 80% at a potential operation speed of a few kHz, surpassing previous implementations of PCC-based reflector-absorber switches[260,261]. Meanwhile, it mitigates the thermal deformation of meta-atoms, a common issue with alternative resistive heating strategies that employ plasmonic materials prone to low melting points. More importantly, this electrically driven model facilitates the achievement of multiple non-volatile intermediate states of GST, enabling the creation of multi-state reconfigurable metasurfaces crucial for the advancement of adaptive optics technologies. They also successfully showcased the capability of active beam steering within the near-infrared spectrum through the utilization of an electrically actuated phase-change gradient metasurface. By altering the GST's phase from amorphous to crystalline, precise control over the deflected power between the +1st and zeroth diffraction orders was implemented. However, such a GST meta-deflector could only dynamically tune the power distribution between the +1st and zeroth diffraction orders and lacks the capability of continuously steering the diffracted beams in a controlled way, which requires addressing individual metasurface pixels instead of the whole meta-device. To solve this issue, Adibi's group has numerically proposed a hybrid Au-GST-Au metasurface to tune the reflection phase over a wide range of 315° while maintaining moderate reflection amplitudes (>15%) by electrically controlling the crystalline fraction of GST through Joule heating[263]. By individually triggering each meta-atom with a proper voltage, phase, amplitude, or polarization of reflected light could be dynamically reconfigured.

To move the operation regime of active PCC metasurfaces from reflection to transmission, which is more appealing for practical applications, transparent electrodes can potentially replace conventional opaque metal heaters. For instance, a transparent silicon-on-insulator (SOI) microheater was used to successfully achieve a reversible switching near-infrared optical filter based on a 200 μm × 200 μm fishnet GSST meta-atom array, as displayed in Fig. 7(e)[264]. As a proof of concept, a transmissive metasurface filter (meta-filter) shows consistent switching between low- and high-transmission states through electrical pulses, achieving a switching contrast ratio of 5.5 dB. Remarkably, the meta-filter sustains reversibility for 1250 cycles before experiencing accelerated degradation, marking a great advancement toward the realization of free-space reconfigurable optics. Therefore, the study heralds a new era for electrically controlled PCC metasurface devices suitable for transmissive optics using doped crystalline Si as the optically transparent heater, which is compatible with CMOS processes and exhibits low loss in the infrared spectrum.

The inherent narrow bandgap of Ge-composite PCCs limits the efficiency of aforementioned dynamic metasurfaces, particularly in the visible spectrum where PCCs strongly absorb light in both amorphous and crystalline states. Consequently, there is a growing demand to discover new PCCs with wider bandgaps. By removing Ge and substituting Te with Se or S, the bandgap broadens, leading to the formation of Sb_2S_3 and Sb_2Se_3, which are transparent in near-infrared wavelengths[265–268]. In particular, Sb_2S_3 has bandgaps of $2.05\,\text{eV} \pm 0.05\,\text{eV}$ and $1.72\,\text{eV} \pm 0.05\,\text{eV}$ in amorphous and crystalline states, moving the absorptance band-edges to the wavelengths of 605 and 721 nm, respectively, which can be considered as a potential low-loss platform for dynamic metasurfaces operating at visible wavelengths[223–225,266]. Besides larger bandgaps, Sb_2S_3 exhibits a substantial and nonvolatile refractive index change upon crystallization, with the maximum Δn approaching ~1 at $\lambda = 614$ nm. By coupling Sb_2S_3 to an optical cavity composed of multiple thin films, Simpson's group demonstrated tunable structural colors by actively switching the Sb_2S_3 absorption edge with both optical and electrical stimuli[266]. For instance, they showed that a metal/Sb_2S_3 color filter can be electrically switched by depositing Sb_2S_3 on top of a W filament, which allows them to directly probe the optical response of the active Sb_2S_3 area before and after the application of electrical pulses. Figure 7(f) presents images of the device in its initial state and after a 2 μs, $15.0\,\text{mA} \pm 1\,\text{mA}$ pulse. When Sb_2S_3 is in its amorphous state (initial state), the W/Sb_2S_3 metasurface possesses high absorption in the visible spectrum, rendering the image of the active area dark. Once Sb_2S_3 is electrically triggered to the crystalline state, the appearance of W/Sb_2S_3 becomes light blue-gray. However, this color filter is sensitive to a small increase in the electric current, leading to ablation of the hottest area after applying a 2 μs, $15.7\,\text{mA} \pm 1\,\text{mA}$ pulse. Therefore, robust electrical switching with excellent endurance needs further investigation. To enhance the color tuning range of thin-film optical coatings, two distinct PCCs were utilized[269,270]. In 2021, Singh's group demonstrated electrically dynamic color generation by employing a broadband GST-Ag absorber and a narrowband Sb_2S_3-Ag absorber to form an active thin-film coating that achieves tunable optical Fano resonance within the visible spectrum[269]. By applying electrical pulses to an integrated W microheater, the structural phase of the PCCs within the film can be switched between amorphous and crystalline states, altering the reflection spectrum and thus the color. Continuous tuning of the Fano resonance was achieved by increasing the DC current from 0 to 300 mA, enabling significant color tunability from pink to greenish yellow with a 15 nm thin Sb_2S_3 layer. Later in 2023, the same group used this concept to develop PCCs-integrated steganographic nano-optical coatings (SNOCs) as electrically tunable color reflectors for secure optical data storage, as illustrated in Fig. 7(g)[270]. The SNOC was designed to create optical Fano resonances with tunable linewidths but fixed resonance wavelengths by structurally

adjusting the PCC layer from amorphous to crystalline within the visible spectrum, enabling high-purity color generation. Optical steganography was implemented using tunable SNOC color pixels by dividing the SNOC cavity layer into two regions, each made from different dielectric materials (Sb_2S_3 or TiO_2) yet maintaining identical optical thicknesses. Furthermore, they showcased the electrically tunable color capability of individual Sb_2S_3 SNOC pixels within a 2 pixel × 2 pixel array, fabricated on microheater devices to enable precise control and modulation of colors. By applying a DC voltage of 10 V, the initial violet color was changed to blue. Nevertheless, such thin-film color coatings suffer from larger pixel sizes and slower modulation speeds. Additionally, reversible color switching has not been realized in such PCC thin-film coating, which, in turn, requires judiciously designed microheaters to enable transient melting and rapid cooling simultaneously.

To enable substantial free-space light control with smaller pixel sizes and faster speeds, one needs to utilize PCC meta-atoms with proper resonances to enable substantial phase or amplitude modulation. Fang and colleagues presented a significant advancement in electrically controlled phase modulation by introducing a state-of-the-art transmissive SLM that effectively utilizes the unique properties of Sb_2Se_3 (i.e., non-volatile behavior and low loss in the near-infrared regime), as depicted in Fig. 7(h)[271]. Integrated into a high-Q (∼409) diatomic Si metasurface, Sb_2Se_3 facilitates a phase-only modulation of $\sim 0.2\pi$ in the experiment. The robustness of the device is evidenced by its ability to endure over 1,000 switching cycles with no noticeable performance degradation by applying SET and RESET electric pulses to the doped Si microheater. The authors further leveraged an alternative GMR to enhance the interaction between TE-polarized light and the Sb_2Se_3 layer, where a resonance shift of approximately 8 nm, alongside a 2π phase shift, was achieved through precise control of individual meta-molecules [Fig. 7(h)]. For the designed SLM, individual meta-molecule control was realized through the electrical connection between a single source channel and 17 separate group channels, each linked to one of 17 meta-molecules. By applying varied phase profiles, tunable far-field beam shaping with three focal lengths was successfully demonstrated. The simplicity, reliability, and capability of this Sb_2Se_3 SLM offer a promising alternative to more traditional technologies like LCs or MEMS if full 2π phase-only control with unity transmission is achieved with more complicated meta-atom designs, potentially reducing the complexity and cost of manufacturing and maintenance.

Despite their potential, electrically controlled metasurfaces using PCMs present several limitations. The phase transition temperature of VO_2, around 68°C, can be unsuitable for many applications, requiring additional energy to trigger the phase change or causing unintended transitions in common environmental conditions. PCCs often have even higher transition temperatures, further limiting their practical use. Therefore, thermal management is crucial, as localized heating to induce phase changes can lead to heat dissipation issues, affecting performance and longevity. Material stability is another concern, as repeated phase transitions can lead to fatigue and affect long-term reliability. Particularly, producing high-quality, pure VO_2 with consistent properties remains challenging, as does the synthesis and integration of VO_2 nanoparticles into nanophotonic devices, which is both complex and costly. The tunability of PCMs is inherently limited, restricting their application in scenarios requiring a broad range of optical responses[137]. Additionally, integrating PCMs with other materials can be problematic due to differences in thermal expansion, chemical reactivity, and mechanical properties, potentially leading to interface degradation or delamination. Environmental and health concerns also arise from the toxicity of constituent compounds, necessitating safe handling protocols and proper disposal methods. By overcoming these hurdles, the potential of PCMs in active metasurfaces and other photonic applications continues to grow.

4 Electrochemically Activated Metasurfaces

Electrochemical reactions, fundamental to processes such as energy storage in batteries, corrosion protection, and sensing, are significantly influenced by the surface characteristics of the materials involved. Metasurfaces, by their engineered features, offer an effective way to modify surface areas, electron transfer rates, and local electromagnetic environments, thereby profoundly altering the dynamics of electrochemical reactions. Meanwhile, the integration of electrochemical environments into metasurfaces has led to the development of a novel class of active metasurfaces, which can be dynamically tuned and reconfigured through electrochemical stimuli, allowing for the versatile manipulation of light at the nanoscale in a controllable manner, a feature particularly beneficial in applications like smart windows that change transparency or color in response to electrical inputs[272–274].

4.1 Electrochemically Activated Metasurfaces Based on Inorganic TMOs

To develop efficient electrochemically activated metasurfaces with good performance, it is critical to choose materials for the electrodes. Inorganic TMOs, such as tungsten trioxide (WO_3) and TiO_2, are excellent electrochemical materials that can dynamically modify their optical properties *via* reduction and oxidation (redox) chemical reactions in many cycles. During a redox cycle, both electrons and guest ions (i.e., Li^+) are concurrently introduced into a redox-active host material. This simultaneous injection significantly alters the distribution of charge carriers, thereby largely modulating the complex refractive index and resulting in dynamically controlled optical responses. For instance, TMO thin films change their color or opacity under the influence of an electrical stimulus, a phenomenon called "electrochromism"[272,275]. Integrating electrochromic TMOs with metasurfaces enables the development of dynamical structural coloration with superior properties in terms of wider color ranges, high resolutions, good thermal stability, long endurance, and compatibility with standard nanofabrication processes[65,123,163,276,277].

Brongersma's group demonstrated dynamic modulation of gap plasmon resonances using a thin TMO Li_xWO_3 spacer layer sandwiched between an Al base layer and Al nanorods, forming a typical MIM cavity, as depicted in Fig. 8(a)[276]. These $Al/Li_xWO_3/Al$ resonators exhibited changes in their plasmonic colors in response to variations in the optical properties of Li_xWO_3, which were controlled by adjusting the Li concentration x with an electrical stimulus. Upon applying a certain voltage, Li ions were injected into the Li_xWO_3 layer from nearby ionically connected $Li_{0.7}FePO_4$ electrodes, shifting the refractive index from ∼2.1 in its lithiated state (−1.4 V) to ∼1.9 in its delithiated state (1 V). This change in refractive index modified the resonance conditions and led to a resonance shift of

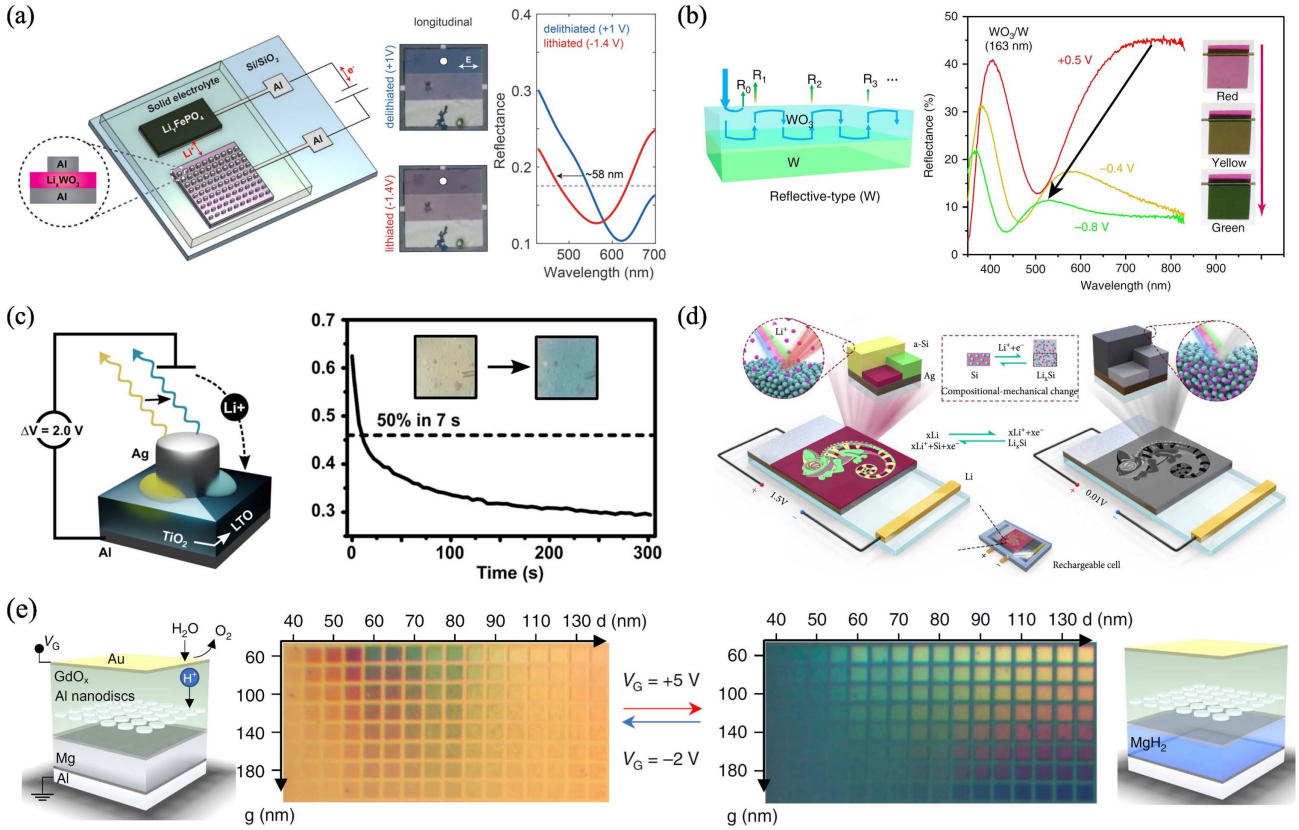

Fig. 8 Electrochemically activated metasurfaces based on inorganic materials. (a) Electrically controlled Al/Li_xWO_3/Al gap plasmon resonators for tunable structural color generation, where Li^+ ions are reversibly inserted and removed under specific voltages. The color changes from blue to red/purple upon lithiation, corresponding to a blue shift of 58 nm in the reflection spectrum. Adapted with permission from Ref. [276] © ACS. (b) Asymmetric W-WO_3-PET FP nanocavity for tunable structural colors. By electrically adjusting the amount of Li injected into the WO_3 layer, subtle color modulation from red to green was achieved. Adapted with permission from Ref. [278] © Springer Nature. (c) Electrochemically actuated Ag-TiO_2-Al plasmonic metasurfaces for dynamic color tuning. The metasurface exhibited a significant color change from gold to green when anatase TiO_2 transitions to LTO. Adapted with permission from Ref. [279] © ACS. (d) Compositionally and mechanically dual-altered rechargeable Si metasurfaces integrated into an LIB cell for dynamic color display. Under a low voltage, lithiation and delithiation processes occur dynamically to control the phase transformation from Si to Li_xSi, enabling high-contrast colorization and decolorization with long cyclic stability. Adapted with permission from Ref. [280] © AAAS. (e) Switchable plasmonic color generation by integrating an electrically controlled local proton source. When a positive bias of 5 V is applied, hydrogen ions split from moisture travel through a proton-conducting GdO_x layer and transform Mg to MgH_2, resulting in color changes. Adapted with permission from Ref. [288] © Springer Nature.

58 nm from approximately 620 nm (purple color) to 565 nm (blue color) in the reflectance spectra. Owing to the use of MIM plasmonic structures, vivid structural colors were produced. In addition, intense light–matter interactions at the plasmonic hotspots allow a substantial decrease in the Li_xWO_3 thickness down to 17 nm. Furthermore, the switching time, a critical parameter for display technologies, was improved to 20 s. The researchers also demonstrated continuous color adjustment through cyclic voltammetry sweeping and robust bistability over several minutes. Nevertheless, the approach is hindered by relatively slow switching speeds and the necessity for a high operating temperature of 80°C to enhance ionic conductivity. While optimizing the doping process, such as substituting Li^+ ions with protons, might enhance ion diffusivity and shorten switching time, the current configuration appears somewhat unsuitable for display applications in its present form. In this Al/Li_xWO_3/Al gap plasmon resonator, the absorption bandwidth is quite wide, hindering the precise tuning of plasmonic colors. FP cavities with narrow resonances provide a viable solution to this problem. Recently, asymmetric FP cavities have been utilized to achieve rich and precise structural color tuning in reflection mode, as shown in Fig. 8(b)[278]. These nanocavities were fabricated by sequentially sputtering uniform layers of W and amorphous WO_3 onto polyethylene terephthalate (PET) substrates. This method is relatively simple as it requires no nanopatterning and is fully compatible with standard

electrochromic fabrication techniques. The W layer acts as a partial reflector and a current collector at the same time, enabling a good match of reflections at the WO_3 interfaces. As a result, the incident light bounced back and forth within the WO_3 thin layer, enhancing or suppressing the reflected light at specific wavelengths depending on the thickness and refractive index of the WO_3 layer. In the experiment, reflectance modulations of up to 50% and various distinct structural colors have been implemented, which remain nearly unchanged at oblique angles of incidence up to 40°. Moreover, by inserting Li ions from an external reservoir into the WO_3 layer, its refractive index was continuously varied from 2.15 to 1.61 at a wavelength of 600 nm, resulting in rich and subtle color modulation since the colors are directly related to the WO_3 refractive index. For example, a wide range of color modulation, from red (0.5 V) to yellow (−0.4 V) and green (−0.8 V), was realized for a 163 nm thick WO_3 film, corresponding to a very large modulation range of the FP resonance (243 nm), which shifted the reflection peak position from 760 to 517 nm. In addition, this color modulation was reversible and showed good cycling stability over 1000 cycles. The measured switching time between a steady bleached and colored state was on the order of a few seconds, comparable to other inorganic electrochromic materials.

TMO TiO_2 is ideally suitable for reversible color generation when electrochemically lithiated to $Li_{0.5}TiO_2$ (LTO), which offers an index change of 0.65 at 649 nm with minimal absorption[279]. Capitalizing on the phase transformation from TiO_2 to LTO, Eaves-Rathert *et al.* employed a simple FP nanocavity to harness the dynamic tunability of TiO_2, where a 100 nm TiO_x film was deposited on a titanium backplane and annealed to form anatase TiO_2. This nanocavity demonstrated a broadband reflection with a local minimum of around 410 nm due to the destructive interference. Upon lithiation to LTO under a bias of less than 2 V, the reflection peak shifted to blue-green wavelengths (∼490 nm), achieving a 114 nm blue shift. To improve switching speed and color tunability, they integrated the TiO_2/LTO system into a gap plasmon metasurface configuration, which involved 20 nm thick TiO_2 films placed between patterned Ag nanopillars and an Al backplane, as shown in Fig. 8(c). This configuration enhances light–matter interaction within the gap, leading to strong absorption due to the GSP resonances. As such, the metasurface exhibited a significant blue shift in reflectance minimum (135 nm) when transitioning from anatase TiO_2 to LTO, resulting in a color change from gold to green. The switching speed was found to be competitive with other materials like Li_xWO_3, with 50% of the reflectance change achieved within 7 s, which is mainly limited by the device platform since the Li^+ ion transport is very efficient with measured diffusion coefficients on the order of 10^{-11} cm^2/s. Further electrochemical characterization showed excellent cycling stability, where a 20 nm anatase film cycled at 3 $\mu A/cm^2$ demonstrated stable lithium capacity retention over 400 cycles. Capitalizing on the similar reversible lithiation and delithiation process in a lithium-ion battery (LIB) setup, Yang *et al.* utilized Si, the predominant semiconductor material for electronics and photonics, to implement compositional and mechanical dual-altered rechargeable metasurfaces for broadband optical reconfiguration in the visible and near-infrared regions through an electro-chemo-mechanical coupled process, as shown in Fig. 8(d)[280]. They fabricated metasurfaces by patterning Si structures onto an Ag film coated on a quartz substrate. These Si structures were integrated into a LIB cell, where the Ag layer served as a current collector during charging and discharging cycles. The dynamic color changes were driven by the compositional transformation from Si to lithium silicon (Li_xSi) and the mechanical expansion of the Si layer during lithiation and delithiation processes, under a low voltage of ≤1.5 V. The volume of the Si layer could expand up to 300%, dramatically altering both structural morphology and optical scattering properties, resulting in high-contrast colorization and decolorization within 30 s and significant cyclic stability (>400 cycles). With a straightforward multilayer film deposition method, they created chameleon and butterfly patterns with four distinct colors depending on the varied thicknesses of the Si layers. Upon electrochemical activation, the colors could be dynamically and reversibly tuned by controlling the external voltage within 1.5 V. The initial vibrant colors transformed into a uniform dark green upon full lithiation and returned to their original state after delithiation. Additionally, intermediate colors were achieved during the transition by properly controlling the electrochemical potential of the Li_xSi linked to the applied voltage, which could be stabilized and maintained even after disconnecting the electrical supply. High-resolution structural colors with significant color and intensity modulations were further demonstrated using electron beam lithography (EBL) to create L-shaped and bowtie nanostructures with different periods and gaps. Apart from the periodicity of the nanostructures, the incident and observation angles could be used to vary structural colors, which allows for color encoding with both viewing angle and applied voltage, presenting a novel strategy for multidimensional information encryption. Very recently, Kovalik *et al.* leveraged this concept to achieve reversible color tuning in the visible spectrum using Li-ion insertion in α-Si metasurfaces that support multiple Mie resonances[21,173] and possess significant changes in both the refractive index ($\Delta n = 0.12$ at 500 nm) and lattice expansion[281]. With a power consumption of less than 120 $\mu W/cm^2$, pronounced color bleaching was observed. Notably, the device maintains good optical performance after multiple lithiation cycles, showing resilience against mechanical degradation. In addition, continuous color tuning is achieved, with intermediate alloyed states accessible for varying degrees of color bleaching.

Like lithiation of TMOs, hydrogenation of phase transition metals like magnesium (Mg) provides a unique material platform for dynamic metasurfaces[282–287]. Driven by the absorption and desorption of hydrogen, metal hydrides undergo substantial changes in their crystallographic and electronic structures, leading to significant alterations in their optical properties and facilitating an IMT. Despite significant achievements in Mg-integrated dynamic metasurfaces, cumbersome gas chambers for (de)hydrogenation are required, which is a major drawback for practical applications. Huang *et al.* provided an efficient solution to address this limitation by integrating a nanoscale solid-state proton source into Mg-based plasmonic devices, which enables the precise and selective modification of the optical properties of Mg[288]. As shown in Fig. 8(e), the electrically switchable plasmonic device comprises an Al/Mg/Pd stack, periodically arranged Al nanodiscs embedded in a thin gadolinium oxide (GdO_x) layer, and a thin Au layer, where Mg acted as a switchable mirror. By controlling the diameter and spacing of the nanodiscs as well as the distance between the reflective Mg mirror and the Al nanodisc arrays, a variety of reflective plasmonic colors were generated. When a positive bias of 5 V was applied to the top Au electrode for 120 s, water molecules from

moisture near the GdO_x/Au interface were split into molecular oxygen (O_2) and hydrogen ions (H^+). The gate bias then drove these protons through the proton-conducting GdO_x layer to the bottom Al/Mg electrode (mirror), leading to the hydrogenation of the Mg layer, which could be accurately controlled by specific patterned gold electrodes that served as sources for hydrogen ions. As a result, the metallic Mg transformed into the optically transparent dielectric MgH_x, leaving the Al layer as the bottom mirror. Consequently, the effective thickness of the new spacer, consisting of both GdO_x and MgH_x, is increased, resulting in a blue shift of the plasmonic resonance and a change in the plasmonic colors accordingly. When a negative bias of −2 V was applied for 1 h, the plasmonic colors returned to their original states, showcasing excellent reversibility even after hundreds of cycles. While water hydrolysis and proton transport were relatively fast (∼10 ms), the hydrogenation and dehydrogenation processes require sufficient time to load and unload hydrogen, dramatically slowing the overall switching speed. To realize fast switching, one may only utilize refractive index changes in GdO_x to switch colors produced by thin-film interferences.

4.2 Electrochemically Activated Metasurfaces Based on Conducting Polymers

Apart from inorganic materials, conducting polymers, a specific branch of organic materials, have emerged as highly promising materials for developing electrochemically activated metasurfaces with faster switching speeds and more advanced functionalities. Conducting polymers are organic polymers capable of conducting electricity, a property typically associated with metals and inorganic semiconductors[144]. Their conductivity arises from a typical conjugated backbone with alternating single (σ) and double (π) carbon-carbon bonds, facilitating the movement of charge carriers, such as electrons and holes. These charge carriers can be incorporated directly during polymerization or *via* post-processing methods, such as chemical or electrochemical doping. Unlike the doping of inorganic semiconductors, where doping levels are much lower (typically less than 1%), conducting polymers can achieve extremely high doping levels approaching one charge per repeating unit. Furthermore, the doping level in conducting polymers can be adjusted in various ways after fabrication, enabling their use in devices such as electrochemical transistors, electroactive actuators, and tunable metasurfaces.

Poly(3,4-ethylenedioxythiophene) (PEDOT) is one of the most studied conducting polymers due to its stability and high transparency in its conductive state. The optical properties of PEDOT can be modulated through electrochemical doping, making it suitable for dynamic color-changing devices[289,290]. Moreover, PEDOT can switch between insulating and conductive states through electrochemical doping/dedoping reactions, which allows for the dynamic tuning of metasurface properties, such as extinction, reflectivity, and absorption, making PEDOT suitable for applications in adaptive optics. Jonsson's group demonstrated the use of PEDOT:Sulf nanoantennas for dynamic organic plasmonics[291,292]. They prepared thin PEDOT:Sulf films using vapor phase polymerization followed by sulfuric acid treatment to achieve high electrical conductivity exceeding 5000 S/cm. These PEDOT:Sulf films exhibit a negative real permittivity in the spectral range from 0.8 to 3.6 μm, indicating plasmonic behavior resulting from the high concentration of mobile positive polaronic charge carriers in the polymer network[291]. When the PEDOT:Sulf film was patterned into periodic PEDOT:Sulf nanodisks using colloidal lithography, pronounced localized surface plasmon resonances (LSPRs) were observed in the infrared ranges, which can be tuned through chemical redox reactions. For instance, exposing PEDOT:Sulf nanodisks to the vapor of highly branched poly(ethylenimine) (PEI) can reduce the charge carrier concentration in PEDOT, effectively switching PEDOT between plasmonic and insulating states. Since chemical tuning is not very convenient for most applications, the authors later developed electrical tuning of PEDOT:Sulf nanoantennas[292]. As shown in Fig. 9(a), the device consists of PEDOT:Sulf nanodisks on an ITO/glass substrate, which is coated with an ion gel and a second ITO/glass substrate as the top electrode. This setup allowed for the electrochemical modulation of the redox state of the polymer, enabling reversible switching of its plasmonic properties. The extinction spectra showed that the resonance peak observed at around 1800 nm for the oxidized state could be entirely suppressed by applying a positive bias, demonstrating excellent reversibility over multiple cycles [Fig. 9(a)]. Beyond binary switching, they also demonstrated the ability to gradually tune the plasmonic response of PEDOT:Sulf nanoantennas. A continuous suppression of the plasmonic resonance, accompanied by a small red shift of the extinction peak, was achieved by applying different biases. To eliminate the need for additional electrodes that typically obstruct optical performance, Kang *et al.* explored the development of electrically tunable and electrode-free metasurfaces by utilizing an inverted nanoantenna array design of PEDOT:Sulf[293]. They employed a nanofabrication method known as solvent-assisted nanoscale embossing followed by reactive ion etching, which allows for the precise creation of both regular and inverted nanoantenna arrays with high resolutions. The fabricated inverted nanorod (INR) arrays demonstrated polarization-dependent extinction peaks, primarily determined by the gap between apertures and thus influenced by the size and periodicity of the apertures. As shown in Fig. 9(b), the device features a continuous, in-plane configuration that enables direct electrical connection. By applying voltages of 0 and −5 V repeatedly, the optical properties of the PEDOT:Sulf film transitioned between oxidized (doped) and reduced (undoped) states. This transition facilitates the reversible switching of the plasmonic resonance of the PEDOT:Sulf INR array, with the extinction spectra showing significant changes based on the applied voltage. The ability to dynamically modulate these properties without extra electrodes enhances the device's applicability in many optoelectronic applications.

In addition to the simple tuning of extinction spectra, Giessen's group has presented significant advancements in dynamic metasurfaces using electrically switchable plasmonic nanoantennas made from conducting polymers[294]. They explored the use of poly(3,4-ethylenedioxythiophene):polystyrene sulfonate (PEDOT:PSS) for creating nanoantennas by alternate lithographic processes that require multi-step indirect patterning and dry etching, which can reversibly switch between metallic and insulating states when PEDOT:PSS is subjected to an electrochemical redox reaction [Fig. 9(c)]. When a voltage of +1 V is applied, PEDOT:PSS becomes doped and exhibits metallic properties, supporting strong plasmonic resonances at around 2.2 μm. Conversely, applying a voltage of −1 V reduces the polymer, rendering it insulating and effectively turning off the plasmonic resonance. This switching occurs rapidly, with a

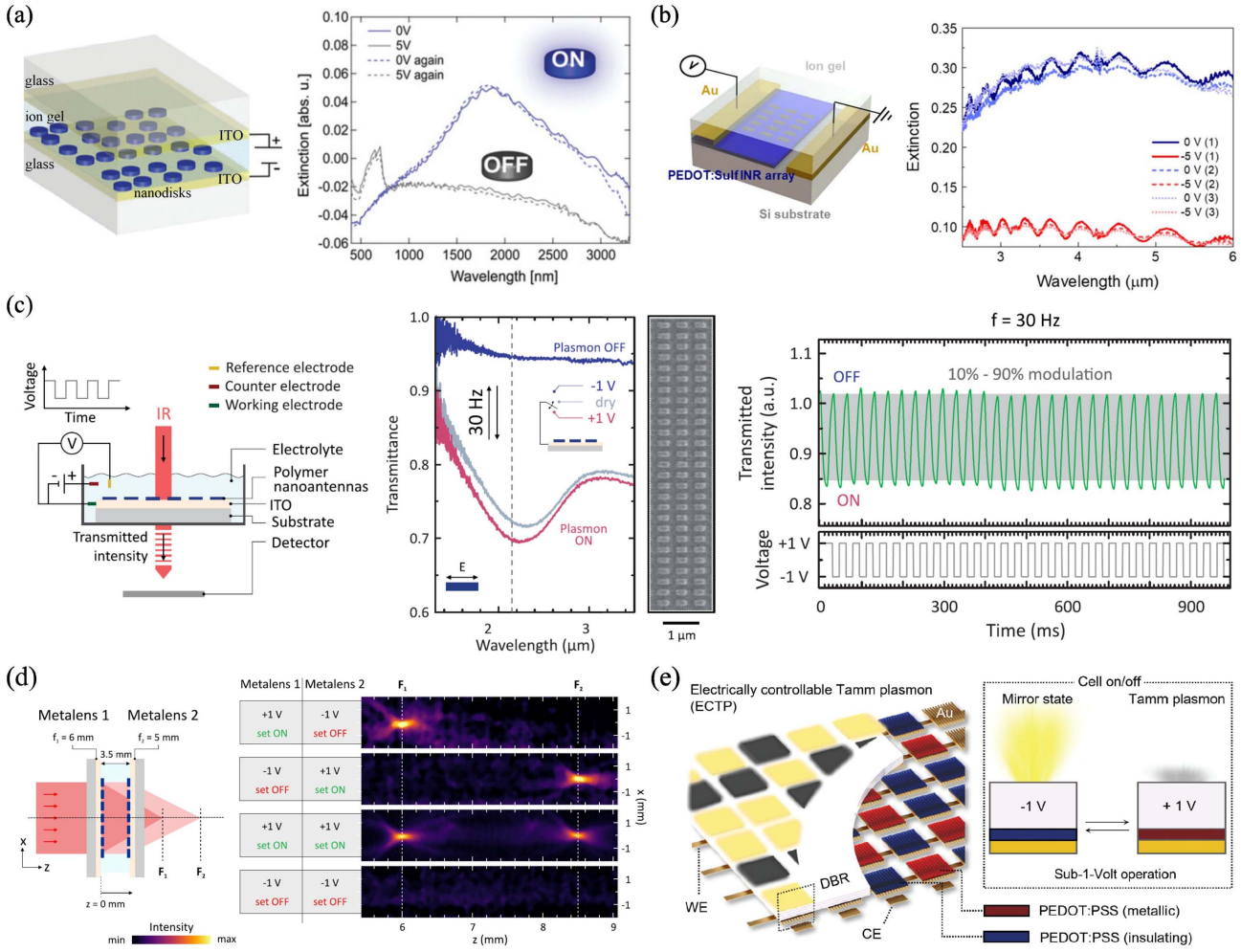

Fig. 9 Electrochemically activated metasurfaces based on conducting polymer PEDOT. (a) Electrochemically activated PEDOT:Sulf nanoantennas for tunable extinction. Extinction spectra of a nanodisk array with a thickness of 65 nm, a diameter of 145 nm, and an array period of 600 nm on the counter ITO electrode, where on and off plasmonic resonance was switched at the electrical bias of 0 and 5 V. Adapted with permission from Ref. [292] © John Wiley and Sons. (b) Electrode-free PEDOT:Sulf INR arrays for electrically tunable extinction. Plasmon resonance of an INR array was switched OFF and ON by applying voltages of –5 and 0 V repeatedly. Adapted with permission from Ref. [293] © Royal Society of Chemistry. (c) Electrically switchable PEDOT:PSS nanoantennas. Plasmonic resonance of fabricated PEDOT:PSS antennas was completely tuned ON and OFF with applied voltages of +1 and –1 V, respectively, with a modulation frequency of up to 30 Hz. Adapted with permission from Ref. [294] © AAAS. (d) Electrically switchable metaobjective comprising two PEDOT:PSS metalenses. The metaobjective allows for four different states depending on the individual voltage applied to the polymer metalens. Adapted with permission from Ref. [297] © Springer Nature. (e) Electrically controlled near-infrared optical modulator by coupling Tamm plasmon to PEDOT:PSS. Optical modulation depth exceeding 88% was achieved under low voltages of ±1 V. Adapted with permission from Ref. [298] © John Wiley and Sons.

rise time of 20.8 ms and a fall time of 9.1 ms, equivalent to a duty cycle time of 29.9 ms, corresponding to a maximum switching frequency of 33 Hz. The nanoantennas could endure multiple switching cycles (260 cycles) with minimal degradation. This breakthrough enables dynamic control of optical properties at video-rate frequencies, paving the way for applications in high-resolution augmented reality, virtual reality, and other optoelectronic devices. As a proof of concept, they implemented electrically switchable beam steering with a 100% contrast ratio between the diffracted beam intensities in the metasurface ON and OFF states, superior to the design that combines Au nanoantennas and an electropolymerized PEDOT[295]. The metasurfaces, composed of PEDOT:PSS meta-atoms with different orientations to supply the PB phase, diffracted the cross-polarized component to an angle of +10.2° when illuminated with a CP light for an applied voltage of +1 V, corresponding

to the ON state. On the contrary, a voltage of −1 V turns the metasurface completely OFF, and the diffracted beam at +10.2° vanishes completely. Intriguingly, intermediate states could be realized by successive electrochemical doping, allowing the intensity of the diffracted beam to be gradually modulated. Dynamic control over multiple diffraction angles was also possible by incorporating two electrically switchable metagratings placed on electrically isolated areas, where each metagrating has a different superlattice period to produce distinct diffraction angles[296]. The device demonstrated three distinct states of beam diffraction based on the applied voltages: large-angle diffraction (33.5°) when the left grating is ON and the right is OFF, small-angle diffraction (16°) when the right grating is ON and the left is OFF, and no diffraction when both gratings are OFF. Leveraging the reversible metal-to-insulator transition of PEDOT:PSS, they have developed a conducting polymer metalens that can be dynamically switched ON and OFF with low voltages of ±1 V by precisely controlling the rotation angle of nanoantennas to obtain a quadratic phase profile[297]. When the metalens was ON with an applied voltage of +1 V, a focal spot was obtained at the working wavelength of 2.65 μm. Notably, the metalens exhibited hysteresis behavior, allowing it to remain in either the ON or OFF state at 0 V, depending on the preceding voltage. This hysteresis enables non-volatile operation, which is energy-efficient and ideal for applications requiring stable optical states without a continuous power supply. They extended the concept further to create a metaobjective composed of two independently switchable metalenses (metalenses 1 and 2 with focal lengths of 6 and 5 mm, respectively), which are mounted on an ITO-coated substrate. The separation between two metalenses is filled with an electrolyte layer of 3.5 mm to facilitate electrochemical switching. As shown in Fig. 9(d), by adjusting the voltages applied to each polymer metalens of +1 V or −1 V, four distinct states were successfully achieved: single focus in the focal plane F_1 ($z = 6$ mm) or F_2 ($z = 8.5$ mm), a dual-focal state with spots in both planes F_1 and F_2, and an OFF state with no focal spots.

Despite achievements, the previously designed PEDOT:PSS meta-atoms suffer from limited modulation depths[294–297]. To overcome this limitation, Ko *et al.* introduced an electrically switchable optical modulator with a near-unity optical modulation under a low operation voltage in the telecom range using Tamm plasmon coupled with PEDOT:PSS[298], which addresses key challenges in high-density optical interconnects, photonic switching, and memory applications. As displayed in Fig. 9(e), the electrically controllable Tamm plasmon (ECTP) array consists of a DBR, a PEDOT:PSS active layer, and an Au membrane. Each ECTP cell is equipped with a working electrode (WE) and a counter electrode (CE), allowing to precisely control the reflectivity by adjusting the applied voltage between +1 V and −1 V. The DBR consists of alternating SiO_2 and silicon nitride (SiN) layers, which create a necessary optical stop band for the Tamm plasmon resonance. The modulation mechanism relies on the electrochemical doping and dedoping of PEDOT:PSS, which switches the polymer between metallic and insulating states. When a positive voltage (+1 V) is applied, PEDOT:PSS becomes doped, increasing its carrier density and making it metallic. In contrast, a negative voltage (−1 V) reduces the polymer, turning it insulating. This switching modulates the plasmonic resonance, enabling the device to transition between high reflectance (ON state) and high absorption (OFF state). The device achieves an exceptional modulation depth of 88% experimentally at the wavelength of 1500 nm, with theoretical projections exceeding 99%, attributed to the strong light confinement at the DBR/PEDOT:PSS interface, facilitated by the Tamm plasmon mode. Moreover, the proposed optical modulator can be easily scaled to work across a broad spectral range from 800 to 2500 nm, making it suitable for various near-infrared applications. The switching speed of the ECTP is mainly determined by the ion exchange rate in the PEDOT:PSS layer. Although incorporating a porous Au membrane could significantly enhance ion transport and thus reduce the switching time, this ECTP still exhibits slower switching speeds (~30 ms in a dedoping and doping duty cycle) compared to other active materials like PCMs or electron density tuning materials. The ECTP's hysteresis behavior under cyclic voltage allows for its application in optical memory devices. They demonstrated a programmable memory cell capable of multi-level data storage, whereby electrical pulses with positive and negative potentials define the information state. By applying different voltage sweeps, the device can encode and decode binary information, showcasing its potential for rewritable optical memory applications.

Polyaniline (PANI) is another widely used conductive polymer due to its low loss, high stability, and facile synthesis[299]. PANI experiences significant changes in its refractive index, especially in the imaginary part[300,301], when electrochemically switched between its oxidized form [emeraldine state (ES)] and reduced form [leucoemeraldine state (LS)] with an applied voltage. In the ES form, PANI exhibits strong absorption, whereas in the LS form, it has minimal absorption in the visible and near-infrared wavelengths. The electrochemical switching of PANI occurs at an ultrafast speed of approximately 1 μs and can withstand more than switching 10^5 cycles without degradation. These properties make PANI an ideal material for electrically controlled metasurfaces with active responses[301–308]. For example, switchable plasmonic colors were realized by coating plasmonic nanocrystals with PANI[303–307]. To explore the functionalities beyond spectral tuning, Liu's group utilized a complicated metasurface design with preselected Au antennas locally conjugated with PANI[301]. As illustrated in Fig. 10(a), the metasurface consists of two sets of Au nanorods that are alternatively arranged in odd and even rows on an ITO-coated substrate based on the PB phase. The Au nanorods in even rows are conjugated with PANI, acting as the active pixels, whereas the Au antennas in odd rows are embedded in PMMA as static pixels. When PANI is close to its LS form with no absorption, the anomalous transmission approaches zero due to the destructive interference of the scattered light from the neighboring rows with a relative orientation of $\Delta\theta = 90°$. When PANI transits to its ES form with increased absorption, the anomalous transmission gradually increases and eventually reaches a maximum intensity. In the experiment, PANI was grown on preselected Au nanorods using an electrochemical polymerization process in an aqueous electrolyte, which was monitored in real time using cyclic voltammetry, ensuring precise control over the PANI thickness. The optimal thickness of PANI was found to be around 50 nm, which allowed for high-intensity contrast switching with a ratio of up to 860:1 at the wavelength of 633 nm [Fig. 10(a)]. The switching speed was around 35 ms, and the device showed excellent reversibility over more than 100 switching cycles without significant degradation. They also showcased the practical applications of addressable metasurface holography, where two holographic images of "L" and "R" could be switched on and off independently.

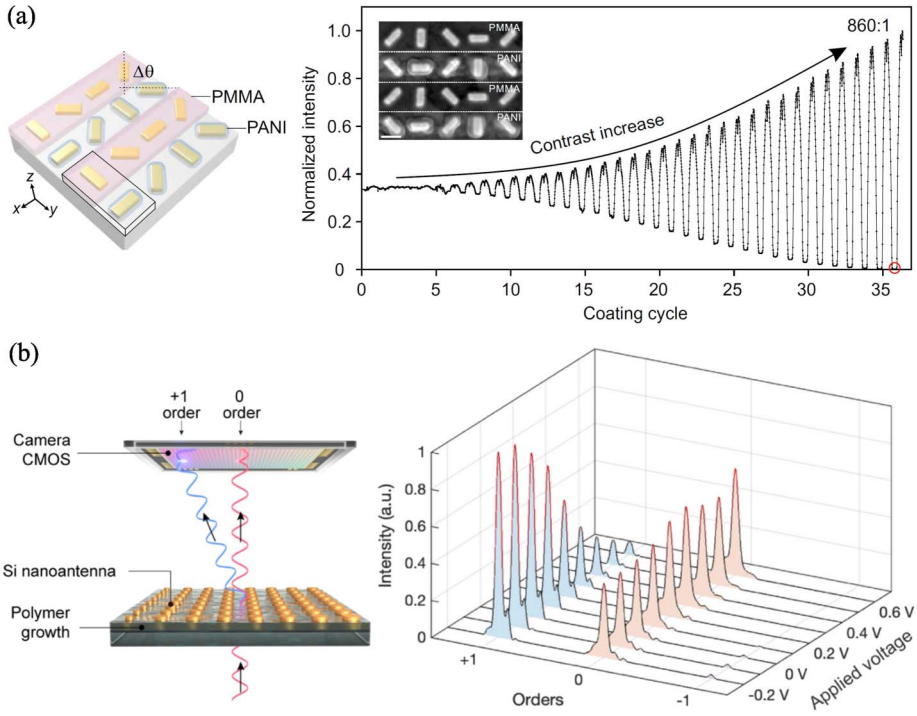

Fig. 10 Electrochemically activated metasurfaces based on conducting polymer PANI. (a) Electrochemically controlled visible metasurfaces with high-contrast switching through in-site optimization. A maximum intensity contrast was achieved by selectively and locally coating PANI on Au antennas with 36 cycles. Adapted with permission from Ref. [301] © AAAS. (b) Active Huygens' metasurface based on *in-situ* grown PANI. Intermediate PANI states with gradually varied refractive indices could be addressed via voltage tuning, enabling the continuous modification of the intensity distributions between the +1st and zeroth diffraction orders. Adapted with permission from Ref. [308] © De Gruyter.

Based on *in-situ* grown PANI, Lu *et al.* demonstrated an electrically switchable Huygens' metasurface with high-performance metrics, including fast switching speed, high modulation contrast, and long-term durability[308]. The metasurface consists of dielectric Si nanodisks surrounded by a layer of PANI. The PANI layer was grown *in-situ* using electrochemical polymerization, ensuring strong mechanical and electrical contact between the polymer and the Si nanoantennas, which can not only simplify the fabrication process but also enhance the durability and performance of the metasurface. The modulation mechanism also relies on the redox reaction of PANI, which switches between ES and LS forms, resulting in significant changes in the refractive index. At +0.6 V, PANI is in its oxidized state with strong absorption, while at −0.2 V, it is in its reduced state with minimal absorption. As a proof of concept, the researchers implemented the phase-gradient metasurface for active beam steering, in which the intensities between zeroth and +1st diffraction orders were controlled by the applied voltage, as shown in Fig. 10(b). A high modulation contrast of over 1400% was measured for the +1st order between two states, which is significantly higher than previous polymer-based metasurfaces[294,301]. The diffraction efficiency reaches up to 28%, 25 times higher than similar devices[294,295,309], attributed to the careful design of the Huygens' nanoantennas and the strong interaction between the PANI layer and dielectric nanodisks. The switching speed of the metasurface is around 60 frame/s, with a rise time of 14.1 ms and a fall time of 11.7 ms. The device shows excellent stability, maintaining performance over 2000 switching cycles without noticeable degradation, owing to the solid contact between the PANI and the nanoantennas.

Electrochemically activated dynamic metasurfaces offer several advantages, including precise control over optical properties through electrochemical modulation, allowing for reversible changes in response to applied electrical signals. This tunability facilitates diverse applications, from color display and beam steering to tunable lenses and holography. Additionally, the use of electrochemical processes can enable low-power operation and integration into compact devices. However, the complexity of fabrication, involving precise material deposition and integration, can be costly and time-consuming. Material stability under repeated electrochemical cycling is a concern, as it may lead to degradation over time, affecting long-term reliability. Furthermore, the range of tunability is often limited by the inherent properties of the materials used, and maintaining consistent performance across different environmental conditions can be challenging. Despite these limitations, the outlook for electrochemically activated dynamic metasurfaces is promising. Ongoing research focusing on improving material stability, expanding tunability, and developing more efficient fabrication techniques will unlock new possibilities in photonics and other fields, driving the development of versatile electrochemical metasurface-based technologies.

5 Electrically Tunable Metasurfaces Based on 2D Materials

2D materials consist of single or few layers of atoms and include substances such as graphene, its derivatives, and transition metal dichalcogenides (TMDs) like molybdenum disulfide (MoS_2), tungsten disulfide (WS_2), and molybdenum diselenide ($MoSe_2$), as well as black phosphorus, among others[145,146,149]. Due to their atomically thin structures and electrically tunable bandgaps, 2D materials can be heterogeneously integrated with ultrathin, flat-form-factor metasurfaces to create electrically tunable hybrid metasurfaces[151]. Furthermore, the versatile resonances supported by the designer metasurfaces can significantly enhance the interaction between light and 2D materials, thus achieving efficient light modulation. In addition to hybrid metallic and dielectric metasurfaces integrated with 2D material, the materials themselves can be engineered into electrically tunable atomic-layer metasurfaces, leveraging mechanisms such as carrier-injection tunable graphene plasmons, tunable exciton resonances, and others[147,148,150].

5.1 Electrically Tunable Metasurfaces with Continuous Graphene Layers

Due to its ultrafast carrier mobility, continuous graphene layers can be integrated with metallic or dielectric meta-atoms to realize tunable metasurfaces with ultrafast modulation on the sub-picosecond level, driven by an electrical stimulus. Through an electrical gating that adjusts the Fermi level of the graphene layer, the optical responses are dynamically tuned. This tuning mechanism relies on an electrically tunable carrier density, which, in turn, alters the complex refractive index. Consequently, this modifies the resonance properties of the metallic/dielectric antenna arrays and thus naturally affects the optical response[310]. In 2014, Capasso's group showcased a significant technological advancement with graphene-activated tunable plasmonic metasurfaces over a 5–7 μm wavelength range[311]. They demonstrated a tunable metasurface perfect absorber in reflection, composed of an Au antenna array (30 nm thick) on graphene, an Al_2O_3 dielectric layer (300 nm thick), and a thick Al substrate (300 nm thick), forming an asymmetric subwavelength-thick FP cavity [Fig. 11(a)]. By varying the gate voltage applied to the graphene, the absorber can switch in and out of a critical coupling condition, achieving a modulation depth of up to 95% (defined by $1-|R_{\min}/R_{\max}|$, where $R_{\min}$ and $R_{\max}$ are the minimum and maximum achievable reflectivities, respectively) at $\lambda = 6$ μm with a gate voltage change of 80 V. This technology allows for ultrathin, high-speed (20 GHz) optical modulators and can be scaled from infrared to terahertz wavelengths. Notably, this configuration was later extended to the near-infrared spectrum (1.55 μm) and demonstrated as feasible for low-pump-fluence all-optical modulation with ultrafast modulation speeds (picosecond scale), benefiting from graphene's ultrafast photocarrier relaxation time[312]. In 2015, Shvets's group experimentally demonstrated a reflective intensity modulator by integrating graphene with plasmonic Au metasurfaces that exhibit Fano resonances, achieving efficient electrical switching of infrared light, as shown in Fig. 11(b)[313]. The electrically controlled plasmonic response of graphene in the Pauli blocking regime leads to strong spectral shifts of the Fano resonances without inducing additional nonradiative losses. Coupled with the narrow spectral width of the Fano resonance, this configuration enables reflectivity modulation of about 10 dB [defined by $10\lg(|1-R_{\text{off}}/R_{\text{on}}|)$, with $R_{\text{on}} \approx 19\%$, and $R_{\text{off}} \approx 1.9\%$] at the wavelength of ~7 μm. Apart from intensity modulation, graphene-tunable plasmonic metasurfaces are also explored for their capability in dynamic phase manipulation[314,315]. For example, in 2017, Atwater's group demonstrated a simple configuration consisting of a rectangular Au nanoantenna array with a graphene layer atop a SiN_x-coated Au reflector, as illustrated in Fig. 11(c)[315]. This configuration achieved significant phase modulation in reflection across the mid-infrared spectrum ($\lambda = 8$–9 μm). By adjusting the Fermi energy of graphene through electrostatic gating, the metasurface can dynamically modulate the phase of reflected light over a broad range, specifically achieving phase shifts of 206° and 237° at wavelengths of 8.70 and 8.50 μm, respectively.

Following this concept, various nanoantennas with distinct resonances and functionalities have been studied. For instance, Yuan's group theoretically explored a graphene-activated metasurface capable of alternating between being a perfect absorber and a reflective polarization converter with high efficiency (>90%) at 1550 nm in 2023[316]. The modulator employs an FP-like nanostructure with an elliptically patterned anisotropic nanohole antenna array, which supports GMRs to enhance the modulation capabilities of graphene. In 2024, Feinstein and Almeida demonstrated a graphene-metal hybrid metasurface that supports tunable hybrid graphene-Au plasmons for active control of mid-infrared radiation[317]. They engineered this by depositing Au nanorods on graphene sheets, creating localized surface plasmons that couple with graphene's plasmons to enhance their interaction and resonance strength. Experimentally, they demonstrated a modulation rate of 17% [defined as $1-T(E_F)/T_{\text{CNP}}$, where $T(E_F)$ and T_{CNP} represent the transmittances at Fermi level E_F and at the charge neutrality point (CNP, $E_F = 0$ eV), respectively] at a wavelength of 11.5 μm, achieved with only a modest 0.35 eV chemical doping. Note that reflective graphene-tunable metallic/dielectric metasurfaces are primarily based on asymmetric FP cavities, each comprising a back reflector, a dielectric spacer, an electrically controlled graphene layer, and versatile nanoantenna arrays. These antenna arrays feature different configurations such as periodic Au nanobrick antenna arrays (in experiment, $\lambda = 2$–6 μm)[318], split-ring Au nano-resonators (in experiment, $\lambda = 5$ μm)[319], combined Ag split-ring resonators (SRRs) and inductance-capacitance (LC) resonators (in simulation, $\lambda = 6$ μm)[320], combined PMMA dielectric gratings with lithium niobate (LN) for dynamically controlled GMRs (in simulation, $\lambda = 800$ nm)[321], and silver grating (in simulation, $\lambda = 6.78$ μm)[322].

In addition to reflective-type, transmission-type graphene-tunable hybrid metasurfaces have also been investigated. In 2016, Atwater's group experimentally integrated graphene plasmonic ribbons (GPRs) with subwavelength metallic slit arrays to achieve electronically tunable extraordinary optical transmission, as depicted in Fig. 11(d)[323]. The graphene plasmonic ribbons are electrostatically tuned within the slits to modulate their resonant coupling with surface plasmons on the metallic layers, thereby dynamically controlling the optical transmission properties. This configuration achieved enhanced mid-infrared transmission modulation efficiency of 28.6% (defined by $1-T/T_{\max}$) at a specific wavelength of 1397 cm^{-1} (~7.158 μm), achieved by adjusting the Fermi energy of graphene between −0.353 eV (a maximum transmittance of

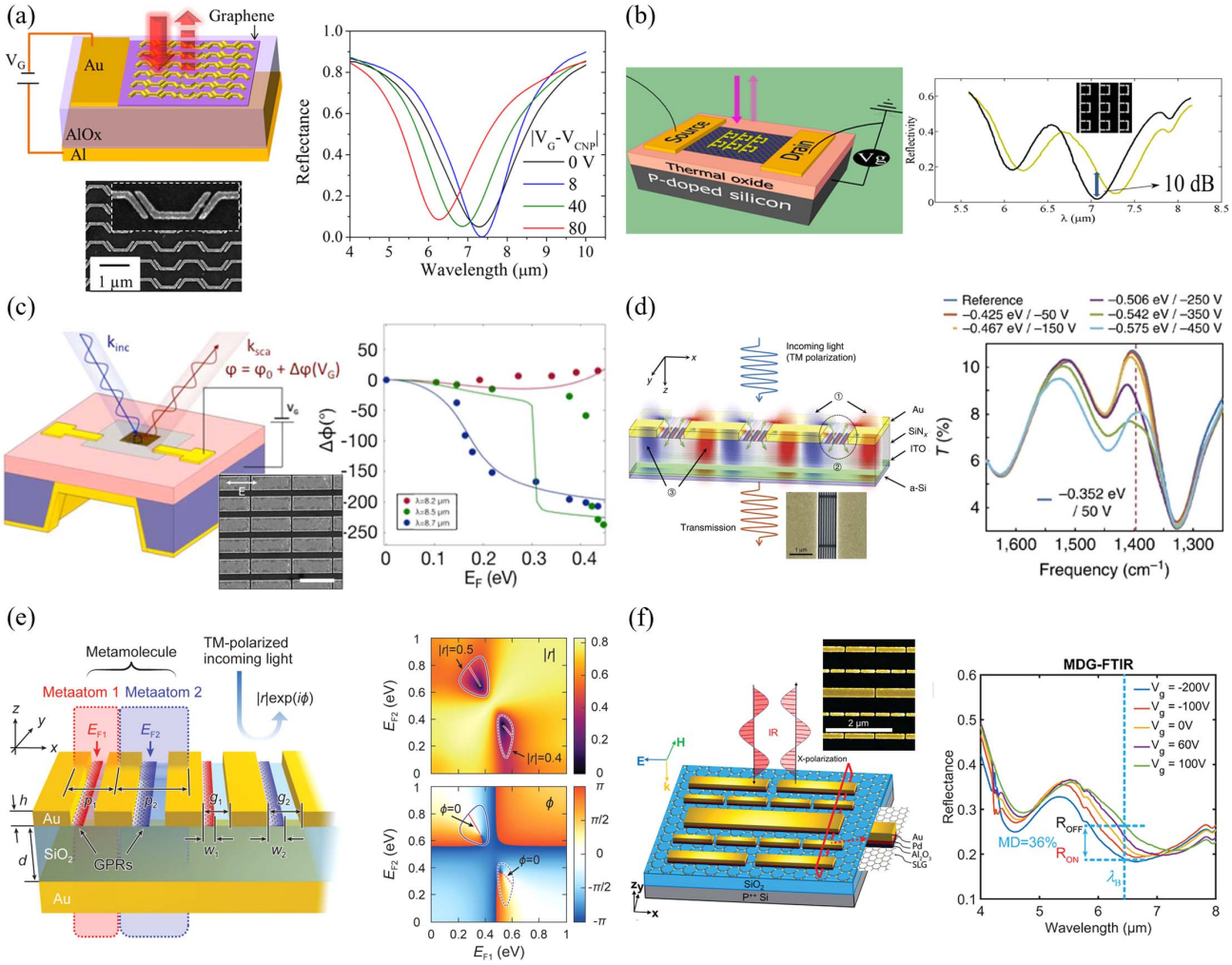

Fig. 11 Electrically tunable metasurfaces with continuous graphene layers. (a) Tunable metasurface absorber composed of a metasurface on graphene, an Al_2O_3 layer, and an Al substrate at the wavelength of 6.5 μm. Adapted with permission from Ref. [311] © ACS. (b) Reflective intensity modulator based on a Fano-resonant metasurface integrated with graphene at the wavelength of 7 μm. Adapted with permission from Ref. [313] © ACS. (c) Reflective phase modulator based on gate-tunable graphene-Au nanoantenna array at the wavelength of 8.5 μm. Adapted with permission from Ref. [315] © ACS. (d) Transmissive intensity modulator by coupling extraordinary optical transmission resonances to electro-statically tunable graphene plasmonic ribbons. Adapted with permission from Ref. [323] © Springer Nature. (e) Metamolecule composed of a pair of independently controlled gate-tunable graphene plasmonic meta-atoms for complete complex amplitude modulation at the wavelength of 7 μm. Adapted with permission from Ref. [325] © ACS. (f) Tunable mid-infrared multi-resonant graphene-metal hybrid metasurfaces. Adapted with permission from Ref. [327] © John Wiley and Sons.

∼10.7%) and −0.542 eV (a minimum transmittance of ∼7.6%), corresponding to gate voltages between 50 and −350 V. Potential modulation efficiencies up to 95.7% were demonstrated under optimal conditions in simulations. Some other possible configurations for transmissive graphene-integrated hybrid metasurfaces include single-layer graphene on top of nano-structured surfaces such as a Si photonic-crystal-like substrate[324].

To achieve more complex, independent control of amplitude and phase, multiple parameter control strategies are often required[325,326]. In 2020, Jang's group theoretically explored a novel approach for achieving complete complex amplitude modulation using graphene plasmonic metamolecules, as shown in Fig. 11(e)[325]. By integrating pairs of tunable graphene plasmonic ribbons with noble metal antennas, this metasurface can independently control both the amplitude and phase of light across a complete 2π range at a wavelength of 7 μm. This dual-parameter control is facilitated through the independent electronic tuning of the Fermi levels of two subwavelength scatterers within each metamolecule, offering a high degree of flexibility and precision for dynamic complex wavefront control at mid-infrared frequencies. Importantly, this configuration presents significant fabrication challenges, as both the graphene layer and the gold antenna layer must be precisely patterned, involving complex and labor-intensive fabrication processes.

In most graphene-integrated plasmonic metasurfaces mentioned earlier, the metallic nanoantennas are in direct contact with the graphene layer, leading to unintentional doping from the metal to graphene. This interaction can limit how effectively a bias voltage can tune the metasurface's permittivity. To address this issue, Janssens's group experimentally demonstrated the enhancement of tunable mid-infrared multi-resonant graphene-metal hybrid metasurfaces by integrating a thin Al_2O_3 barrier layer (10 nm thick) in 2024[327]. This design significantly minimizes electrical coupling between the metal and graphene, greatly improving the tunability of the resonances. As illustrated in Fig. 11(f), the dual-band resonance tuning exhibits a tuning range of ~500 nm for a resonance at $\lambda = 7.3$ μm, and ~120 nm for another resonance at $\lambda = 4.7$ μm.

5.2 Electrically Tunable Metasurfaces with Directly Patterned Graphene Meta-Atoms

Apart from integrating continuous graphene layers with meta-atoms, graphene itself can be crafted into nanoantennas to realize electrically tunable graphene metasurfaces. This capability stems from the existence of graphene plasmons[152,328–334], which can strongly couple with incident electromagnetic waves with low losses and high spatial confinement, offering fascinating light control in the mid-infrared (MIR) and terahertz (THz) spectrum ranges. Unlike conventional metallic plasmonic metasurfaces, which are inherently static, graphene metasurfaces provide tunability through electrically adjustable optical permittivity. By controlling the carrier density through electrostatic gating, the resonance frequency, damping rate, and propagation length of graphene plasmons can be dynamically tuned, facilitating the design of innovative dynamic metasurfaces. For instance, experimental evidence has demonstrated that the plasmonic resonances of patterned graphene nanodisks and nanorings can be significantly tuned around a wavelength of 3.7 μm[335]. This tunability of graphene plasmons allows for actively controllable and enhanced absorptance, making them suitable for applications in ultracompact intensity modulators[336]. Due to significantly increased losses of graphene plasmons in the visible spectrum, these metasurfaces are most effective in the MIR to THz regimes[337–345]. In 2015, Liu's group conducted a simulation study on graphene plasmonic metasurfaces for dynamic wavefront shaping in the reflection within the MIR spectrum ($\lambda = 25$ μm)[337]. The metasurface consists of patterned graphene ribbons on a dielectric/metal substrate, forming a MIM configuration, where the width of the graphene ribbons is designed for phase engineering. By varying the Fermi energy of graphene through electrical gating, the efficiency of a tunable reflective focusing graphene metalens can be dynamically manipulated [Fig. 12(a)]. Almost concurrently, Tian's group numerically reported the potential for dynamically tunable transmissive anomalous refraction using graphene metasurfaces in the infrared spectrum, as illustrated in Fig. 12(b)[339]. These metasurfaces, composed of periodically patterned graphene nano-crosses, support plasmonic resonances at the MIR spectrum ($\lambda = \sim 17.6$ μm) and are encoded with geometric phases, specifically designed to manipulate CP light. By adjusting the Fermi energy of the graphene from 0.75 to 1 eV, they demonstrated that the anomalous refraction efficiency of the phase-gradient graphene metasurface could be optimized across different wavelengths from ~17.6 to ~20.7 μm, thereby broadening its effective operational bandwidth. Furthermore, by arranging gradient graphene nano-crosses on a dielectric-separated thick Au substrate, they theoretically demonstrated the ability to dynamically switch high-order anomalous reflection on and off at the wavelength of ~8 μm by varying the Fermi energy of graphene between 0.95 and 0.8 eV [see Fig. 12(c)][341]. In another simulation study shown in Fig. 12(d),

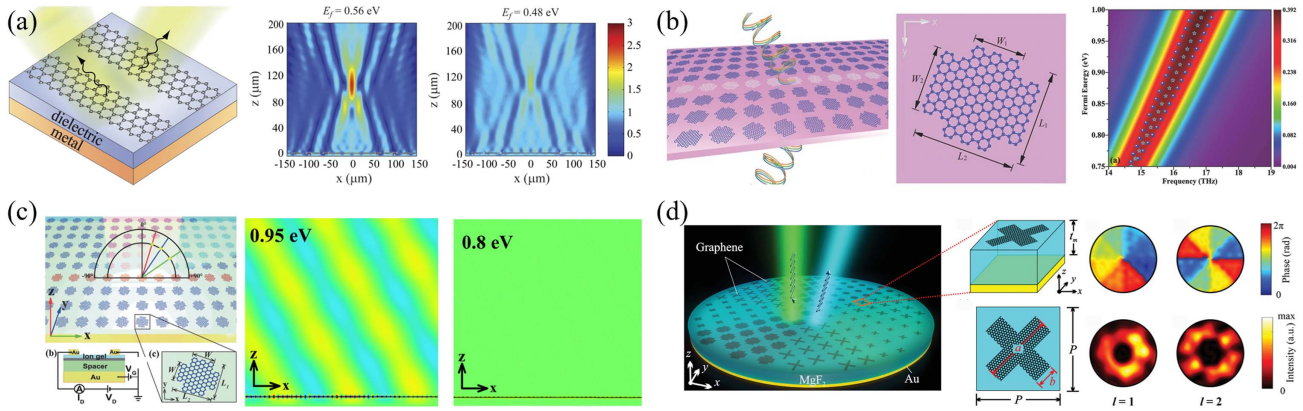

Fig. 12 Electrically tunable metasurfaces with directly patterned graphene meta-atoms. (a) Reflective graphene plasmonic metasurfaces comprising subwavelength-patterned graphene ribbons on a dielectric/metal substrate for dynamic control over reflective wavefronts by modulating the plasmonic resonance through adjustment of graphene's Fermi level at the wavelength of around 20 μm. Adapted with permission from Ref. [337] © Springer Nature. (b) Transmissive graphene nano-cross metasurfaces for dynamically tunable broadband MIR anomalous refraction, operating at the wavelength of around 17 μm. Adapted with permission from Ref. [339] © John Wiley and Sons. (c) Reflective graphene metasurface for high-order anomalous reflection switching. Adapted with permission from Ref. [341] © John Wiley and Sons. (d) Reflective diagonal nano-cross graphene metasurfaces for tunable polarization-preserving vortex beam generation at the wavelength of 8 μm. Adapted with permission from Ref. [344] © John Wiley and Sons.

Chen *et al.* employed diagonal graphene nano-crosses to successfully generate polarization-preserving optical vortices, with tunable topological charges over a frequency range from 4.5 to 5.5 THz[344]. It is important to note that, to date, there is still a lack of experimental demonstrations of tunable graphene metasurfaces in the infrared spectrum. For motivational purposes, several experimental implementations in the terahertz range can be referenced[338,343,345].

In addition, graphene oxide, a derivative of graphene, can be used to enable dynamic metasurfaces. In 2021, Jia's group experimentally demonstrated a varifocal graphene oxide metalens capable of dynamically tuning its focal length to provide zoom imaging across the entire visible spectrum[346]. This metalens operates in transmission and achieves broad spectral coverage through the detour phase method (no graphene plasmons here). Constructed from graphene oxide (250 nm thick) on a polydimethylsiloxane (PDMS) substrate, the lens employs lateral stretching to tune focal lengths, offering a 20% tuning range for different wavelengths—specifically red (650 nm), green (550 nm), and blue (450 nm) light. In a related effort, the same group demonstrated dynamically switchable structural color using graphene and graphene oxide meta-pixels[347]. These meta-pixels consist of alternating graphene/graphene oxide and dielectric layers on an Ag-coated flexible substrate. They can dynamically and instantaneously switch colors by controlling light scattering to excite various modes, a capability enabled by the strong anisotropic optical properties of the graphene and graphene oxide meta-pixels.

5.3 Electrically Tunable Metasurfaces with Other 2D Materials

Besides graphene, the development of 2D materials has expanded well beyond, with many other 2D materials (also known as van der Waals materials) being explored to enable tunable metasurfaces. These materials offer versatile configurations and tuning approaches, including tunable excitonic effects in transition TMDs[150,348,349], tunable hybrid plasmon modes in black phosphorus carbide (b-PC)[350], anisotropic quantum well electro-optics in few-layer black phosphorous[351], and tunable tri-layer black phosphorus integrated FP cavities[352]. Benefiting from recent advances in the fabrication and transfer methods, electronic and optical properties, as well as electrical-tuning capabilities, the expansion of 2D-materials-integrated tunable metasurfaces allows for functionalities that are challenging with graphene alone, such as extending into the visible and near-infrared spectra, exploiting novel tunable excitonic mechanisms in TMDs, and utilizing tunable anisotropic 2D materials for dynamic polarization control.

In 2018, Ang's group introduced b-PC for creating tunable anisotropic plasmonic metasurfaces in transmission[350]. As shown in Fig. 13(a), the metasurface comprises back-gated b-PC nanoribbon arrays on a SiO_2/Si substrate, supporting hybrid plasmon modes within the wavelength range from 5 to 7.7 μm. These modes are related to a Fano resonance between the plasmons and infrared-active optical phonons in b-PC. Exhibiting anisotropic behavior, this resonance allows for distinct responses along different crystal orientations and can be finely tuned *via* electrical gating, thereby offering new possibilities for tunable anisotropic metasurfaces.

In addition to the plasmon modes supported by graphene and b-PC mentioned above, which have been widely investigated for enabling tunable metasurfaces, a novel exciton tuning effect is proposed to create mutable, flat meta-optics. In 2020, Brongersma's group demonstrated a breakthrough using exciton resonance tuning to develop a tunable, atomically thin transmissive zone plate lens made from a monolayer of WS_2[348]. In this WS_2, excitons, which are electron-hole pairs bound by the Coulomb force within semiconductors, dominate the optical properties. By applying electrical gating using an ionic liquid, they were able to switch the exciton resonances in WS_2 on and off, enabling substantial modulation of the focusing properties.

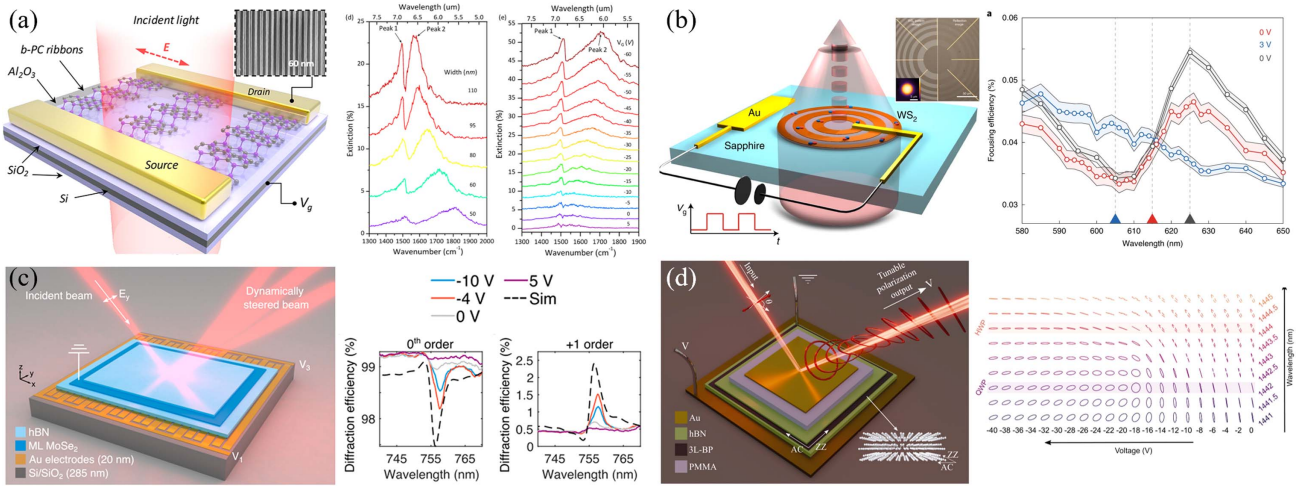

Fig. 13 Electrically tunable metasurfaces with other 2D materials. (a) Tunable Fano resonances by coupled plasmons and infrared-active optical phonon in back-gated b-PC nanoribbon arrays. Adapted with permission from Ref. [350] © ACS. (b) Tunable WS_2 zone plate metalens in transmission using excitonic resonance tuning effect. Adapted with permission from Ref. [348] © Springer Nature. (c) Exciton-based $MoSe_2$ metasurface for dynamic reflective beam steering. Adapted with permission from Ref. [349] © ACS. (d) TLBP-integrated FP cavity for dynamic polarization control in reflection. Adapted with permission from Ref. [352] © AAAS.

Operating within the visible spectrum, the lens demonstrated tunable focusing capabilities with a change in focusing efficiency from approximately 0.055% to 0.025% (corresponding to a modulation efficiency of 33% at $\lambda = 625$ nm) with a voltage change from 0 to 3 V [Fig. 13(b)], alongside a switching time of tens of milliseconds, with rise and fall time of 39 and 16 ms, respectively. Building on the theme of exciton resonance tuning, Atwater's group further advanced this area by introducing a method for dynamic reflective beam steering using an active van der Waals metasurface composed of unpatterned $MoSe_2$ on patterned Au electrodes in 2023[349]. They exploited the tunability of excitonic radiative and non-radiative rates within $MoSe_2$ *via* applied voltages to achieve significant changes in the complex refractive index. Experimentally, they demonstrated the capability to steer reflected light to angles ranging from $-30°$ to $+30°$ at a resonant wavelength of 757 nm, albeit with low efficiency ($\sim$1%) and modulation contrast, as shown in Fig. 13(c). Crucially, this approach obviates the need for fabricating patterned nanostructures, as the tunable phase gradient is directly dictated by the voltage profile applied to the $MoSe_2$.

Apart from dynamic wavefront engineering, tunable polarization control has also been explored on the van der Waals metasurface platform, utilizing tunable anisotropic 2D materials. In 2021, Atwater's group investigated the EO properties of trilayer black phosphorus (TLBP) integrated within an FP cavity[352]. This integration enables broadband polarization control across telecommunications wavelengths ranging from 1410 to 1575 nm. TLBP exhibits inherent birefringence and significant electrical tunability of its anisotropic refractive indices, enabling the dynamic manipulation of the polarization state of reflected light and covering nearly half of the Poincaré sphere, as displayed in Fig. 13(d).

Furthermore, the possibility of dynamic dispersion control has also been explored with tunable van der Waals metasurfaces. In 2023, Mosallaer's group theoretically proposed tunable pulse shaping using an all-dielectric metasurface enhanced by MoS_2[353]. The metasurface includes an array of TiO_2 nanobars coated with a MoS_2 layer and positioned over a DBR to enhance reflectivity. This configuration utilizes MoS_2 to actively control the temporal profile of optical pulses. It achieves electrically tunable phase modulation enhanced by quasi-bound states in the continuum (quasi-BICs), supported by the asymmetric TiO_2 nanobar array, which allows for dynamic adjustments of the phase and group delay dispersion properties.

Owing to their 2D flat form and rich physics underlying their tunability, 2D materials are inherently suitable for developing tunable metasurfaces. These can be achieved either by combining them with specifically designed dielectric or metallic metasurfaces or by patterning 2D materials themselves to create atomic-layer tunable meta-optics. Additionally, the rapid carrier dynamics of 2D materials such as graphene enable ultrafast responses, making them promising for ultracompact and ultrafast tunable meta-optics. However, the interaction of light with 2D materials is typically weak (especially in the high-frequency regime, such as the visible spectrum), necessitating carefully designed resonances (via either dielectric or metallic meta-atoms or 2D material meta-atoms) to enhance light–matter interaction and consequently, modulation efficiency. Moreover, selecting the appropriate 2D material for the targeted spectral regime is crucial; for instance, most graphene-based tunable metasurfaces are effective from infrared to terahertz spectra, owing to the tuning range of the carrier density. Lastly, it is important to note that both electronic and optical properties of single- or few-layer 2D materials are significantly influenced by environmental conditions, including temperature and humidity, and their long-term stability should also be investigated for further development.

6 Electrically Tunable Metasurfaces Based on TCOs

TCOs such as ITO, aluminum-doped zinc oxide (AZO), gallium-doped zinc oxide (GZO), and cadmium oxide (CdO) exhibit high transparency in the visible and/or infrared spectral ranges along with excellent electrical conductivity[152–155]. These properties make TCOs ideal for developing electrically tunable metasurfaces by leveraging their tunable refractive indices through carrier injection. TCO-enabled metasurfaces offer broad-range continuous tunability and high modulation speeds, owing to the carrier-density-tunable epsilon-near-zero (ENZ) phenomena and rapid carrier dynamics. Among all TCOs, ITO is the most widely utilized in developing tunable metasurfaces due to its tunable ENZ wavelength in the telecom range, superior optical and electrical properties, established technology, compatibility with other materials, and chemical and mechanical durability. By implementing an electrically gated metal-oxide-semiconductor (MOS) capacitor configuration (e.g., $Au/Al_2O_3/ITO$), it is possible to control carrier accumulation and depletion at the ITO/dielectric interface, thus modulating the permittivity of ITO through carrier-induced effects. The relationship between the permittivity and carrier density of ITO is typically described by the Drude model, while the inhomogeneous carrier distribution within the accumulation layer in ITO is analyzed using Poisson and drift-diffusion equations. Notably, the carrier density in ITO can be easily adjusted to achieve the ENZ phenomenon around a specific wavelength, typically in the near-infrared range. The ENZ phenomenon allows for strong electric field confinement at the ITO/dielectric interface, significantly enhancing light–matter interactions and enabling substantial tunability of the optical response. Apart from TCOs, the carrier-induced field effect in Si and gallium arsenide (GaAs) using p-i-n, p-n, or Schottky diode configurations can also be applied to add tunability to metasurfaces[354–359]. However, the maximum attainable refractive index change with these configurations is limited compared to TCOs, owing to lower carrier density and the absence of ENZ phenomena. To address this limitation, high-Q resonances and multiple cascaded p-i-n or p-n junctions have been proposed to enhance their tunability.

This section will focus on recent developments in TCO-integrated electrically tunable metasurfaces, which represent versatile metasurface configurations combining various resonances and MOS structure designs, utilizing both single and multiple gate-voltage-controlled approaches.

6.1 Electrically Tunable Metasurfaces with Single-Gated TCOs

To implement high-performance TCO-activated metasurfaces, it is important to properly design the resonance of meta-atoms to match the target operation wavelength while tuning the ENZ wavelength of the TCO through electrical gating to coincide with the resonance. The simplest configuration involves inserting a continuous ultrathin TCO layer into a MIM configuration, making conventional GSP metasurfaces active for

intensity[360–362], phase[363,364], and polarization[363,365–367] modulation. In 2015, Brongersma's group experimentally demonstrated electrically tunable light absorbers using Au GSP metasurfaces incorporated with thin ITO film at a wavelength of 3.8 μm, as illustrated in Fig. 14(a)[360]. The thicknesses of each layer in the metasurface are 50 nm (top Au), 6 nm (ITO), 20 nm [hafnium oxide (HfO_2)], and 50 nm (bottom Au), with the width and period of the top Au strip being 600 and 750 nm, respectively. By applying a voltage between +5 V (for carrier depletion) and −5 V (for carrier accumulation), the profile and mode index of the GSP mode could be dramatically changed reversibly, resulting in a large reflectance modulation (up to 15%, or a modulation ratio of $\Delta R/R = 35\%$). The operation speed was limited to 125 kHz due to the capacitance of the ITO/HfO_2/Au configuration and the resistance of the ITO layer. Beyond intensity modulation, they further investigated the dynamic phase control in reflection using a similar MIM configuration at the wavelength of 5.94 μm[363]. As shown in Fig. 14(b), this MIM configuration comprised a 50 nm thick Au nanostrip array (2.2 μm period), a 20 nm thick ITO layer, a 115 nm Al_2O_3 layer, and a 50 nm bottom Au layer. By tuning the carrier density in the ITO layer, the phase tuning range can reach up to 180°, thereby shifting the system between under-coupling ($V = -40$ V), critical coupling ($V = 0$ V), and over-coupling ($V = +40$ V) regimes.

Apart from uniform amplitude and phase modulation, Atwater's group reported individually addressable phase-gradient MOS-integrated MIM nanostrip arrays in 2016, which are composed of Au stripe antennas (250 nm wide, 50 nm thick, and 400 nm period), a 5 nm thick Al_2O_3 layer, a 20 nm thick ITO layer, and an 80 nm thick Au backplane[368]. By applying different voltages between each gold stripe antenna and the bottom Au layer, the carrier concentration at the Al_2O_3/ITO interface beneath each antenna can be independently controlled, thereby achieving tunable phase-gradient metasurfaces at the wavelength of 1550 nm. Notably, a phase coverage of 184° and a reflectance change of ∼30% were achieved by applying a gate bias of 2.5 V. In experiments, they demonstrated dynamic phase grating switching between zeroth and ±1st diffraction beams by electrically controlling subgroups of metasurface elements, with modulation frequencies reaching 10 MHz [Fig. 14(c)]. Furthermore, with an improved configuration consisting of 40 nm Au fishbone antennas (connected by gold

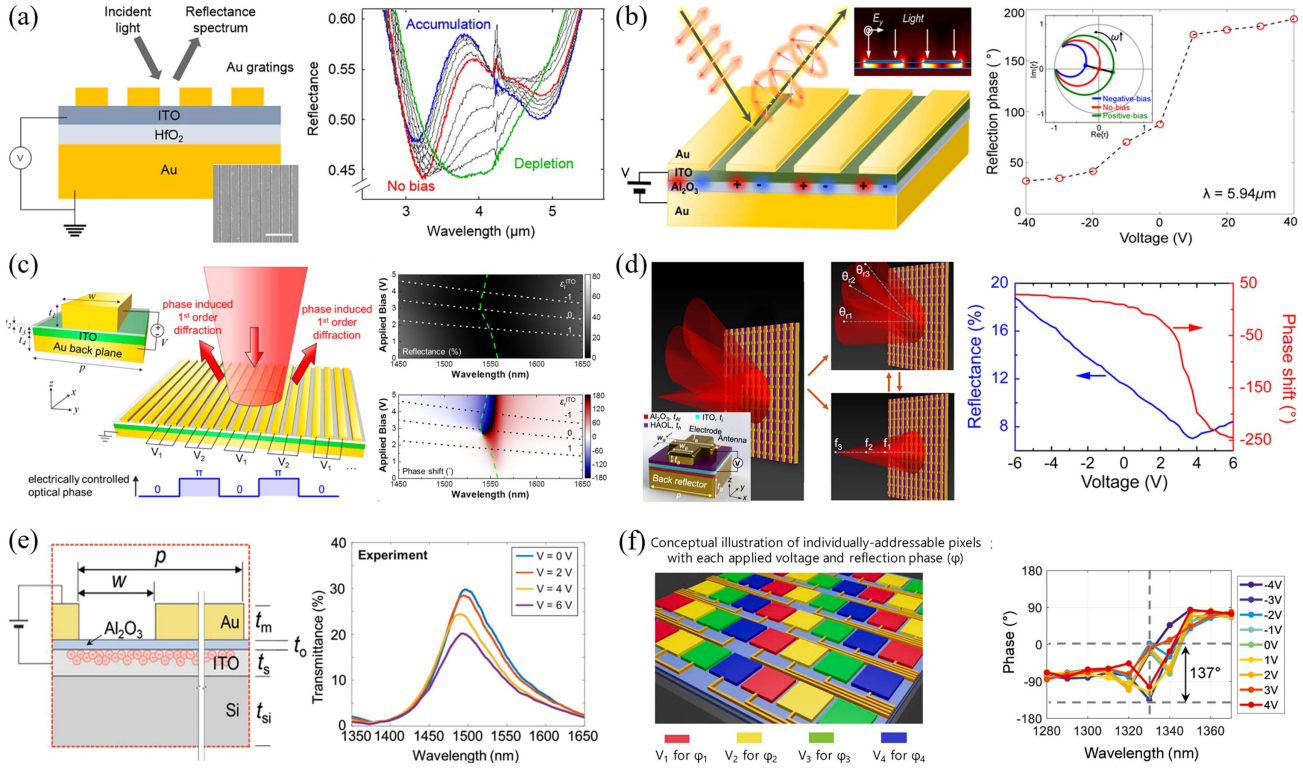

Fig. 14 Electrically tunable metasurfaces with single-gated TCOs. (a) ITO-integrated plasmonic absorber for amplitude modulation at $\lambda = 3.8$ μm. Adapted with permission from Ref. [360] © Springer Nature. (b) ITO-integrated nanostrip metasurfaces for dynamic phase and polarization control at $\lambda = 5.94$ μm. Adapted with permission from Ref. [363] © ACS. (c) Individually addressable nanostrip metasurfaces for 1D reconfigurable wavefront shaping at $\lambda = 1.55$ μm. Adapted with permission from Ref. [368] © ACS. (d) Tunable multifunctional metasurfaces consisting of individually addressable fishbone nanoantennas for 1D dynamic wavefront shaping at $\lambda = 1.522$ μm. Adapted with permission from Ref. [369] © ACS. (e) Transmission-type tunable ITO-integrated metasurface employing hybrid plasmonic waveguide mode at $\lambda = 1.5$ μm. Adapted with permission from Ref. [371] © John Wiley and Sons. (f) Pixelated ITO-integrated GSP metasurface for 2D beam steering at $\lambda = 1.3$ μm. Adapted with permission from Ref. [374] © De Gruyter.

stripes), 9.5 nm HfO_2/5 nm ITO/9.5 nm Al_2O_3, and an 80 nm Au back reflector, the same group achieved a significantly large continuous phase shift from 0° to 274° with applied gate voltages from 0 to 6.5 V at $\lambda = 1522$ nm, as displayed in Fig. 14(d)[369]. This large tunable phase shift offers the potential for dynamic wavefront shaping corresponding to multiple optical functions, such as 1D dynamic beam steering and cylindrical metalenses with reconfigurable focal lengths.

Besides operation in reflection, TCO-integrated transmissive metasurfaces have also been investigated. Various configurations have been studied, including a modified MIM structure with ITO and HfO_2 sandwiched between two Au strips[370], MOS structures placed on a Si substrate[371], and modified MIM with a hollow Au square instead of a continuous Au back reflector[372]. As an example, in 2020, Lee's group experimentally reported a gate-tunable ITO-integrated plasmonic metasurface for high-speed control of light transmission at 1550 nm[371]. As shown in Fig. 14(e), the metasurface consisted of a 40 nm Au nanoslit array (120 nm width and 900 nm period) atop a multilayer of 10 nm Al_2O_3, 20 nm ITO, and 140 nm α-Si on a quartz substrate. By adjusting the ITO's permittivity via a single gate voltage, the hybrid resonance formed by the coupling between the plasmonic mode from the Au pattern and the waveguide mode from the Si layer can be modulated, consequently altering the transmittance. In their experiment, a transmittance change of 33% was observed under a bias of 6 V, with a high modulation speed characterized by a 3 dB cut-off frequency of 826 kHz.

Most research on ITO-integrated metasurfaces has been conducted using 1D pixelated structures, which restricts their applicability to 1D light field control. To implement 2D programmable light field control, the only solution is to create 2D metasurface pixel arrays that can be individually addressed[373,374]. This remains challenging due to the densely packed arrays of nanoscale metasurface elements. In 2022, Kim *et al.* demonstrated a 10×10 independently addressable 2D metasurface pixel array with an overall size of $52\,\mu m \times 52\,\mu m$, as illustrated in Fig. 14(f)[374]. Each metasurface unit cell consists of a 50 nm Au nanoantenna, a 7 nm HfO_2 layer, a 1 nm Al_2O_3 layer, a 5 nm active ITO layer, a 1 nm HfO_2 layer, a 5 nm Al_2O_3 layer, and an Au mirror. By applying single gate voltages between the top Au antenna and the ITO layer (ranging from -4 to $+4$ V), they achieved a moderate tunable phase shift of 137° at $\lambda = 1330$ nm. Furthermore, they implemented dynamic beam steering over a range of ±7.3° in 2D space by applying different voltages to each of the 2D metasurface pixels.

For future reference, some relevant and motivating investigations on the tunable TCO metasurfaces are also listed here, including: (1) thermal robustness: studies on the thermal robustness of TCO metasurfaces under high-power irradiation with both continuous wave (CW) and pulsed laser illumination[375]. (2) Alternative TCOs: exploration of other conducting oxide materials such as CdO[375] and gallium-doped zinc oxide (Ga: ZnO)[376], targeting different wavelengths and higher speeds, among other benefits. (3) Versatile metallic meta-atom configurations: MIM meta-molecules with double-resonances for dual-band operation[377]; ITO gap-loaded gold dimer nanoantenna[378]; tunable dual-functional metasurfaces of MOS on a hyperbolic substrate for incident-angle multiplexed independent phase and amplitude modulation ($\lambda = 1450$ nm)[379]; ITO-integrated multi-resonant Al metasurface for broadband tunable absorber ($\lambda = \sim 1550$ nm)[380]. (4) Dielectric meta-atom configurations: ITO-integrated disc-shaped Si metasurfaces on an Au plate ($\lambda = 1100$ nm)[381]; ITO-perovskite barium strontium titanate (BST)-ITO nanoresonators supporting magnetic dipole resonances for enhanced amplitude modulation ($\lambda = 820$ nm)[382]; Si_3N_4 nanograting-Si-ITO-Al_2O_3-Au tunable GMR mirror structure for dual-band amplitude modulation ($\lambda = 1310$ and 1550 nm)[383]; Si nanograting-Al_2O_3-ITO intensity modulator in reflection ($\lambda = 1550$ nm)[384]; active quasi-BIC metasurfaces by integrating Si metasurfaces with ITO film (from 1300 to 1500 nm)[385].

6.2 Electrically Tunable Metasurfaces with Multi-Gated TCOs

Although single-gate-controlled MOS configurations feature an ultracompact, fast, and all-solid tunable metasurface solution, they exhibit limited tunability, with the amplitude and phase modulation intrinsically coupled. As an improvement to achieve larger and independent tunability of amplitude and phase, recently developed dual-gated and multi-gated controlled TCO metasurfaces offer significant advances. By employing dual-gated or multi-gated control, the range of tunability can be expanded, providing more precise and versatile modulation of the optical properties. In 2018, Mosallaei's group reported a numerical investigation of a tunable multi-gated ITO-assisted dielectric metasurface, as illustrated in Fig. 15(a)[386]. The metasurface consists of disc-shaped Si nanoantennas and multiple Al_2O_3/ITO layers on an optically thick Au substrate. By actively controlling the closely spaced electric and magnetic resonances in the Si nanoantennas with electrically controlled ITO layers under multi-gated biasing, a relatively high reflection amplitude of 0.4 over the entire phase-tuning coverage (~180°) in the near-infrared regime ($\lambda = \sim 1.4$ μm) was achieved. Based on the multi-gated ITO tunable dielectric meta-atoms, they theoretically demonstrated various optical applications using different biasing strategies, including reconfigurable polarizers (by applying an identical bias voltage to all meta-atoms), dynamic beam steering (using two-state biasing and a multilevel grating system), as well as controllable on- and off-axis focusing (through advanced element-by-element biasing). Utilizing a similar configuration without the Au back reflector, they investigated its potential for tunable phase engineering in transmission[387]. Furthermore, they numerically explored multi-gated ITO metasurface designs for amplitude/phase modulators and tunable phase-gradient components in the telecom wavelengths, using both dielectric[388,389] and metallic[390,391] meta-atoms supporting GMRs[388], decoupled gap plasmon resonances[390,391], and others[389]. The enhanced tunability by adopting a dual-gated ITO-integrated metasurface was first experimentally confirmed by Atwater's group in 2018[392]. They proposed a dual-gated reflectarray metasurface for achieving extensive (300°) phase tunability at the wavelength of 1550 nm. As shown in Fig. 15(b), the unit cell is composed of an 80 nm Al back reflector, a bottom 9.5 nm gate dielectric (composite HfO_2/Al_2O_3), a 5 nm ITO layer, another 9.5 nm gate dielectric, and a layer of 40 nm Al fishbone antenna on top. Two independent voltages can be applied between the ITO layer and the top fishbone antenna layer or the bottom Al back reflector, respectively, forming two independent voltage-controlled MOS channels at the top and bottom ITO/dielectric interface. Specifically, they achieved a continuous phase shift from 0° to 303° and a relative reflectance modulation of 89% under a ±6.5 V bias.

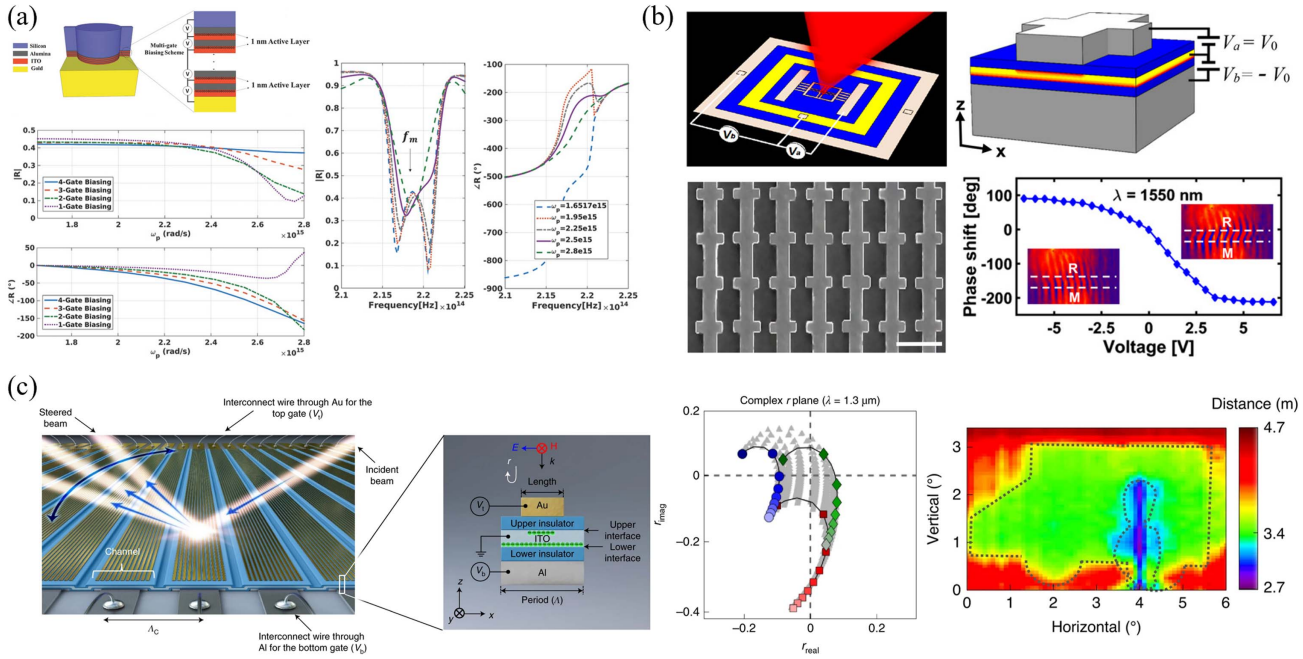

Fig. 15 Electrically tunable metasurfaces with multi-gated TCOs. (a) Multi-gated all-dielectric metasurfaces for dynamic polarization and 1D wavefront shaping at $\lambda = 1.4$ μm. Adapted with permission from Ref. [386] © John Wiley and Sons. (b) Dual-gated MIM metasurfaces with opposite top and bottom biases for enhanced (>300°) phase tunability at $\lambda = 1.55$ μm. Adapted with permission from Ref. [392] © ACS. (c) Dual-gated ITO-integrated MIM metasurface with different top and bottom biases for independent phase and amplitude control. A 3D depth image was produced using the ITO metasurface SLM. Adapted with permission from Ref. [393] © Springer Nature.

Besides enhanced tunability, the dual-gated TCO metasurface also provides possibilities for achieving independent phase and amplitude control based on a two-control-parameter approach[393]. In 2020, Park *et al.* reported a breakthrough in all-solid-state SLM based on an electrically tunable dual-gated ITO-activated metasurface, which enables independent control of the phase (full 360° coverage) and amplitude of reflected light at wavelengths of 1340 nm and 1560 nm, with a modulation speed of ~5.4 MHz. As shown in Fig. 15(c), the active metasurface consists of electrically tunable channels, each consisting of 11 individually addressable plasmonic nanoresonators. Each plasmonic nanoresonator (unit cell) comprises a 70 nm Au nanoantenna, a 5 nm ITO active layer sandwiched between two insulating layers composed of 1 nm Al_2O_3 and 7 nm HfO_3 layers, backed by an Al mirror. To achieve independent phase and amplitude control, they employed a two-control-parameter approach enabled by the versatile top and bottom gate-voltage combinations accessible in each unit cell. For proof-of-concept investigation, they demonstrated dynamic beam steering within a scan angle of 8°, achieving a detection range of up to 4.7 m in the 3D light detection and ranging (LiDAR) experiment.

Leveraging carrier-induced refractive index modulation at the ENZ condition accessible in TCO materials, metasurfaces with considerable tunability can be achieved through meticulously designed MOS-integrated meta-atoms. These designs simultaneously ensure efficient carrier injection and optical resonance of enhanced light–matter interaction. Notably, a TCO material thickness of just several nanometers is sufficient to boost the efficacy of solid-state TCO tunable metasurfaces. Additionally, the modulation of carriers within these nanometer-thin TCO layers can be extremely fast, with promising modulation speeds reaching up to GHz. Furthermore, the experimentally demonstrated capabilities of dynamic, independent amplitude and phase control through a dual-gated strategy inspire the development of other tunable metasurface configurations, incorporating multiple tuning parameters to achieve arbitrary complex amplitude dynamic control.

7 Electrically Tunable Metasurfaces Using EO Nonlinear Effects

In this section, we will discuss electrically tunable metasurfaces using EO nonlinear effects (i.e., Pockels and Kerr effects), encompassing both inorganic (e.g., LN) and organic (e.g., EO polymer) materials[156–159]. The Pockels effect is a linear EO phenomenon where the refractive index of a material changes linearly with an applied electric field, expressed as $\Delta n = \frac{1}{2} n_0^3 r E$, where n_0 is the initial refractive index, r is the Pockels coefficient, and E is the applied electric field. A significant advantage of the EO Pockels effect is its inherently fast modulation speed (up to hundreds of GHz), as the changes in material refractive index result from rapid alternations in the electronic distribution under an electric field, without involving slower thermal or mechanical processes. It is important to note that current research on tunable metasurfaces leveraging the EO Pockels effect primarily focuses on intensity

modulation, while a more complicated dynamic wavefront shaping has yet to be explored experimentally.

In addition to the Pockels effect, the EO Kerr effect can also be utilized to modulate the refractive index of the material. In this case, the refractive index changes quadratically with the applied electric field, described by $\Delta n = \frac{1}{2} n_0^3 K E^2$, where K is the Kerr constant. Although the Kerr effect is theoretically present in all materials, it is relatively weak and has not been widely investigated, even in simulations. Only recently have a few studies explored tunable metasurfaces based on the optical Kerr effect, utilizing metallic quantum well structures[394–397] to enhance the Kerr effect.

7.1 Electrically Tunable Metasurfaces Based on Thin-Film Inorganic Pockels Materials

Thin-film inorganic EO Pockels materials, including LN, barium titanate (BaTiO3 or BTO), aluminum nitride (AlN), and silicon-rich silicon nitride (SRN), have been used to develop electrically tunable metasurfaces when integrated with metallic[398–407] and dielectric metasurfaces[408,409], or independently patterned[410–415].

Among all these materials, LN is the most used due to its large EO coefficients, good thermal stability, wide transparency window, and recent development in high-quality thin-film LN-on-insulator (LNOI) technologies[157–159,416]. Recent research has primarily focused on integrating thin-film LN into various metasurface configurations for amplitude modulation. In 2021, Bozhevolnyi's group explored an active Fresnel lens comprising a 300 nm thick z-cut LN layer sandwiched between a thick bottom Au film and a layer of semitransparent nanostructured Au concentric rings, as illustrated in Fig. 16(a)[401]. The modulation relies on FP resonance, which can be tuned by modulating the refractive index of the LN layer ($r_{13} = 10.12$ pm V^{-1}). The focusing efficiency of the Fresnel lens is ~15% in the spectrum from 800 to 900 nm, which changed by 1.5% when a driving voltage of ± 10 V was applied. However, the large bottom electrode limits the 3 dB operation bandwidth to approximately

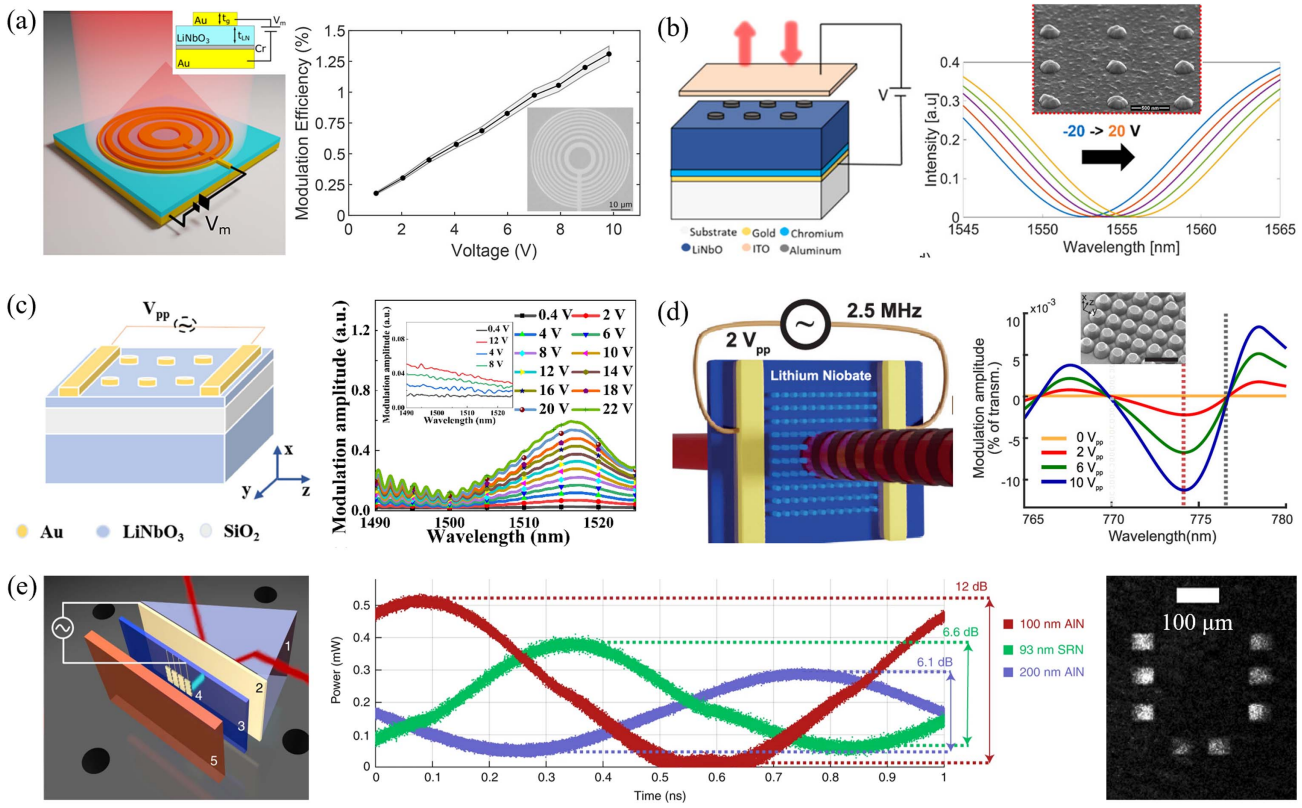

Fig. 16 Electrically tunable metasurfaces based on thin-film inorganic Pockels materials. (a) Near-infrared active Fresnel lens in reflection. Adapted with permission from Ref. [401] © ACS. (b) Reflective metasurface intensity modulator at $\lambda = 1550$ nm based on a MIM configuration. Adapted with permission from Ref. [404] © ACS. (c) Transmissive metasurface intensity modulator by tuning hybrid LSPR/FP resonances. Adapted with permission from Ref. [405] © Optical Society of America (OSA). (d) Transmissive metasurface intensity modulator with structured LN meta-atoms on a SiO_2/LN substrate. Adapted with permission from Ref. [411] © ACS. (e) Programmable plasmonic phase modulator consisting of a Si prism, an Ag thin film for surface plasmon polaritons, an EO dielectric modulation layer of SRN or AlN, and a 4 × 4 electrode matrix on a sapphire wafer, operating at $\lambda = 1550$ nm. A tunable phase shift between $[0, \pi]$ was achieved with [0 V, 18 V] applied voltages, which can be implemented for polarization contrast imaging. Adapted with permission from Ref. [399] © Springer Nature.

6.4 MHz. Using similar LN-integrated MIM configurations, with topmost Au nanostrips carefully optimized for the excitation of transverse magnetic (TM)[402] or transverse electric (TE)[406] GMRs around 900 nm, reflection modulation depths [defined as $1-R_{\min}(\lambda)/R_{\max}(\lambda)$] of 20% (with TM GMR) and 42% (with TE GMR) have been achieved with ± 10 V bias. To improve modulation efficiency, hybrid resonances have been explored for narrow and high-contrast resonance dips. In 2022, Levy's group developed an LN-integrated MIM metasurface combining three coupled resonant phenomena: LSPR, lattice resonance, and FP resonance[404]. This configuration achieved amplitude modulation with a modulation depth of 40% at a ± 25 V driving voltage, along with an absolute reflection of 80% in the telecom regime, as shown in Fig. 16(b). In addition to reflection modulation, transmission modulation has been investigated using similar configurations with metasurfaces and LN thin films, but without thick metallic reflectors. Various tunable resonances have been explored, including LSPR/FP[405], quasi-BIC[407], and GMR resonances[407]. For example, Ju *et al.* investigated transmissive metasurface modulators by designing an Au nanodisk metasurface on an LNOI substrate[405]. They achieved a tunable hybrid LSPR/FP resonance with an extinction ratio of 40% at the resonance wavelength (1480–1550 nm), demonstrating dynamic modulation at 135 MHz, as shown in Fig. 16(c). Furthermore, thin-film LN itself can also be patterned into tunable LN metasurfaces[411,415], rather than relying on LN-integrated hybrid metasurfaces. For example, Weigand *et al.* explored a transmissive EO modulator using a resonant LN metasurface[411]. The metasurface unit cell is pillar-shaped, featuring a period of 500 nm and a height of 200 nm, created from a 500 nm thick *x*-cut LN thin film on a 2 μm silicon dioxide buffer layer atop an LN substrate. Two electrodes placed on the top LN layer generate an electric field along the extraordinary axis (*z*-axis) of the LN ($r_{33} = 34\ \mathrm{pm\,V^{-1}}$), enhancing the light–matter interaction. By applying a 10 V_{pp} voltage, the transmittance at the wavelength of 774 nm was changed by 0.01%, with the measured operation bandwidth of 2.5 MHz, as shown in Fig. 16(d).

The capability of high-speed (up to GHz) EO metasurfaces was experimentally confirmed by Smolyaninov *et al.* in 2019. They achieved GHz modulation speeds with a programmable plasmonic phase modulator (PPPM) using the Kretschmann configuration, which is capable of phase-dominant, space-variant light modulation at a wavelength of 1550 nm, as illustrated in Fig. 16(e)[399]. The PPPM consists of a Brewster angle Si prism, a 48 nm Ag thin film, and a ∼100 nm thick EO dielectric active layer of SRN or AlN, with a 4×4 electrode matrix on a sapphire wafer. By leveraging the high second- and third-order nonlinear susceptibility (primarily second-order, with $r_{33} \approx 1.0\ \mathrm{pm\,V^{-1}}$ for AlN and $r_{33} \approx 0.1\ \mathrm{pm\,V^{-1}}$ for SRN) of the dielectric thin film, the surface plasmon resonance (SPR) can be tuned, achieving a tunable phase shift of up to π. However, this comes at the cost of relatively high insertion losses of up to 10 dB.

Other Pockels materials, such as BTO[400,412,413], are also explored for tunable metasurfaces. For example, one experimental work by Karvounis *et al.* combined BTO nanoparticle films (∼250 nm thick) with an Au nanowire metasurface to realize reflection modulation. However, the reflection change was rather limited, with ∼0.15% at $\lambda = 1$ μm wavelength upon an applied voltage of 4 V[400].

7.2 Electrically Tunable Metasurfaces Based on EO Polymers

Apart from inorganic materials, organic EO polymers (e.g., JRD1 and HLD) are also being explored for dynamic metasurfaces[156]. These materials leverage their high Pockels coefficients (e.g., the r_{33} of HLD is 10 times larger than that of LN) and their solution-processability, which offers greater flexibility in fabrication. It is important to note that poling is a critical process for EO polymers, as it aligns the nonlinear optical chromophores within the polymer matrix, significantly enhancing the EO coefficients.

By incorporating a subwavelength-thick EO polymer layer into a MIM configuration, where both the EO polymer and top-layer Au are structured, a GSP-like tunable metasurface can be implemented. Notably, the solution-processable spin-coating process of EO polymer, along with an easily employed reactive ion etching method[417,418], offers more flexible fabrication compared to inorganic EO materials such as LN. In 2018, Tanemura's group demonstrated a tunable MIM metasurface embedded with an EO polymer[417]. The device consists of an EO side-chain polymer layer (540 nm thick) sandwiched between two layers of Au (200 nm thick), with the top Au layer patterned to form a subwavelength grating. The in-plane FP resonance of the EO-polymer-activated MIM mode enhances modulation efficiency, resulting in a modulation depth of 1.15% (due to the relatively small r_{33} of $2.4\ \mathrm{pm\,V^{-1}}$ achieved) with ± 10 V tuning voltages at the wavelength of 1630 nm, and capable of operating at a modulation frequency of 5 MHz. Furthermore, with a similar configuration, they explored the design of strongly coupled bimodal plasmonic resonances to produce a sharp dip in reflection, thereby enhancing modulation efficiency[418,419]. In experiment[418], they achieved a high-Q resonance ($Q \approx 113$) and nearly perfect absorption (∼27 dB) at a resonant wavelength of 1650 nm. Along with an optimized poling process of the EO polymer ($r_{33} \approx 48\ \mathrm{pm\,V^{-1}}$), the modulation in reflectance was significantly enhanced, characterized by a 9.5 dB modulation depth under an applied voltage of ± 30 V, and a high modulation frequency of 1.25 GHz, as shown in Fig. 17(a).

Another configuration that features one side structured into various dielectric or metallic metasurfaces with an unstructured EO polymer in between has also been studied based on various tunable resonances. In 2021, Sun *et al.* proposed an EO-polymer- ($r_{33} = 108\ \mathrm{pm\,V^{-1}}$) integrated SiN metasurface, consisting of an Au backplane, an EO polymer (composite of PMMA and chromophore) layer (1.8 μm thick), and a thin ITO film on which a SiN grating array was patterned[420]. By tuning a high-Q (∼145) resonance within this hybrid metasurface, they achieved 1 dB modulation depth in reflectance with $V_{\mathrm{pp}} = \pm 10$ V at $\lambda = 1244$ nm, along with a modulation frequency of 10 MHz. Shortly after, they explored high-Q (∼153) resonances in a similar configuration with Si metasurfaces[421], resulting in an improved modulation depth of 4.5 dB at a 70 V bias and a 400 MHz modulation bandwidth. In another simulation work by the same group, they utilized an in-plane inversion symmetry structure within a Si nano-array to generate high-Q resonance, enhancing the EO modulation effect[422]. In the simulation, they achieved a high-Q (∼1910) resonance, and consequently a reflectance modulation up to 16 dB with a low driving voltage of ± 2 V at $\lambda = 1327$ nm. To further improve the modulation

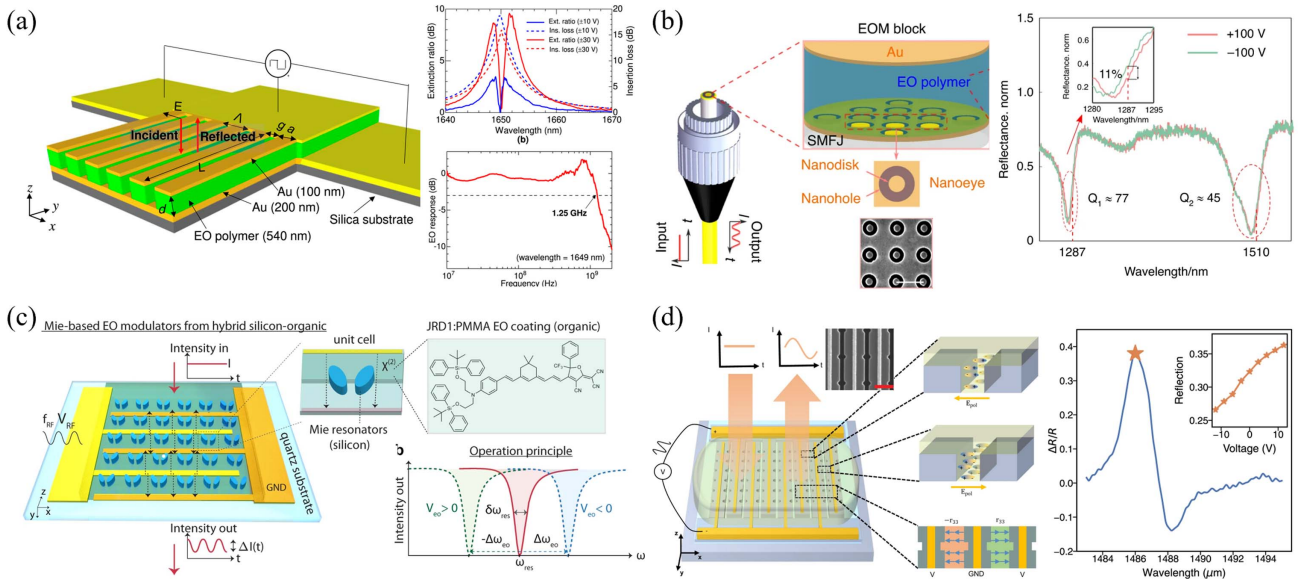

Fig. 17 Electrically tunable metasurfaces based on EO polymers. (a) Reflective EO-polymer-activated metasurface intensity modulator. Adapted with permission from Ref. [418] © AIP Publishing. (b) Plasmonic meta-fiber EO modulators with nanoeye plasmonic metasurfaces for dual-band operation. Adapted with permission from Ref. [424] © Springer Nature. (c) Hybrid Si-organic metasurfaces comprising a Mie-resonance Si metasurface layer, Au interdigitated electrode array, and JRD1 layer for high-speed intensity modulation in transmission. Adapted with permission from Ref. [426] © Springer Nature. (d) Hybrid Si-organic slot metasurfaces comprising a Si slot metasurface, Au interdigitated electrode array, and HLD layer for intensity modulation in reflection with CMOS-level voltages. Adapted with permission from Ref. [427] © Springer Nature.

efficiency, they utilized high-Q dual BIC resonances[423]. The dual BICs include symmetry-protected BIC (SP-BIC) and FP BIC, achieved through a sandwich configuration using an Au BIC metasurface ($Q \approx 203$), an EO polymer, and an Au back reflector. With this configuration, they achieved a modulation depth of 77% (with 100 V tuning voltage) at $\lambda = 1261$ nm, while the modulation speed reached nearly 100 MHz. As a step towards the direct integration of the EO metasurface modulator with fiber optics, another work in 2023 from Qiu's group explored the direct integration of the EO-polymer metasurface modulator on the end facet of a standard single-mode fiber[424]. As shown in Fig. 17(b), the EO modulator consists of an Au plasmonic metasurface layer, an EO-polymer layer (with in-device $r_{33} = 15\,\mathrm{pm\,V^{-1}}$), and an Au film, forming an FP nanocavity. The metasurface uses a nanoeye structure to sustain dual-band operation in the telecom O-band (1283 nm) and S-band (1500 nm). Experimentally, they achieved around 11% modulation depth at a bias voltage of ±9 V for both bands, along with modulation speeds up to 1 GHz.

Further improvements lie in the integration of interdigitated electrode design (providing a larger electric field with a given voltage, compared to the above-mentioned MIM configurations) with EO-polymer-activated metasurfaces hosting various high-Q resonances, including GMRs, quasi-BICs, and slot mode resonances, to achieve transmissive and reflective intensity modulation. In 2021, Capasso's group demonstrated a transmissive SLM by integrating a layer of EO organic molecules JRD1 mixed with PMMA and an Au grating on a quartz substrate, as illustrated in Fig. 17(c)[425]. The high second-order nonlinear susceptibility ($r_{33} \approx 105\,\mathrm{pm\,V^{-1}}$) of the JRD1 facilitates significant refractive index changes under an applied electric field, modulating its GMRs and enabling efficient intensity modulation. By applying ±80 V voltages, an intensity modulation ($\Delta T/T_0$) of up to 40% is achieved at the wavelength of 1400 nm. Furthermore, the demonstrated component is effective over a broad band from 1100 to 1600 nm, and the modulation frequency is up to 50 MHz. To further improve modulation efficiency and operation speed, they proposed the integration of the JRD1:PMMA layer with Mie-resonant Si metasurfaces, with two different metasurface configurations to achieve quasi-BICs and GMRs for efficient tuning[426]. In their experiment, they achieved transmittance modulation ($\Delta T/T_{\max}$) of 67% and 40% ($V_{\mathrm{switch}} = 100$ V) with respective quasi-BICs and GMRs at $\lambda \approx 1550$ nm, along with a high modulation speed characterized by a 3 dB modulation bandwidth at 3 GHz. Another experimental investigation on HLD-activated Si metasurfaces with tunable slot mode resonances has alleviated the voltage required for efficient modulation, bringing it within CMOS-level voltages. In 2024, Faraon's group explored the integration of organic EO materials (HLD, with in-device r_{33} of 45.7 $\mathrm{pm\,V^{-1}}$ at 1495 nm) within narrow gaps of high-Q slot-mode metasurfaces[427], achieving a reflectance modulation of 38% ($\Delta R/R_{\max}$) within ±17 V at telecom wavelengths, as shown in Fig. 17(d). The demonstrated 3 dB bandwidth is at 3 MHz, which has the potential improvement to GHz modulation with appropriate circuit design.

The EO nonlinear Pockels effects in LN have proven highly effective and reliable in various high-speed waveguide switches and modulators[157,159,428–432]. However, tunable metasurfaces with sub-wavelength-thin LN layers exhibit limited tuning ranges. A general solution is to design high-Q resonances to enhance light–matter interactions, which nevertheless results in tradeoffs

between bandwidth and tunability. EO polymers, which possess higher Pockels coefficients than LN, have been explored for efficient tunable metasurfaces. Yet, the implementation of EO polymers requires meticulous poling before fabrication and a crosslinking process afterward to enhance their EO activity and ensure long-term stability. Additionally, the robustness at high temperatures (>100°C) must be validated. Currently, experimental developments in tunable metasurfaces using EO Pockel materials primarily focus on uniform amplitude and phase modulation, with more complex dynamic polarization control and wavefront engineering still relatively unexplored.

8 Electrically Tunable Metasurfaces Based on MEMS and NEMS

MEMS and NEMS that integrate electronically actuate, movable components represent a cutting-edge domain in micro- and nanoscopic technologies[161,433–437]. When combined with micro-optics, this technology facilitates the development of MOEMS, which have found extensive commercial applications, including digital micromirror devices, optical switches, variable optical attenuators, tunable lasers, optical sensors, and optical phase arrays[438–441]. The functional excellence of MOEMS in manipulating light stems from their nanometer-precision movements, ranging approximately from 100 nm to 100 μm. This capability is ideally suited for optical applications, where movement precision must be significantly smaller than the wavelength, while the range of motion should be comparable to or larger than the wavelength, ensuring precise and comprehensive phase control from visible to infrared spectra. Integrating MEMS and NEMS technologies into optical metasurfaces enables dynamic actuation, offering a distinct advantage over other tunable metasurfaces that rely on active materials with limited refractive index changes modulated by external stimuli[160,162,442]. In contrast, the dynamic optical responses in MEMS- and NEMS-based metasurfaces are achieved through precise adjustments of geometric parameters, whether in-plane or out-of-plane.

8.1 MEMS/NEMS-Integrated Homogeneous Metasurfaces

Early efforts on MEMS/NENS-integrated dynamic metasurfaces primarily featured configurations with suspended metasurfaces consisting of periodically arranged homogeneous meta-atoms, whose lateral separation can be dynamically adjusted by applying an electrostatic force. Consequently, this approach uniformly alters the optical responses (e.g., reflection and transmission spectra). In 2013, Zheludev's group published a groundbreaking study on the development of an electromechanically reconfigurable plasmonic metamaterial operating in the near-infrared spectrum, which utilizes electrostatic forces to dynamically alter its optical properties, as illustrated in Fig. 18(a)[443]. The metamaterial is composed of plasmonic metamolecules arrayed on flexible SiN strings with an area of 12 μm × 35 μm. Applying a voltage to these strings caused them to move closer or further apart due to electrostatic attraction, thus modifying the transmission and reflection characteristics at near-infrared wavelengths between 1 and 2 μm. They achieved a modulation depth of approximately 8% ($\Delta R/R_{\text{off}}$ and $\Delta T/T_{\text{off}}$) at high speeds (up to 0.5 MHz). This seminal work represents a pioneering demonstration of leveraging MEMS to dynamically control plasmonic structures and their resonances, leading to reconfigurable reflection, transmission, and absorption properties. Shortly after, using a similar configuration of NEMS-integrated metasurfaces, Yamaguchi *et al.* demonstrated a transmissive optical filter with a tuning range of ~60 nm at a fast-tuning speed of 20 MHz in the visible spectrum (around 500 nm) when a bias voltage of less than 10 V was applied[444]. Besides in-plane MEMS actuation, out-of-plane MEMS actuation has also been studied for intensity modulation. For instance, a mechanically tunable metasurface comprises an α-Si nanopillar array and a suspended α-Si membrane with integrated electrostatic actuators[445]. By mechanically displacing the membrane, the device utilizes the tunable Mie-resonance-enhanced absorption within the nanopillar array to vary the reflectivity. This configuration offers a contrast ratio of 1:3, with reflectance varying from approximately 25% to 8%, over a spectral range from 400 to 530 nm, as shown in Fig. 18(b).

Besides electrostatic actuation, electrothermal actuation offers another method for implementing dynamic metasurfaces by properly designing bimorph nanostructures. Zheludev's group designed an array of zigzag-shaped nanostructures (overall size of 35 μm × 20 μm) on an Au/SiN bilayer membrane [Fig. 18(c)][446]. Each zigzag beam can be actuated for out-of-plane movement by thermally induced expansion, thereby modifying corresponding transmittances ($\Delta T/T = 50\%$) at the wavelength of 1550 nm. However, this electrothermal adjustment is relatively slow, constrained by the cooling rates of the materials. Moreover, the performance is highly dependent on the materials used, requiring careful selection and compatibility analysis of different thermal and mechanical properties.

In addition to intensity modulation, dynamic polarization control has been demonstrated. In 2018, Shimura *et al.* demonstrated adjustable linear birefringence based on a MEMS-integrated Au nanograting metasurface[447], where the birefringence arises from the different optical paths encountered by light polarized along two perpendicular axes, known as the slow and fast axes. The MEMS actuator physically deforms the nanograting, altering these paths and the corresponding birefringence. The metasurface comprises Au gratings fabricated on a glass substrate with a thin Si layer in between. By integrating ITO glass above the metasurface, it is possible to adjust the suspended Au nanograting beams up and down. This mechanical deformation enables dynamic control over the birefringence. The modulation of retardation, observed at a wavelength of 633 nm, was achieved by varying the applied voltage from 0 to 200 V, resulting in a change from 21.5° to 46.8°, as shown in Fig. 18(d).

Apart from low-Q plasmonic resonances, high-Q resonances were investigated to achieve significant amplitude and phase modulation with less intense external stimuli. For example, Faraon's group demonstrated a series of NEMS-enabled metasurfaces based on various tunable high-Q resonances, including GMRs[448], quasi-BICs[448], high-order Mie resonances[449], and slot resonance modes[450], to explore both intensity and phase modulation capabilities. For example, in 2021, they demonstrated a NEMS-enabled dynamic metasurface that hosts tunable high-Q resonances, including both GMRs and quasi-BICs[448]. The designed system requires only several volts to achieve spectral shifts of approximately 5 nm at telecom wavelengths. Impressively, it achieved an absolute intensity modulation exceeding 40% and demonstrated a phase shift of up to 144° with a 4 V bias. For more efficient phase modulation, they explored asymmetric resonant Si nanobar metasurfaces that

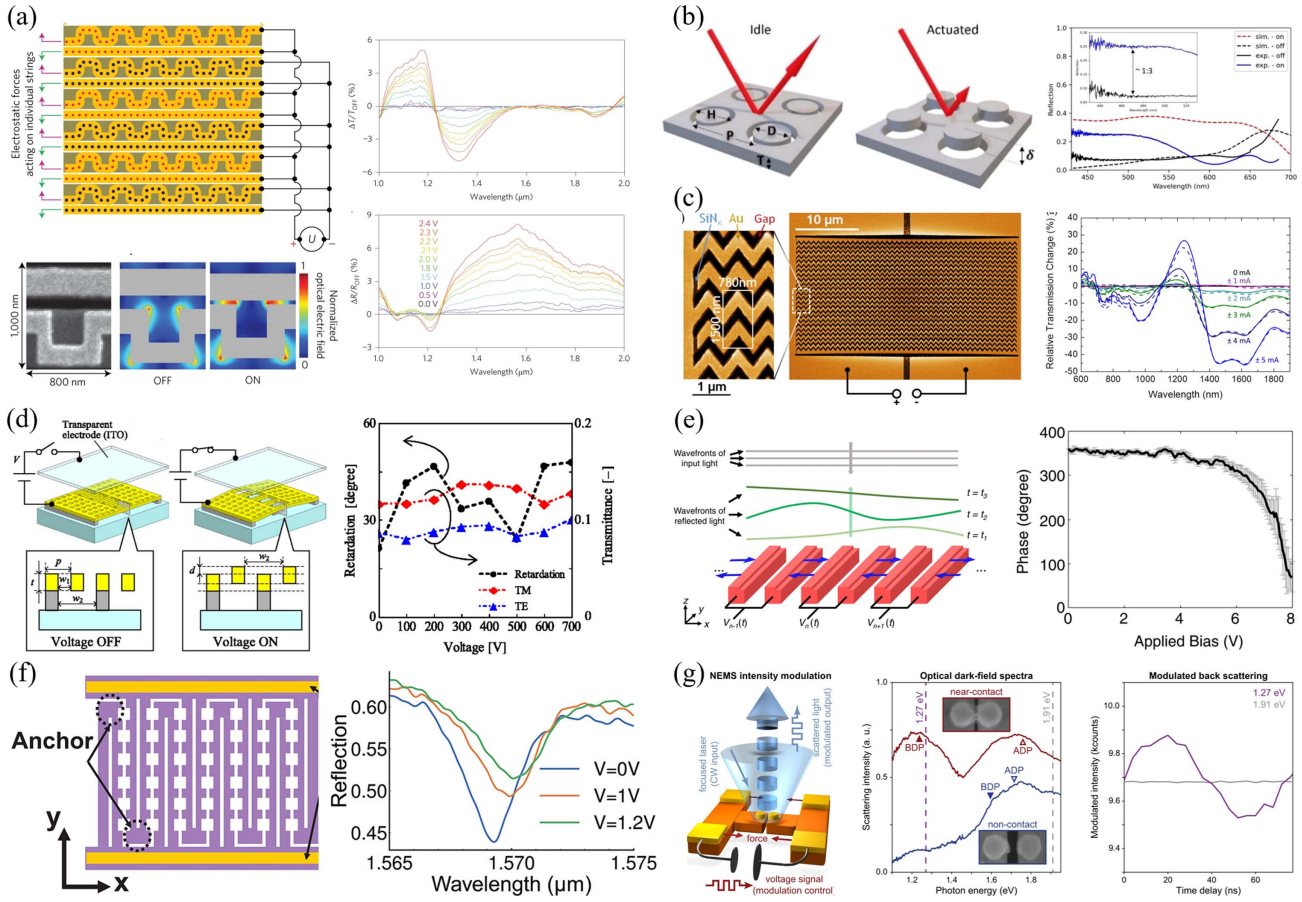

Fig. 18 MEMS/NEMS-integrated homogeneous metasurfaces. (a) Electrically reconfigurable plasmonic metamaterial for modulating reflected and transmitted telecom light using in-plane electrostatic forces between parallel strings on a flexible SiN membrane. Adapted with permission from Ref. [443] © Springer Nature. (b) Broadband tunable Si metasurfaces for intensity modulation in the visible spectrum using out-plane electrostatic forces. Adapted with permission from Ref. [445] © ACS. (c) Tunable plasmonic metasurfaces for intensity modulation at telecom wavelengths, activated by out-of-plane electrothermal actuation. Adapted with permission from Ref. [446] © AIP Publishing. (d) Birefringent reconfigurable metasurfaces for visible wavelengths utilizing MEMS-integrated Au nanogratings. Adapted with permission from Ref. [447] © AIP Publishing. (e) NEMS integrated metasurfaces for dynamic amplitude and phase modulation at telecom wavelengths with nanostructures meticulously designed for high-order Mie resonances. Adapted with permission from Ref. [449] © Springer Nature. (f) NEMS integrated metasurfaces for dynamic amplitude and phase modulation at telecom wavelengths with nanostructures meticulously designed for high-Q slot resonance modes. Adapted with permission from Ref. [450] © ACS. (g) NEMS modulation of a strongly coupled plasmonic dimer for high-speed (~10 MHz) light-intensity modulator. Adapted with permission from Ref. [452] © Springer Nature.

support perturbed high-order Mie resonances, as illustrated in Fig. 18(e). This configuration achieves a continuous-tunable phase shift up to 246° with over 50% reflectivity at a bias of 8 V at $\lambda = 1529$ nm[449], which offers the potential of a metasurface SLM with a large phase tuning range, high operation speed, and wavelength-level pixel size. Another design introduces a perturbation in the slot mode propagating between Si bars, enabling a high-Q resonance that is highly sensitive to mechanical movement[450]. By applying a voltage of ~1 V, reflection modulation of ~10% was experimentally achieved at wavelengths of around 1550 nm, as shown in Fig. 18(f). Furthermore, they employed a NEMS-based chiral metasurface to demonstrate tunable chiroptical responses associated with orthogonal CP light[451]. The setup includes two sets of Si nanostructures, each outfitted with an electrode for electrical biasing. By applying a voltage, the physical separation between these structures can be modulated, thereby altering the chiroptical properties. They demonstrated a significant change in circular dichroism (CD, $|R_{RR} - R_{LL}|$) from 0.45 to 0.01 with a tuning voltage of less than 3 V at a resonant wavelength of 1478 nm.

Individual gap-tunable NEMS-integrated coupled plasmonic dimers have also been investigated [Fig. 18(g)]; these nanodimers have extremely sensitive optical properties when they are nearly touching[452]. At sub-nanometer scales, the strong

coupling effects and quantum mechanical behaviors significantly influence the plasmonic resonance, making the system highly tunable and capable of precise control over light–matter interactions. The system demonstrated a dramatic shift in plasmonic resonance energy with minute changes in the gap, showing a sensitivity of approximately 250 meV/nm. A fabricated prototype light-intensity modulator achieved operational speeds up to 10 MHz and demonstrated energy efficiency with a power consumption of only 4 fJ/bit. Despite high tunability, low power consumption, and high-speed operation, this work involves sophisticated fabrication and control techniques, along with potential stability issues and limited scalability.

8.2 MEMS-Mirror-Integrated Dynamic Metasurfaces

The integration of MEMS/NEMS with homogeneous metasurfaces typically results in uniform amplitude/phase modulation, which makes it impossible to realize dynamic wave-shaping functions such as beam steering, switchable focusing, or the generation of versatile vortex beams with reconfigurable topological charges. Recently, by combining a MEMS mirror with a phase-gradient metasurface and modulating the separation between them, tunable phase-gradient metasurfaces with high absolute and modulation efficiencies have been achieved by exploring various tunable resonance mechanisms, including Mie/FP[453], GSP[454], or plasmonic/FP resonances[455–458]. In 2019, Brongersma's group made groundbreaking advancements in the field of dynamic wavefront shaping by developing a highly integrated, compact MEMS-based tunable phase-gradient metasurface in reflection, as illustrated in Fig. 19(a)[453]. This metasurface, fabricated within a suspended Si membrane, utilizes variable spacing between the metasurface (composed of suspended nanobeams with different widths for phase engineering) and a thick Si substrate on the backside, which enables the reconfiguration of hybrid resonances through the coupling of Mie resonances, supported by the in-plane Si antennas, and out-of-plane FP resonances, supported by both Si antennas and the backside Si substrate. Leveraging this innovative platform, the team demonstrated temporal color mixing as well as dynamic 1D beam steering and focusing within the visible spectrum from 600 to 700 nm. This system achieves complete 0-2π phase modulation over a relatively small voltage range of approximately 4 V and offers rapid operation speeds up to ~1 MHz. Although this platform can be readily expanded to incorporate other tunable phase engineering functionalities, its limitations are still evident: (1) the material is limited to Si, which can be lossy for visible wavelengths; (2) scaling up to a large aperture size is challenging; (3) it is only capable of 1D wavefront shaping.

To develop a universal platform, Bozhevolnyi's group utilized a thin-film piezoelectric MEMS mirror to create MEMS-mirror-integrated metasurfaces. In this approach, the MEMS mirror and the optical metasurface are designed and fabricated independently, thus significantly increasing the DoFs for metasurface design in terms of materials, geometries, and overall sizes. In 2021, Meng *et al.* demonstrated a dynamic phase-gradient metasurface by integrating a MEMS mirror with an Au plasmonic metasurface[454]. By precisely controlling the distance between the MEMS mirror and the plasmonic metasurface, they could switch GSP resonances on and off. This functionality enables the realization of tunable phase-gradient metasurfaces in reflection, characterized by high efficiencies (over 50%), significant modulation depth, and broadband operation around the wavelength of 800 nm. The response time, approximately 400 μs, is primarily determined by the design of the MEMS mirror and could potentially be optimized to the MHz level. As proof of concept, they demonstrated a MEMS-based metasurface grating capable of reconfiguring between the zeroth and first diffraction orders, as well as a MEMS-tunable concave mirror that could toggle between focusing and normal mirror functionalities [Fig. 19(b)]. It is important to note that this configuration achieves both a large bandwidth and high modulation depth, which are typically mutually constrained in active-material-triggered tunable metasurfaces. Achieving a larger bandwidth requires a more substantial refractive index change, which is often limited and very difficult to achieve in many active materials, making it challenging to attain larger modulation depths. In a follow-up work[455], the same group discovered that even with the distance between the plasmonic metasurface and the MEMS mirror exceeding 1 μm, thereby eliminating the presence of GSP resonances, it was still possible to achieve tunable phase-gradient metasurfaces for dynamic wavefront control. The underlying mechanism transitioned to hybrid plasmonic/FP resonances, as shown in Fig. 19(c). While this mechanism eliminates the need for an ultra-small separation between the MEMS mirror and the metasurface to activate GSP resonances, operating in this regime leads to a reduction in the operation bandwidth due to the increased FP orders.

By leveraging the design flexibility of the metasurface, the MEMS-mirror-integrated metasurface can be further developed for dynamic polarization control by incorporating anisotropic antenna arrays, which exhibit distinct optical responses to orthogonal linear polarization incidences. In one study, Meng *et al.* employed a plasmonic metasurface composed of anisotropic periodic Au nanobrick arrays (200 nm in length, 100 nm in width, and 50 nm in thickness) to demonstrate a tunable waveplate with high efficiency (>75%) and full 2π accessible birefringence at an 800 nm wavelength, as shown in Fig. 19(d)[456]. In another investigation, Deng *et al.* showcased a MEMS-based metasurface linear polarizer with a tunable extinction ratio ranging from 13.3 to 1.0 by activating the separation [Fig. 19(e)][457]. Using this tunable polarizer, they demonstrated potential applications in dynamic grayscale display and tunable vector vortex beam generation. Moreover, by integrating chiral nanostructures, the MEMS-mirror-integrated metasurface can enable topological phase transitions under an orthogonal circular polarization basis. In 2024, Ding *et al.* demonstrated MEMS-based chiral metasurfaces capable of operating between chiral exceptional points (EPs) and diabolic points (DPs) through the careful design of chiral nanostructures[458]. At the chiral EP, the entire MEMS-metasurface system is characterized by simultaneously degenerate eigenstates and eigenvalues, whereas at the DP, it exhibits degenerate eigenvalues and orthogonal eigenstates. This configuration enabled the creation of a tunable circular polarizer, capable of switching the output light between left and right circular polarizations with a voltage change as small as 0.8 V when using RCP incident light, as shown in Fig. 19(f).

From a comprehensive perspective, it is important to note that the underlying mechanism of tunable MEMS-mirror-integrated metasurfaces for efficient dynamic wavefront and polarization control can also be understood and elucidated from the viewpoint of parameter space phase singularities, which have been recently discussed by several research groups[459–469].

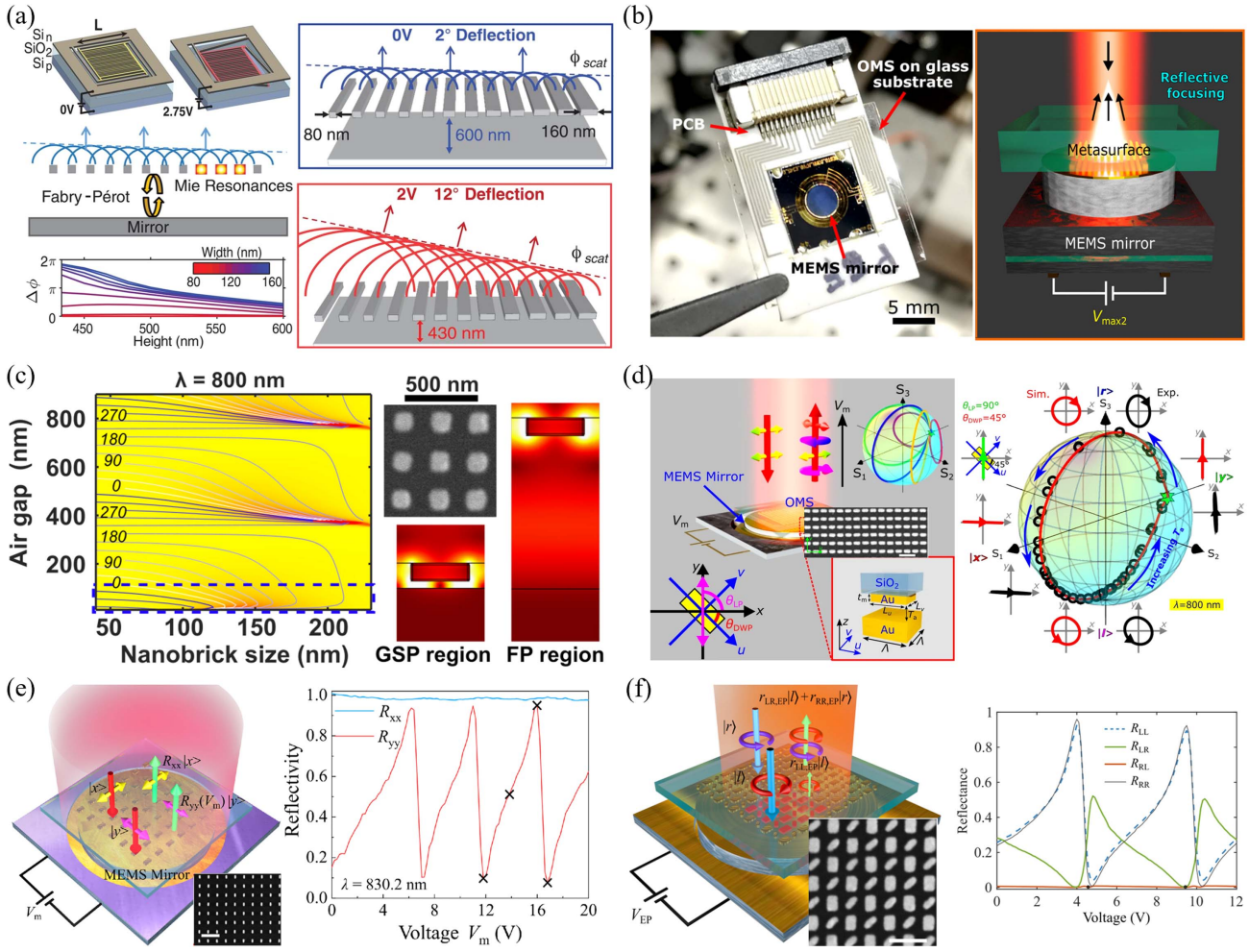

Fig. 19 MEMS-mirror-integrated dynamic metasurfaces. (a) Suspended Si metasurfaces for dynamic wavefront shaping in the visible spectrum via voltage-controlled electrostatic forces between the suspended metasurfaces and the underlying Si substrate. Adapted with permission from Ref. [453] © AAAS. (b) MEMS-mirror-integrated phase-gradient GSP metasurfaces for broadband polarization-independent dynamic wavefront shaping. Adapted with permission from Ref. [454] © AAAS. (c) MEMS-mirror-integrated plasmonic metasurfaces for dynamic wavefront shaping through tunable hybrid plasmonic/FP resonances. Adapted with permission from Ref. [455] © ACS. (d) MEMS-mirror-integrated tunable waveplate with full 2π birefringence coverage. Adapted with permission from Ref. [456] © Springer Nature. (e) MEMS-mirror-integrated tunable linear polarizer. Adapted with permission from Ref. [457] © OSA. (f) MEMS-mirror-integrated chiral metasurfaces for voltage-controllable topological phase transitions and tunable CP light filtering. Adapted with permission from Ref. [458] © AAAS.

8.3 MEMS-Tunable Metalenses

Metalenses represent a pivotal advancement in metasurface technology to revolutionize compact and lightweight imaging systems by potentially replacing conventional bulky lenses[29–31,33,34]. Recent progress in MEMS-integrated metalenses has further enhanced the capabilities of traditional metalenses, broadening their applicability in various practical imaging applications. One strategy for implementing tunable metalenses with a MEMS configuration involves transferring an as-fabricated single metasurface lens onto a MEMS structure to stretch it[470] or control its orientation[471]. In 2018, She *et al.* proposed adaptive metalenses by directly integrating (transferring) a metasurface lens onto dielectric elastomer actuators (DEAs). By applying voltages to the DEAs, an in-plane strain field can stretch or shift the metalens, thereby allowing control over its focal length, astigmatism, and shift. As shown in Fig. 20(a), they experimentally achieved a polarization-insensitive transmissive MEMS-integrated metalens with focal length tuning from 50.1 to 53.1 μm using applied voltages ranging from 0 to 1 kV, at a wavelength of 1550 nm. Furthermore, adjustments to the astigmatism and focal point shifts can also be made by applying different voltages to the electrodes to induce asymmetric in-plane strains. Although these ultracompact, electrical-controlled, adaptive metalenses showcase high efficiency and tunability, this configuration is characterized by a relatively slow speed (response time ~33 ms) limited by the viscoelasticity of the elastomer and requires high operating voltages (up to ~kV) constrained by Young's modulus and thickness

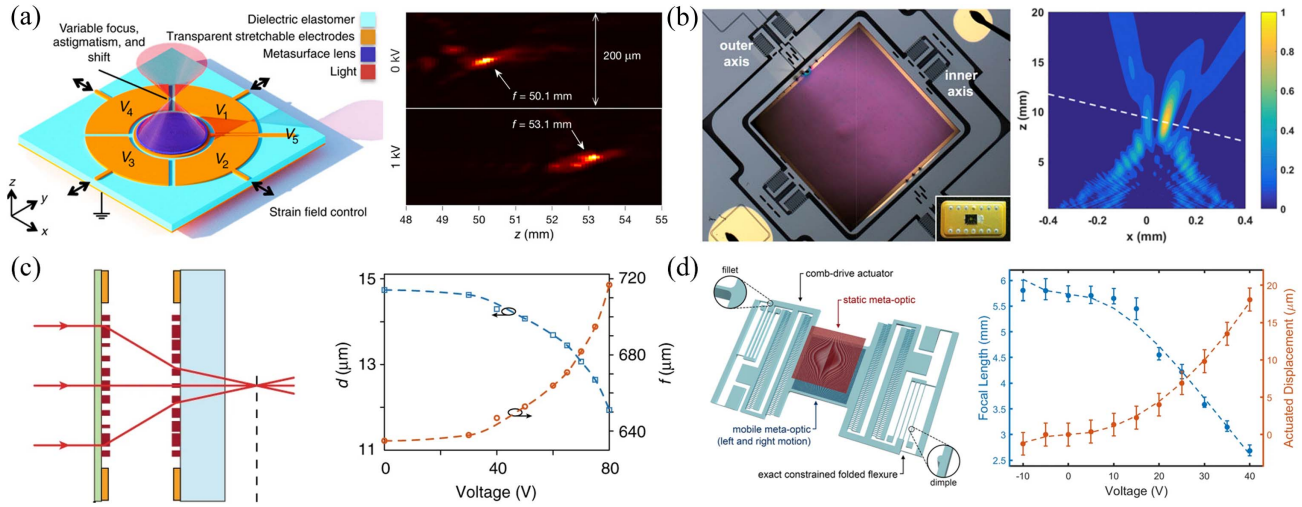

Fig. 20 MEMS-integrated tunable metalenses. (a) Transmissive silicon metasurface integrated with dielectric elastomer actuators for controlling focal length, astigmatism, and shift. Adapted with permission from Ref. [470] © AAAS. (b) Reflective plasmonic metalens directly transferred to a MEMS mirror for angled MIR focusing. Adapted with permission from Ref. [471] © AIP Publishing. (c) MEMS-tunable varifocal transmissive Si metasurface doublet with adjustable separation controlled by out-of-plane electrostatic forces between the substrates supporting the two metalenses. Adapted with permission from Ref. [472] © Springer Nature. (d) MEMS-actuated varifocal transmissive Alvarez metalens by introducing lateral displacement between two static metalenses using comb-drive actuators. Adapted with permission from Ref. [475] © Springer Nature.

of the elastomer layer in DEA configurations. To reduce the required voltages and enhance both tunability and switching speed, electrostatic or piezoelectric MEMS actuators can be utilized instead of DEAs. In 2018, Roy *et al.* demonstrated a reflective metalens mounted on an electrostatic MEMS mirror [471]. The metalens, consisting of a 50 nm Au nanodisk, a 400 nm SiO_2 layer, and a 200 nm Au film, was designed to focus light at mid-infrared wavelengths ($\lambda = 4.6$ μm) with a focusing efficiency of approximately 83%. By adjusting the MEMS mirror, the angle of the metalens can be controlled within ±9°, allowing for dynamic steering of the focused beam at an operating speed of around 1 kHz [Fig. 20(b)].

Another strategy to implement tunable metalenses involves a configuration of cascaded metasurfaces, with their longitudinal separation[472,473] or lateral shifts[474,475] precisely controlled and modulated by MEMS actuators. In 2018, Faraon's group showcased a groundbreaking integration of MEMS with dielectric metalenses to create a transmissive varifocal doublet, as illustrated in Fig. 20(c)[472]. Composed of high-index Si nanoposts, the dielectric metalens facilitates phase transmission adjustments from 0 to 2π by altering the width of the nanoposts, optimized for a design wavelength of 915 nm. One metalens was mounted on a movable MEMS membrane, while the other was affixed to a stationary fused SiO_2 substrate; the two lenses were then meticulously aligned and bonded. Electrostatic force actuation enables adjustment of the separation between these two metalenses, thereby tuning the focal length of the compound MEMS-based doublet. This adjustment achieved a significant change in the optical power of about 60 diopters by altering the metalens separation by approximately 1 μm, with operation frequencies around 4 kHz. Moreover, the study also introduced a tunable focus metasurface microscope utilizing this MEMS-tunable metalens. Most MEMS-integrated tunable metasurfaces utilize electrostatic MEMS that, although easy to implement, typically offer limited out-of-plane displacement and require relatively high voltages. In 2022, Dirdal *et al.* advanced MEMS-tunable metalenses by incorporating thin-film piezoelectric MEMS into a metalens doublet[473]. This innovation demonstrated an out-of-plane displacement of one metasurface lens up to 7.2 μm under an applied voltage of 23 V, roughly twice the displacement at a quarter of the voltage required by conventional electrostatic out-of-plane actuating MEMS metasurfaces. Utilizing this enhanced tunability, the team successfully demonstrated a varifocal metalens doublet, achieving a focal shift of approximately 250 μm at the design wavelength of 1.55 μm.

Apart from metalens doublets, the concept of Alvarez lenses was also explored as varifocal lenses[474,475]. In 2020, Han *et al.* constructed varifocal metalenses using two complementary cubic surface-profiled metalenses that shift laterally to adjust the lens's optical power[474]. The integration of the metalens with MEMS technology facilitates precise and dynamic control of the focal length through in-plane electrostatic actuation. Compatible with standard semiconductor fabrication processes, the entire metalens assembly is scalable and potentially cost-effective for mass production. The fabricated metalens operating at $\lambda = 1550$ nm achieved a focal length change of over 68 μm within an actuation range of 6.3 μm. With a nominal focal length of 216 μm, this modification corresponds to a significant 1460 diopter change in optical power. Furthermore, they demonstrated MEMS-integrated Alvarez meta-optics with a 0.5 mm aperture, utilizing flip-chip bonding to improve alignment between the meta-optic elements [Fig. 20(d)]. In this new demonstration, a substantial focal length tuning of 3.1 mm (equivalent to 200 diopters) was achieved using actuation voltages below 40 V[475].

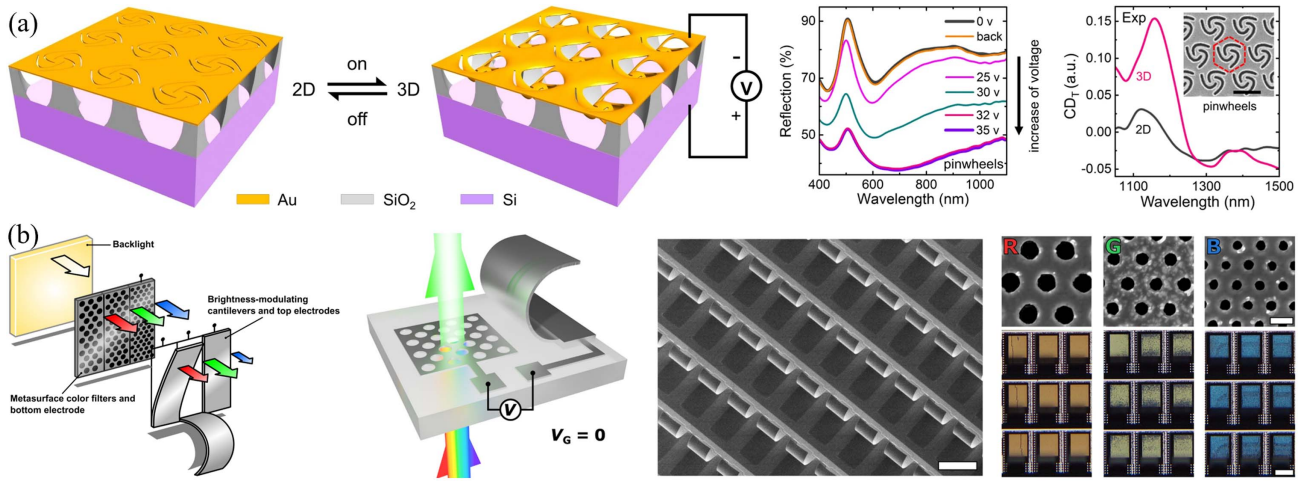

Fig. 21 MEMS-activated metasurfaces with 2D-to-3D transformations. (a) Optical nano-kirigami with pinwheel and spiral arrays for reflective intensity modulation and tunable circular dichroism. Adapted with permission from Ref. [476] © Springer Nature. (b) MEMS cantilever-controlled plasmonic color filter demonstrating dynamic plasmonic colors with adjustable transmittance, designed for sustainable optical displays. Adapted with permission from Ref. [480] © AAAS.

8.4 MEMS-Activated Metasurfaces with 2D-to-3D Transformations

Leveraging the high versatility of MEMS, it is possible to reconfigure properly designed metasurfaces between 2D and 3D configurations by applying out-of-plane electrostatic forces. This capability opens up a new design dimension for versatile light field manipulation[160], including uniform intensity[476,477] and phase[478,479] modulation, dynamic wavefront shaping[477–479], and tunable chirality[476]. In a notable example [Fig. 21(a)], Li's group demonstrated electromechanically reconfigurable optical nano-kirigami[476]. By applying voltages between the nanostructured top Au layer and the Si substrate, a 2D-to-3D transformation is achieved, modulating optical properties like reflectance and helicity at visible and near-infrared wavelengths, as depicted in Fig. 21(a). Notably, with deformable pinwheel arrays, they achieved a 50% modulation contrast [defined as $\Delta R/R(V = 0\,\mathrm{V})$] in reflection at an actuation voltage range of 0 to 35 V, at a wavelength of 750 nm. Another nano-kirigami configuration showed reconfigurable helicity in reflectance, characterized by a CP-dependent reflection spectrum.

Besides intensity/phase modulation and dynamic wavefront control, MEMS-integrated transmissive metasurfaces were used for fast-tunable spectral filter arrays, potentially motivating new-generation displays. In 2022, Han *et al.* utilized the out-of-plane movement freedom of a MEMS cantilever to achieve plasmonic colors for sustainable optical displays[480]. As shown in Fig. 21(b), this system combines a static plasmonic metasurface (Al nanohole arrays with three different sizes, acting as three transmissive bandpass filters for RGB colors) with a MEMS cantilever that controls transmittance, which can be modulated freely from 35% to 100%. The pixels can operate at around 1 kHz. This component showcases a CMOS-compatible design that is simple to fabricate for both MEMS and metasurfaces, offering advantages such as a simplified configuration, energy efficiency, and a fast refresh rate compared to state-of-the-art liquid crystal displays, which could be particularly useful in developing innovative optical displays that align with future circular economic goals.

Concluding the MEMS/NEMS-tunable metasurface section, the integration of MEMS/NEMS-actuators enables the realization of tunable metasurfaces for a range of applications, including intensity/phase modulators, tunable polarization optics, and dynamic wavefront shaping components. The design approaches are primarily based on three concepts: (1) altering the geometry of individual meta-atoms to modulate its resonance properties; (2) redefining the overall phase profiles by stretching or shifting the entire metasurfaces; (3) adjusting the overall response by modifying the relative positions of several cascaded metasurfaces. MEMS/NEMS-enabled electromechanical movements offer controllable, nanometer-scale resolution and precision, making them ideal for optical applications. Unlike tunable metasurfaces reliant on active materials, where modulation efficiency is limited by the extent of refractive index changes, MEMS/NEMS-integrated metasurfaces operate through modifications in meta-atom geometries or the overall configuration, typically yielding high modulation efficiency but at the expense of relatively slow responses. The operational speed of these devices is governed by the intrinsic resonance frequency of the MEMS structures, which generally spans from kHz to MHz bandwidth. The reliability of MEMS technology has been confirmed through the widespread commercial availability of various MEMS components. Notably, in certain configurations, especially those involving piezoelectric MEMS, hysteresis behavior is observed, necessitating the implementation of closed-loop feedback control for further advancements of MEMS-tunable meta-optics.

9 Conclusion and Perspectives

Electrically triggered optical metasurfaces represent a transformative leap in photonics, offering unprecedented control over light–matter interactions with dynamic tunability that can be exercised with existing electronic control systems. In this work,

Table 1 Comparison of Different Platforms to Realize Electrically Tunable Optical Metasurfaces.

Platform	Advantage	Disadvantage	Modulation Speed
LCs	• Compatibility with existing technologies • High resolution and precision • Low power consumption • Wide wavelength range • Flexibility	• Limited modulation speed • Temperature and environmental sensitivity • Limited tuning range • Polarization dependency	~kHz
PCMs	• Large refractive index change • Wide wavelength range • Fast modulation speed • Durability • Scalability and integration • Multi-state operation • Non-volatile tuning (PCCs)	• Non-uniform heating • Optical losses in visible • Energy consumption for large-area transitions • Complex fabrication processes	~kHz – MHz
Electrochemical materials	• Precise and reversible tuning • Large refractive index change • Low power consumption	• Slow modulation speed • Material degradation • Temperature and environmental sensitivity • Complex fabrication processes	~Hz – kHz
2D materials	• Fast modulation speed • Atomic thickness • Compatibility with existing microfabrication techniques	• Optical losses • Poor long-term stability • Challenges in large-scale integration	~GHz
TCOs	• High modulation speed • High transparency in visible • Versatility across different wavelengths • Compatibility with existing semiconductor processes	• Limited modulation depth • Optical losses • Complex fabrication processes • Material stability and degradation	~GHz
EO nonlinear materials	• High modulation speed • Low power consumption • Integration with photonic circuits • Durability	• Limited modulation depth • Optical losses • Complex fabrication processes	~GHz
MEMS/NEMS	• Large tuning range • Durability • Compatibility with existing microfabrication techniques	• Limited modulation speed • Hysteresis in piezoelectric MEMS/NEMS • Complex fabrication processes	~kHz – MHz

we have conducted a comprehensive overview of cutting-edge technologies and methodologies employed in the domain of electrically tunable optical metasurfaces. The fundamental principles of electrical modulation have been elucidated, providing a detailed consideration of various materials and mechanisms that facilitate the metasurface tunability with electrical stimuli (Table 1). Typical applications, such as tunable wavelength filters, optical modulators, dynamic beam steering, adaptive lenses, and holographic displays, have been highlighted to demonstrate the vast potential and versatility.

Despite significant progress, several challenges remain (Table 1), which include optimizing the efficiency and response time of modulation, improving the stability and durability of materials, and developing scalable fabrication techniques. Addressing these challenges is essential for implementing in practice and commercializing electrically tunable optical metasurfaces. Looking forward, the future of electrically triggered optical metasurfaces is promising, with numerous exciting avenues for research and innovation, as follows.

(1) **Advanced design methods**. Conventional metasurface design involves selecting the topologies and tuning the geometries of meta-atoms to meet the specific constraints of the intended scenarios, which is time- and resource-consuming and heavily relies on knowledge and experience. With increased information channels in multiple tuning states, this method makes it impossible to meet all criteria. In contrast to typical design standards, advanced design methods such as machine learning[481–488], deep learning[489–492], inverse design[490,491,493–496], and topology optimization[497–501] seem better equipped to boost the development of dynamic metasurfaces with enhanced efficiency, functionality, and adaptability. Machine learning enables the processing of vast datasets to uncover intricate patterns, allowing for highly accurate prediction and optimization of metasurface structures, accelerating the design process, and facilitating the discovery of novel configurations that traditional methods might overlook. Inverse design further enhances this capability by enabling designers to specify desired outcomes and use computational algorithms to determine the optimal

metasurface structures for achieving these goals, thereby streamlining the design process and expanding the range of practical applications. Topology optimization provides a systematic approach to identifying the most suitable spatial distribution of materials within a metasurface, producing highly sophisticated and efficient designs with complex, multi-functional capabilities. The synergy of these advanced design strategies presents an exciting frontier for optical metasurfaces in general and for electrically triggered tunable metasurfaces with enhanced design precision and efficiency, in particular.

(2) **Advanced materials**. Developing novel materials with enhanced EO properties, wider transparency windows, greater durability, better scalability, and compatibility with existing technological platforms (such as microelectronics), reduced fabrication costs, and improved environmental stability will be critical for electrically triggered optical metasurfaces. While emerging materials such as PCMs, 2D materials, or organic polymers show great promise, none have yet met all the necessary criteria. Thus, the quest for advanced materials remains a challenging but essential endeavor. This process typically involves a multifaceted approach that combines theoretical predictions, experimental validation, and interdisciplinary collaboration. Researchers start by identifying materials with intrinsic properties that are amenable to electrical modulation, such as high conductivity, tunable refractive index, and stability under various operating conditions. Computational methods, including density functional theory and machine learning algorithms[502,503], are employed to predict and screen potential materials from extensive databases, focusing on those with promising EO characteristics. Experimental validation follows, where selected materials undergo rigorous testing to assess their performance in practical metasurface configurations, including their response time, modulation depth, durability, and environmental stability. Significant advancements often come from hybrid materials that integrate organic and inorganic components or from novel nanofabrication techniques that enhance material properties. Effective integration of these materials into functional metasurfaces requires close collaboration among materials scientists, electrical engineers, and physicists. By combining theoretical insights with experimental innovations, the discovery and optimization of materials for tunable metasurfaces can be significantly accelerated, paving the way for new and transformative applications in photonics and beyond.

(3) **Application expansion**. The potential applications of electrically tunable optical metasurfaces extend well beyond traditional photonics, offering transformative possibilities across various fields. In medical imaging, these metasurfaces could be utilized to develop real-time imaging systems with the ability to dynamically adjust focus and contrast, thereby improving the detection and diagnosis of diseases[504–507]. For augmented reality and virtual reality, tunable metasurfaces could revolutionize the way visual information is projected and perceived, enabling lightweight, compact devices with enhanced depth perception and expanded FOV[84,208,508–512]. Additionally, tunable metasurfaces hold promise in the development of adaptive optics systems for astronomy, where they could be used to correct atmospheric distortions in real time, leading to clearer and more detailed observations of celestial objects. Furthermore, electrically triggered metasurfaces can enter the realm of quantum metaphotonics[513–516]. While current quantum metasurfaces facilitate the generation[517–528] and manipulation[529–537] of nonclassical states of light, their functionalities are largely passive and constrained by fixed material compositions and configurations. This limitation underscores the need for dynamic, or more broadly, space-time quantum metasurfaces that can continuously tune quantum light in both time and space[538]. The advancements achieved in electrically triggered metasurfaces for classical light can be extended into the quantum domain, paving the way for electrically controlled space-time quantum metasurfaces that offer unprecedented control over quantum photonic processes.

(4) **Scalability and manufacturing**. Achieving scalability and efficient manufacturing is already, as noted above, on the agenda, being essential for facilitating the transition of electrically triggered optical metasurfaces from the laboratory to widespread industrial applications. Traditional fabrication methods, such as EBL, although precise, are not compliant with large-scale production due to their high cost and time-consuming nature[539]. To address this, alternative techniques like deep-ultraviolet projection lithography[540–543], nanoimprint lithography[544–548], and roll-to-roll printing[549–552] are being explored for their ability to replicate nanoscale patterns over large areas more cost-effectively. Advanced deposition methods, such as atomic layer deposition and chemical vapor deposition, enable precise control over material properties, facilitating the integration of advanced materials like PCMs and 2D materials into scalable processes. Modular manufacturing approaches, which combine different techniques, and hybrid methods integrating additive and subtractive processes, offer flexibility in creating complex designs. Additionally, eco-friendly fabrication processes that minimize waste and energy consumption are critical for sustainable manufacturing. Collaboration between academia and industry is necessary to establish best practices and industry standards, accelerating the commercialization of these innovative metasurfaces.

While electrically triggered tunable optical metasurfaces have already demonstrated remarkable capabilities, the journey toward fully realizing their potential is ongoing[553]. Through continued innovation and interdisciplinary collaboration, these metasurfaces promise to revolutionize a wide range of technologies and applications, heralding a new era in photonic device engineering.

Acknowledgments

The work was supported by the Independent Research Fund Denmark (No. 1134-00010B) and Villum Fonden (award in Technical and Natural Sciences 2019, Nos. 37372 and 50343).

References

1. N. Shitrit *et al.*, "Optical spin Hall effects in plasmonic chains," *Nano Lett.* **11**, 2038 (2011).
2. N. Yu *et al.*, "Light propagation with phase discontinuities: generalized laws of reflection and refraction," *Science* **334**, 333 (2011).
3. L. Huang *et al.*, "Dispersionless phase discontinuities for controlling light propagation," *Nano Lett.* **12**, 5750 (2012).
4. S. Sun *et al.*, "Gradient-index meta-surfaces as a bridge linking propagating waves and surface waves," *Nat. Mater.* **11**, 426 (2012).
5. S. Sun *et al.*, "High-efficiency broadband anomalous reflection by gradient meta-surfaces," *Nano Lett.* **12**, 6223 (2012).
6. N. Yu *et al.*, "A broadband, background-free quarter-wave plate based on plasmonic metasurfaces," *Nano Lett.* **12**, 6328 (2012).

7. Y. Zhao, M. A. Belkin, and A. Alù, "Twisted optical metamaterials for planarized ultrathin broadband circular polarizers," *Nat. Commun.* **3**, 870 (2012).
8. C. Pfeiffer and A. Grbic, "Metamaterial Huygens' surfaces: tailoring wave fronts with reflectionless sheets," *Phys. Rev. Lett.* **110**, 197401 (2013).
9. X. Yin *et al.*, "Photonic spin Hall effect at metasurfaces," *Science* **339**, 1405 (2013).
10. A. V. Kildishev, A. Boltasseva, and V. M. Shalaev, "Planar photonics with metasurfaces," *Science* **339**, 1232009 (2013).
11. N. Meinzer, W. L. Barnes, and I. R. Hooper, "Plasmonic meta-atoms and metasurfaces," *Nat. Photonics* **8**, 889 (2014).
12. N. Yu and F. Capasso, "Flat optics with designer metasurfaces," *Nat. Mater.* **13**, 139 (2014).
13. H.-T. Chen, A. J. Taylor, and N. Yu, "A review of metasurfaces: physics and applications," *Rep. Prog. Phys.* **79**, 076401 (2016).
14. P. Genevet *et al.*, "Recent advances in planar optics: from plasmonic to dielectric metasurfaces," *Optica* **4**, 139 (2017).
15. H. Hsiao, C. H. Chu, and D. P. Tsai, "Fundamentals and applications of metasurfaces," *Small Methods* **1**, 1600064 (2017).
16. G. Li, S. Zhang, and T. Zentgraf, "Nonlinear photonic metasurfaces," *Nat. Rev. Mater.* **2**, 17010 (2017).
17. S. M. Choudhury *et al.*, "Material platforms for optical metasurfaces," *Nanophotonics* **7**, 959 (2018).
18. F. Ding, A. Pors, and S. I. Bozhevolnyi, "Gradient metasurfaces: a review of fundamentals and applications," *Rep. Prog. Phys.* **81**, 026401 (2018).
19. F. Ding *et al.*, "A review of gap-surface plasmon metasurfaces: fundamentals and applications," *Nanophotonics* **7**, 1129 (2018).
20. Q. He *et al.*, "High-efficiency metasurfaces: principles, realizations, and applications," *Adv. Opt. Mater.* **6**, 1800415 (2018).
21. S. M. Kamali *et al.*, "A review of dielectric optical metasurfaces for wavefront control," *Nanophotonics* **7**, 1041 (2018).
22. X. Luo, "Subwavelength optical engineering with metasurface waves," *Adv. Opt. Mater.* **6**, 1701201 (2018).
23. S. Sun *et al.*, "Electromagnetic metasurfaces: physics and applications," *Adv. Opt. Photonics* **11**, 380 (2019).
24. S. Chen *et al.*, "Metasurface-empowered optical multiplexing and multifunction," *Adv. Mater.* **32**, 1805912 (2020).
25. W. T. Chen, A. Y. Zhu, and F. Capasso, "Flat optics with dispersion-engineered metasurfaces," *Nat. Rev. Mater.* **5**, 604 (2020).
26. F. Ding, "A review of multifunctional optical gap-surface plasmon metasurfaces," *Prog. Electromagn. Res.* **174**, 55 (2022).
27. J. Yao *et al.*, "Integrated-resonant metadevices: a review," *Adv. Photonics* **5**, 024001 (2023).
28. A. I. Kuznetsov *et al.*, "Roadmap for optical metasurfaces," *ACS Photonics* **11**, 816 (2024).
29. M. Khorasaninejad and F. Capasso, "Metalenses: versatile multifunctional photonic components," *Science* **358**, eaam8100 (2017).
30. P. Lalanne and P. Chavel, "Metalenses at visible wavelengths: past, present, perspectives," *Laser Photonics Rev.* **11**, 1600295 (2017).
31. M. L. Tseng *et al.*, "Metalenses: advances and applications," *Adv. Opt. Mater.* **6**, 1800554 (2018).
32. X. Zou *et al.*, "Imaging based on metalenses," *PhotoniX* **1**, 2 (2020).
33. M. Pan *et al.*, "Dielectric metalens for miniaturized imaging systems: progress and challenges," *Light Sci. Appl.* **11**, 195 (2022).
34. T. Li *et al.*, "Revolutionary meta-imaging: from superlens to metalens," *Photonics Insights* **2**, R01 (2023).
35. P. Lalanne *et al.*, "Blazed binary subwavelength gratings with efficiencies larger than those of conventional échelette gratings," *Opt. Lett.* **23**, 1081 (1998).
36. F. Aieta *et al.*, "Aberration-free ultrathin flat lenses and axicons at telecom wavelengths based on plasmonic metasurfaces," *Nano Lett.* **12**, 4932 (2012).
37. A. Pors *et al.*, "Broadband focusing flat mirrors based on plasmonic gradient metasurfaces," *Nano Lett.* **13**, 829 (2013).
38. A. Arbabi *et al.*, "Dielectric metasurfaces for complete control of phase and polarization with subwavelength spatial resolution and high transmission," *Nat. Nanotechnol.* **10**, 937 (2015).
39. A. Arbabi *et al.*, "Subwavelength-thick lenses with high numerical apertures and large efficiency based on high-contrast transmitarrays," *Nat. Commun.* **6**, 7069 (2015).
40. M. Khorasaninejad *et al.*, "Metalenses at visible wavelengths: diffraction-limited focusing and subwavelength resolution imaging," *Science* **352**, 1190 (2016).
41. E. Arbabi *et al.*, "Controlling the sign of chromatic dispersion in diffractive optics with dielectric metasurfaces," *Optica* **4**, 625 (2017).
42. S. Wang *et al.*, "A broadband achromatic metalens in the visible," *Nat. Nanotechnol.* **13**, 227 (2018).
43. S. Shrestha *et al.*, "Broadband achromatic dielectric metalenses," *Light Sci. Appl.* **7**, 85 (2018).
44. W. T. Chen *et al.*, "A broadband achromatic metalens for focusing and imaging in the visible," *Nat. Nanotechnol.* **13**, 220 (2018).
45. Z. Li *et al.*, "Meta-optics achieves RGB-achromatic focusing for virtual reality," *Sci. Adv.* **7**, eabe4458 (2021).
46. J. Engelberg and U. Levy, "Achromatic flat lens performance limits," *Optica* **8**, 834 (2021).
47. J. Chen *et al.*, "Planar wide-angle-imaging camera enabled by metalens array," *Optica* **9**, 431 (2022).
48. C. Chen *et al.*, "Bifacial-metasurface-enabled pancake metalens with polarized space folding," *Optica* **9**, 1314 (2022).
49. T. Ellenbogen, K. Seo, and K. B. Crozier, "Chromatic plasmonic polarizers for active visible color filtering and polarimetry," *Nano Lett.* **12**, 1026 (2012).
50. W. Li *et al.*, "Circularly polarized light detection with hot electrons in chiral plasmonic metamaterials," *Nat. Commun.* **6**, 8379 (2015).
51. A. Pors, M. G. Nielsen, and S. I. Bozhevolnyi, "Plasmonic metagratings for simultaneous determination of Stokes parameters," *Optica* **2**, 716 (2015).
52. A. Shaltout *et al.*, "Photonic spin Hall effect in gap–plasmon metasurfaces for on-chip chiroptical spectroscopy," *Optica* **2**, 860 (2015).
53. W. T. Chen *et al.*, "Integrated plasmonic metasurfaces for spectropolarimetry," *Nanotechnology* **27**, 224002 (2016).
54. E. Maguid *et al.*, "Photonic spin-controlled multifunctional shared-aperture antenna array," *Science* **352**, 1202 (2016).
55. F. Ding *et al.*, "Beam-size-invariant spectropolarimeters using gap-plasmon metasurfaces," *ACS Photonics* **4**, 943 (2017).
56. E. Arbabi *et al.*, "Full-stokes imaging polarimetry using dielectric metasurfaces," *ACS Photonics* **5**, 3132 (2018).
57. M. Jung *et al.*, "Polarimetry using graphene-integrated anisotropic metasurfaces," *ACS Photonics* **5**, 4283 (2018).
58. A. Basiri *et al.*, "Nature-inspired chiral metasurfaces for circular polarization detection and full-Stokes polarimetric measurements," *Light Sci. Appl.* **8**, 78 (2019).
59. N. A. Rubin *et al.*, "Matrix Fourier optics enables a compact full-Stokes polarization camera," *Science* **365**, eaax1839 (2019).
60. L. Li *et al.*, "Monolithic full-Stokes near-infrared polarimetry with chiral plasmonic metasurface integrated graphene–silicon photodetector," *ACS Nano* **14**, 16634 (2020).
61. J. Wei *et al.*, "Mid-infrared semimetal polarization detectors with configurable polarity transition," *Nat. Photonics* **15**, 614 (2021).
62. Y. Ni *et al.*, "Computational spectropolarimetry with a tunable liquid crystal metasurface," *eLight* **2**, 23 (2022).
63. C. Chen *et al.*, "Neural network assisted high-spatial-resolution polarimetry with non-interleaved chiral metasurfaces," *Light Sci. Appl.* **12**, 288 (2023).
64. A. Zaidi *et al.*, "Metasurface-enabled single-shot and complete Mueller matrix imaging," *Nat. Photonics* **18**, 704 (2024).

65. A. Kristensen *et al.*, "Plasmonic colour generation," *Nat. Rev. Mater.* **2**, 16088 (2016).
66. M. Song *et al.*, "Colors with plasmonic nanostructures: A full-spectrum review," *Appl. Phys. Rev.* **6**, 041308 (2019).
67. S. Daqiqeh Rezaei *et al.*, "Nanophotonic structural colors," *ACS Photonics* **8**, 18 (2021).
68. R. Fu *et al.*, "Metasurface-based nanoprinting: principle, design and advances," *Opto-Electron. Sci.* **1**, 220011 (2022).
69. K. Kumar *et al.*, "Printing colour at the optical diffraction limit," *Nat. Nanotechnol.* **7**, 557 (2012).
70. S. J. Tan *et al.*, "Plasmonic color palettes for photorealistic printing with aluminum nanostructures," *Nano Lett.* **14**, 4023 (2014).
71. A. S. Roberts *et al.*, "Subwavelength plasmonic color printing protected for ambient use," *Nano Lett.* **14**, 783 (2014).
72. J. S. Clausen *et al.*, "Plasmonic metasurfaces for coloration of plastic consumer products," *Nano Lett.* **14**, 4499 (2014).
73. X. Zhu *et al.*, "Plasmonic colour laser printing," *Nat. Nanotechnol.* **11**, 325 (2016).
74. S. Sun *et al.*, "All-dielectric full-color printing with TiO_2 metasurfaces," *ACS Nano* **11**, 4445 (2017).
75. W. Yang *et al.*, "All-dielectric metasurface for high-performance structural color," *Nat. Commun.* **11**, 1864 (2020).
76. W.-J. Joo *et al.*, "Metasurface-driven OLED displays beyond 10,000 pixels per inch," *Science* **370**, 459 (2020).
77. M. Song *et al.*, "Enabling optical steganography, data storage, and encryption with plasmonic colors," *Laser Photonics Rev.* **15**, 2000343 (2021).
78. M. Song *et al.*, "Versatile full-colour nanopainting enabled by a pixelated plasmonic metasurface," *Nat. Nanotechnol.* **18**, 71 (2023).
79. H. Wang *et al.*, "Coloured vortex beams with incoherent white light illumination," *Nat. Nanotechnol.* **18**, 264 (2023).
80. W. Wan, J. Gao, and X. Yang, "Metasurface holograms for holographic imaging," *Adv. Opt. Mater.* **5**, 1700541 (2017).
81. L. Huang, S. Zhang, and T. Zentgraf, "Metasurface holography: from fundamentals to applications," *Nanophotonics* **7**, 1169 (2018).
82. Q. Jiang, G. Jin, and L. Cao, "When metasurface meets hologram: principle and advances," *Adv. Opt. Photonics* **11**, 518 (2019).
83. R. Zhao, L. Huang, and Y. Wang, "Recent advances in multi-dimensional metasurfaces holographic technologies," *PhotoniX* **1**, 20 (2020).
84. Z. Liu *et al.*, "Metasurface-enabled augmented reality display: a review," *Adv. Photonics* **5**, 034001 (2023).
85. J. C. Zhang *et al.*, "Programmable optical meta-holograms," *Nanophotonics* **13**, 1201 (2024).
86. X. Ni, A. V. Kildishev, and V. M. Shalaev, "Metasurface holograms for visible light," *Nat. Commun.* **4**, 2807 (2013).
87. L. Huang *et al.*, "Three-dimensional optical holography using a plasmonic metasurface," *Nat. Commun.* **4**, 2808 (2013).
88. W. T. Chen *et al.*, "High-efficiency broadband meta-hologram with polarization-controlled dual images," *Nano Lett.* **14**, 225 (2014).
89. G. Zheng *et al.*, "Metasurface holograms reaching 80% efficiency," *Nat. Nanotechnol.* **10**, 308 (2015).
90. D. Wen *et al.*, "Helicity multiplexed broadband metasurface holograms," *Nat. Commun.* **6**, 8241 (2015).
91. K. Huang *et al.*, "Silicon multi-meta-holograms for the broadband visible light," *Laser Photonics Rev.* **10**, 500 (2016).
92. X. Li *et al.*, "Multicolor 3D meta-holography by broadband plasmonic modulation," *Sci. Adv.* **2**, e1601102 (2016).
93. R. Zhao *et al.*, "Multichannel vectorial holographic display and encryption," *Light Sci. Appl.* **7**, 95 (2018).
94. H. Ren *et al.*, "Complex-amplitude metasurface-based orbital angular momentum holography in momentum space," *Nat. Nanotechnol.* **15**, 948 (2020).
95. F. Ding *et al.*, "Versatile polarization generation and manipulation using dielectric metasurfaces," *Laser Photonics Rev.* **14**, 2000116 (2020).
96. G. Qu *et al.*, "Reprogrammable meta-hologram for optical encryption," *Nat. Commun.* **11**, 5484 (2020).
97. Z. Li *et al.*, "Three-channel metasurfaces for simultaneous meta-holography and meta-nanoprinting: a single-cell design approach," *Laser Photonics Rev.* **14**, 2000032 (2020).
98. W. Yang *et al.*, "Dynamic bifunctional metasurfaces for holography and color display," *Adv. Mater.* **33**, 2101258 (2021).
99. Y. Eliezer *et al.*, "Suppressing meta-holographic artifacts by laser coherence tuning," *Light Sci. Appl.* **10**, 104 (2021).
100. P. Georgi *et al.*, "Optical secret sharing with cascaded metasurface holography," *Sci. Adv.* **7**, eabf9718 (2021).
101. M. Liu *et al.*, "Multifunctional metasurfaces enabled by simultaneous and independent control of phase and amplitude for orthogonal polarization states," *Light Sci. Appl.* **10**, 107 (2021).
102. X. Li *et al.*, "Time-sequential color code division multiplexing holographic display with metasurface," *Opto-Electron. Adv.* **6**, 220060 (2023).
103. Z. Liu *et al.*, "Broadband spin and angle co-multiplexed waveguide-based metasurface for six-channel crosstalk-free holographic projection," *eLight* **4**, 7 (2024).
104. C. Zhang *et al.*, "Tantalum pentoxide: a new material platform for high-performance dielectric metasurface optics in the ultraviolet and visible region," *Light Sci. Appl.* **13**, 23 (2024).
105. X. Hu *et al.*, "Metasurface-based computational imaging: a review," *Adv. Photonics* **6**, 014002 (2024).
106. A. Silva *et al.*, "Performing mathematical operations with metamaterials," *Science* **343**, 160 (2014).
107. A. Pors, M. G. Nielsen, and S. I. Bozhevolnyi, "Analog computing using reflective plasmonic metasurfaces," *Nano Lett.* **15**, 791 (2015).
108. Z. Wang *et al.*, "On-chip wavefront shaping with dielectric metasurface," *Nat. Commun.* **10**, 3547 (2019).
109. J. Zhou *et al.*, "Optical edge detection based on high-efficiency dielectric metasurface," *Proc. Natl. Acad. Sci.* **116**, 11137 (2019).
110. Y. Zhou *et al.*, "Flat optics for image differentiation," *Nat. Photonics* **14**, 316 (2020).
111. P. Zheng *et al.*, "Metasurface-based key for computational imaging encryption," *Sci. Adv.* **7**, eabg0363 (2021).
112. J. Zhou *et al.*, "Two-dimensional optical spatial differentiation and high-contrast imaging," *Natl. Sci. Rev.* **8**, nwaa176 (2021).
113. R. Wang *et al.*, "Computing metasurfaces enabled chiral edge image sensing," *iScience* **25**, 104532 (2022).
114. Z. Wang *et al.*, "Integrated photonic metasystem for image classifications at telecommunication wavelength," *Nat. Commun.* **13**, 2131 (2022).
115. A. Cordaro *et al.*, "Solving integral equations in free space with inverse-designed ultrathin optical metagratings," *Nat. Nanotechnol.* **18**, 365 (2023).
116. I. Tanriover, S. A. Dereshgi, and K. Aydin, "Metasurface enabled broadband all optical edge detection in visible frequencies," *Nat. Commun.* **14**, 6484 (2023).
117. M. Deng *et al.*, "Broadband angular spectrum differentiation using dielectric metasurfaces," *Nat. Commun.* **15**, 2237 (2024).
118. B. T. Swartz *et al.*, "Broadband and large-aperture metasurface edge encoders for incoherent infrared radiation," *Sci. Adv.* **10**, eadk0024 (2024).
119. S. Wang *et al.*, "Metalens for accelerated optoelectronic edge detection under ambient illumination," *Nano Lett.* **24**, 356 (2024).
120. H. Zheng *et al.*, "Multichannel meta-imagers for accelerating machine vision," *Nat. Nanotechnol.* **19**, 471 (2024).
121. Q. He, S. Sun, and L. Zhou, "Tunable/reconfigurable metasurfaces: physics and applications," *Research* **2019**, 1849272 (2019).

122. A. M. Shaltout, V. M. Shalaev, and M. L. Brongersma, "Spatiotemporal light control with active metasurfaces," *Science* **364**, eaat3100 (2019).
123. F. Neubrech, X. Duan, and N. Liu, "Dynamic plasmonic color generation enabled by functional materials," *Sci. Adv.* **6**, eabc2709 (2020).
124. O. A. M. Abdelraouf *et al.*, "Recent advances in tunable metasurfaces: materials, design, and applications," *ACS Nano* **16**, 13339 (2022).
125. P. Berini, "Optical beam steering using tunable metasurfaces," *ACS Photonics* **9**, 2204 (2022).
126. E. Mikheeva *et al.*, "Space and time modulations of light with metasurfaces: recent progress and future prospects," *ACS Photonics* **9**, 1458 (2022).
127. J. Yang *et al.*, "Active optical metasurfaces: comprehensive review on physics, mechanisms, and prospective applications," *Rep. Prog. Phys.* **85**, 036101 (2022).
128. T. Gu *et al.*, "Reconfigurable metasurfaces towards commercial success," *Nat. Photonics* **17**, 48 (2023).
129. P.-G. de Gennes and J. Prost, *The Physics of Liquid Crystals* (Clarendon Press, 2013).
130. M. J. Stephen and J. P. Straley, "Physics of liquid crystals," *Rev. Mod. Phys.* **46**, 617 (1974).
131. D. A. Coleman *et al.*, "Polarization-modulated smectic liquid crystal phases," *Science* **301**, 1204 (2003).
132. D. Kang *et al.*, "Liquid crystal-integrated metasurfaces for an active photonic platform," *Opto-Electron. Adv.* **7**, 230216 (2024).
133. M. Wuttig, H. Bhaskaran, and T. Taubner, "Phase-change materials for non-volatile photonic applications," *Nat. Photonics* **11**, 465 (2017).
134. F. Ding, Y. Yang, and S. I. Bozhevolnyi, "Dynamic metasurfaces using phase-change chalcogenides," *Adv. Opt. Mater.* **7**, 1801709 (2019).
135. C. Zheng *et al.*, "Enabling active nanotechnologies by phase transition: from electronics, photonics to thermotics," *Chem. Rev.* **122**, 15450 (2022).
136. B. Gholipour *et al.*, "Roadmap on chalcogenide photonics," *J. Phys. Photonics* **5**, 012501 (2023).
137. P. Prabhathan *et al.*, "Roadmap for phase change materials in photonics and beyond," *iScience* **26**, 107946 (2023).
138. Z. Fang *et al.*, "Non-volatile materials for programmable photonics," *APL Mater.* **11**, 100603 (2023).
139. M. Imada, A. Fujimori, and Y. Tokura, "Metal-insulator transitions," *Rev. Mod. Phys.* **70**, 1039 (1998).
140. K. Kalyanasundaram, "Applications of functionalized transition metal complexes in photonic and optoelectronic devices," *Coord. Chem. Rev.* **177**, 347 (1998).
141. H. Liu, J. Lu, and X. R. Wang, "Metamaterials based on the phase transition of VO_2," *Nanotechnology* **29**, 024002 (2018).
142. D. Mantione *et al.*, "Poly(3,4-ethylenedioxythiophene) (PEDOT) derivatives: innovative conductive polymers for bioelectronics," *Polymers* **9**, 354 (2017).
143. J. R. Reynolds, B. C. Thompson, and T. A. Skotheim, *Conjugated Polymers: Perspective, Theory, and New Materials* (CRC Press, 2019).
144. S. Chen and M. P. Jonsson, "Dynamic conducting polymer plasmonics and metasurfaces," *ACS Photonics* **10**, 571 (2023).
145. K. S. Novoselov *et al.*, "2D materials and van der Waals heterostructures," *Science* **353**, aac9439 (2016).
146. J. Shim *et al.*, "Electronic and optoelectronic devices based on two-dimensional materials: from fabrication to application," *Adv. Electron. Mater.* **3**, 1600364 (2017).
147. M. L. Brongersma, "The road to atomically thin metasurface optics," *Nanophotonics* **10**, 643 (2020).
148. Z. Dai *et al.*, "Artificial metaphotonics born naturally in two dimensions," *Chem. Rev.* **120**, 6197 (2020).
149. Q. Ma *et al.*, "Tunable optical properties of 2D materials and their applications," *Adv. Opt. Mater.* **9**, 2001313 (2021).
150. J. Lynch *et al.*, "Exciton resonances for atomically-thin optics," *J. Appl. Phys.* **132**, 091102 (2022).
151. C. Zeng *et al.*, "Graphene-empowered dynamic metasurfaces and metadevices," *Opto-Electron. Adv.* **5**, 200098 (2022).
152. G. V. Naik, V. M. Shalaev, and A. Boltasseva, "Alternative plasmonic materials: beyond gold and silver," *Adv. Mater.* **25**, 3264 (2013).
153. S. C. Dixon *et al.*, "n-Type doped transparent conducting binary oxides: an overview," *J. Mater. Chem. C* **4**, 6946 (2016).
154. W. Jaffray *et al.*, "Transparent conducting oxides: from all-dielectric plasmonics to a new paradigm in integrated photonics," *Adv. Opt. Photonics* **14**, 148 (2022).
155. A. X. Wang and W.-C. Hsu, "Perspective on integrated photonic devices using transparent conductive oxides: challenges and opportunities," *Appl. Phys. Lett.* **124**, 060503 (2024).
156. F. Ullah, N. Deng, and F. Qiu, "Recent progress in electro-optic polymer for ultra-fast communication," *PhotoniX* **2**, 13 (2021).
157. G. Chen *et al.*, "Advances in lithium niobate photonics: development status and perspectives," *Adv. Photonics* **4**, 034003 (2022).
158. A. Fedotova *et al.*, "Lithium niobate meta-optics," *ACS Photonics* **9**, 3745 (2022).
159. B. You *et al.*, "Lithium niobate on insulator–fundamental optoelectronic properties and photonic device prospects," *Nanophotonics* **13**, 3037 (2024).
160. S. Chen *et al.*, "Kirigami/origami: unfolding the new regime of advanced 3D microfabrication/nanofabrication with 'folding'," *Light Sci. Appl.* **9**, 75 (2020).
161. S. Chen *et al.*, "Technologies and applications of silicon-based micro-optical electromechanical systems: a brief review," *J. Semicond.* **43**, 081301 (2022).
162. Y. Zhao *et al.*, "Mechanically reconfigurable metasurfaces: fabrications and applications," *Npj Nanophotonics* **1**, 16 (2024).
163. Y. Li *et al.*, "Recent progress on structural coloration," *Photonics Insights* **3**, R03 (2024).
164. D. Franklin *et al.*, "Actively addressed single pixel full-colour plasmonic display," *Nat. Commun.* **8**, 15209 (2017).
165. Z.-W. Xie *et al.*, "Liquid-crystal tunable color filters based on aluminum metasurfaces," *Opt. Express* **25**, 30764 (2017).
166. Y. Lee *et al.*, "Electrical broad tuning of plasmonic color filter employing an asymmetric-lattice nanohole array of metasurface controlled by polarization rotator," *ACS Photonics* **4**, 1954 (2017).
167. K. Li *et al.*, "Electrically switchable structural colors based on liquid-crystal-overlaid aluminum anisotropic nanoaperture arrays," *Opt. Express* **30**, 31913 (2022).
168. A. Komar *et al.*, "Electrically tunable all-dielectric optical metasurfaces based on liquid crystals," *Appl. Phys. Lett.* **110**, 071109 (2017).
169. C. Zou *et al.*, "Electrically tunable transparent displays for visible light based on dielectric metasurfaces," *ACS Photonics* **6**, 1533 (2019).
170. C. Zou *et al.*, "Multiresponsive dielectric metasurfaces," *ACS Photonics* **8**, 1775 (2021).
171. X. Chang *et al.*, "Electrically tuned active metasurface towards metasurface-integrated liquid crystal on silicon (meta-LCoS) devices," *Opt. Express* **31**, 5378 (2023).
172. X. Chang *et al.*, "Fast-switching reconfigurable metadevice with metasurface-induced liquid crystal alignment for light modulator applications," *Opt. Mater. Express* **14**, 1094 (2024).
173. A. I. Kuznetsov *et al.*, "Optically resonant dielectric nanostructures," *Science* **354**, aag2472 (2016).
174. S.-Q. Li *et al.*, "Phase-only transmissive spatial light modulator based on tunable dielectric metasurface," *Science* **364**, 1087 (2019).
175. P. Moitra *et al.*, "Electrically tunable reflective metasurfaces with continuous and full-phase modulation for high-efficiency wavefront control at visible frequencies," *ACS Nano* **17**, 16952 (2023).

176. R. C. Devlin *et al.*, "Broadband high-efficiency dielectric metasurfaces for the visible spectrum," *Proc. Natl. Acad. Sci.* **113**, 10473 (2016).
177. R. C. Devlin *et al.*, "Arbitrary spin-to–orbital angular momentum conversion of light," *Science* **358**, 896 (2017).
178. Z. Shi *et al.*, "Single-layer metasurface with controllable multiwavelength functions," *Nano Lett.* **18**, 2420 (2018).
179. Y. Wu *et al.*, "TiO_2 metasurfaces: from visible planar photonics to photochemistry," *Sci. Adv.* **5**, eaax0939 (2019).
180. D. H. Goldstein, *Polarized Light* (CRC Press, 2017).
181. M. Sharma *et al.*, "Electrically and all-optically switchable nonlocal nonlinear metasurfaces," *Sci. Adv.* **9**, eadh2353 (2023).
182. M. V. Gorkunov *et al.*, "Superperiodic liquid-crystal metasurfaces for electrically controlled anomalous refraction," *ACS Photonics* **7**, 3096 (2020).
183. H. Chung and O. D. Miller, "Tunable metasurface inverse design for 80% switching efficiencies and 144° angular deflection," *ACS Photonics* **7**, 2236 (2020).
184. M. Bosch *et al.*, "Electrically actuated varifocal lens based on liquid-crystal-embedded dielectric metasurfaces," *Nano Lett.* **21**, 3849 (2021).
185. S. Pancharatnam, "Generalized theory of interference, and its applications: Part I. Coherent pencils," *Proc. Indian Acad. Sci.* **44**, 247 (1956).
186. M. V. Berry, "Quantal phase factors accompanying adiabatic changes," *Proc. R. Soc. Lond. Math. Phys. Sci.* **392**, 45 (1984).
187. Z. Bomzon *et al.*, "Space-variant Pancharatnam–Berry phase optical elements with computer-generated subwavelength gratings," *Opt. Lett.* **27**, 1141 (2002).
188. L. Huang *et al.*, "Broadband hybrid holographic multiplexing with geometric metasurfaces," *Adv. Mater.* **27**, 6444 (2015).
189. J. P. Balthasar Mueller *et al.*, "Metasurface polarization optics: independent phase control of arbitrary orthogonal states of polarization," *Phys. Rev. Lett.* **118**, 113901 (2017).
190. X. Xie *et al.*, "Generalized Pancharatnam-Berry phase in rotationally symmetric meta-atoms," *Phys. Rev. Lett.* **126**, 183902 (2021).
191. J. Li *et al.*, "Electrically-controlled digital metasurface device for light projection displays," *Nat. Commun.* **11**, 3574 (2020).
192. P. Yu, J. Li, and N. Liu, "Electrically tunable optical metasurfaces for dynamic polarization conversion," *Nano Lett.* **21**, 6690 (2021).
193. T. Badloe *et al.*, "Liquid crystal-powered Mie resonators for electrically tunable photorealistic color gradients and dark blacks," *Light Sci. Appl.* **11**, 118 (2022).
194. T. Guo *et al.*, "Broad-tuning, dichroic metagrating Fabry-Perot filter based on liquid crystal for spectral imaging," *Prog. Electromagn. Res.* **177**, 43 (2023).
195. C.-Y. Fan *et al.*, "Electrically modulated varifocal metalens combined with twisted nematic liquid crystals," *Opt. Express* **28**, 10609 (2020).
196. T. Badloe *et al.*, "Electrically tunable bifocal metalens with diffraction-limited focusing and imaging at visible wavelengths," *Adv. Sci.* **8**, 2102646 (2021).
197. X. Ou *et al.*, "Tunable polarization-multiplexed achromatic dielectric metalens," *Nano Lett.* **22**, 10049 (2022).
198. T. Badloe *et al.*, "Bright-field and edge-enhanced imaging using an electrically tunable dual-mode metalens," *ACS Nano* **17**, 14678 (2023).
199. I. Kim *et al.*, "Stimuli-responsive dynamic metaholographic displays with designer liquid crystal modulators," *Adv. Mater.* **32**, 2004664 (2020).
200. A. Asad *et al.*, "Spin-isolated ultraviolet-visible dynamic metaholographic displays with liquid crystal modulators," *Nanoscale Horiz.* **8**, 759 (2023).
201. Y. Yang *et al.*, "Gap-plasmon-driven spin angular momentum selection of chiral metasurfaces for intensity-tunable metaholography working at visible frequencies," *Nanophotonics* **11**, 4123 (2022).
202. C. Wan *et al.*, "Electric-driven meta-optic dynamics for simultaneous near-/far-field multiplexing display," *Adv. Funct. Mater.* **32**, 2110592 (2022).
203. J. Wang *et al.*, "Cholesteric liquid crystal-enabled electrically programmable metasurfaces for simultaneous near- and far-field displays," *Nanoscale* **14**, 17921 (2022).
204. J. Kim *et al.*, "Dynamic hyperspectral holography enabled by inverse-designed metasurfaces with oblique helicoidal cholesterics," *Adv. Mater.* **36**, 2311785 (2024).
205. Y. Hu *et al.*, "Electrically tunable multifunctional polarization-dependent metasurfaces integrated with liquid crystals in the visible region," *Nano Lett.* **21**, 4554 (2021).
206. I. Kim *et al.*, "Pixelated bifunctional metasurface-driven dynamic vectorial holographic color prints for photonic security platform," *Nat. Commun.* **12**, 3614 (2021).
207. K. Li *et al.*, "Electrically switchable, polarization-sensitive encryption based on aluminum nanoaperture arrays integrated with polymer-dispersed liquid crystals," *Nano Lett.* **21**, 7183 (2021).
208. J. Tang *et al.*, "Dynamic augmented reality display by layer-folded metasurface via electrical-driven liquid crystal," *Adv. Opt. Mater.* **10**, 2200418 (2022).
209. Y. Shi *et al.*, "Electrical-driven dynamic augmented reality by on-chip vectorial meta-display," *ACS Photonics* **11**, 2123 (2024).
210. P. Chen *et al.*, "Digitalizing self-assembled chiral superstructures for optical vortex processing," *Adv. Mater.* **30**, 1705865 (2018).
211. P. Chen *et al.*, "Liquid-crystal-mediated geometric phase: from transmissive to broadband reflective planar optics," *Adv. Mater.* **32**, 1903665 (2020).
212. S. Mansha *et al.*, "High resolution multispectral spatial light modulators based on tunable Fabry-Perot nanocavities," *Light Sci. Appl.* **11**, 141 (2022).
213. Z.-Y. Wang *et al.*, "Vectorial liquid-crystal holography," *eLight* **4**, 5 (2024).
214. X. Yin *et al.*, "Beam switching and bifocal zoom lensing using active plasmonic metasurfaces," *Light Sci. Appl.* **6**, e17016 (2017).
215. M. Zhang *et al.*, "Plasmonic metasurfaces for switchable photonic spin–orbit interactions based on phase change materials," *Adv. Sci.* **5**, 1800835 (2018).
216. J. Tian *et al.*, "Active control of anapole states by structuring the phase-change alloy $Ge_2Sb_2Te_5$," *Nat. Commun.* **10**, 396 (2019).
217. M. Y. Shalaginov *et al.*, "Reconfigurable all-dielectric metalens with diffraction-limited performance," *Nat. Commun.* **12**, 1225 (2021).
218. Q. Wang *et al.*, "Optically reconfigurable metasurfaces and photonic devices based on phase change materials," *Nat. Photonics* **10**, 60 (2016).
219. C. R. De Galarreta *et al.*, "Nonvolatile reconfigurable phase-change metadevices for beam steering in the near infrared," *Adv. Funct. Mater.* **28**, 1704993 (2018).
220. A. Leitis *et al.*, "All-dielectric programmable Huygens' metasurfaces," *Adv. Funct. Mater.* **30**, 1910259 (2020).
221. C. Ruiz De Galarreta *et al.*, "Reconfigurable multilevel control of hybrid all-dielectric phase-change metasurfaces," *Optica* **7**, 476 (2020).
222. M. N. Julian *et al.*, "Reversible optical tuning of GeSbTe phase-change metasurface spectral filters for mid-wave infrared imaging," *Optica* **7**, 746 (2020).
223. H. Liu *et al.*, "Rewritable color nanoprints in antimony trisulfide films," *Sci. Adv.* **6**, eabb7171 (2020).
224. L. Lu *et al.*, "Reversible tuning of Mie resonances in the visible spectrum," *ACS Nano* **15**, 19722 (2021).
225. K. Gao *et al.*, "Intermediate phase-change states with improved cycling durability of Sb_2S_3 by femtosecond multi-pulse laser irradiation," *Adv. Funct. Mater.* **31**, 2103327 (2021).
226. F. J. Morin, "Oxides which show a metal-to-insulator transition at the Neel temperature," *Phys. Rev. Lett.* **3**, 34 (1959).

227. Y. Cui *et al.*, "Thermochromic VO_2 for energy-efficient smart windows," *Joule* **2**, 1707 (2018).
228. S. Chen *et al.*, "Gate-controlled VO_2 phase transition for high-performance smart windows," *Sci. Adv.* **5**, eaav6815 (2019).
229. I. Olivares *et al.*, "Optical switching in hybrid VO_2/Si waveguides thermally triggered by lateral microheaters," *Opt. Express* **26**, 12387 (2018).
230. S. Cueff *et al.*, "VO_2 nanophotonics," *APL Photonics* **5**, 110901 (2020).
231. Y. Jung *et al.*, "Integrated hybrid VO_2–silicon optical memory," *ACS Photonics* **9**, 217 (2022).
232. T. Driscoll *et al.*, "Memory metamaterials," *Science* **325**, 1518 (2009).
233. N. A. Butakov *et al.*, "Broadband electrically tunable dielectric resonators using metal–insulator transitions," *ACS Photonics* **5**, 4056 (2018).
234. B. Chen *et al.*, "Electrically addressable integrated intelligent terahertz metasurface," *Sci. Adv.* **8**, eadd1296 (2022).
235. L. Liu *et al.*, "Hybrid metamaterials for electrically triggered multifunctional control," *Nat. Commun.* **7**, 13236 (2016).
236. Z. Zhu *et al.*, "Dynamically reconfigurable metadevice employing nanostructured phase-change materials," *Nano Lett.* **17**, 4881 (2017).
237. X. Wang *et al.*, "Multifunctional microelectro-opto-mechanical platform based on phase-transition materials," *Nano Lett.* **18**, 1637 (2018).
238. J. Wang *et al.*, "Flexible phase change materials for electrically-tuned active absorbers," *Small* **17**, 2101282 (2021).
239. R. Cabrera, E. Merced, and N. Sepulveda, "Performance of electro-thermally driven VO_2-based MEMS actuators," *J. Microelectromechanical Syst.* **23**, 243 (2014).
240. D. Torres *et al.*, "VO_2-based MEMS mirrors," *J. Microelectromechanical Syst.* **25**, 780 (2016).
241. Y. Kim *et al.*, "Phase modulation with electrically tunable vanadium dioxide phase-change metasurfaces," *Nano Lett.* **19**, 3961 (2019).
242. M. Proffit *et al.*, "Electrically driven reprogrammable vanadium dioxide metasurface using binary control for broadband beam steering," *ACS Appl. Mater. Interfaces* **14**, 41186 (2022).
243. S.-C. Jiang *et al.*, "Controlling the polarization state of light with a dispersion-free metastructure," *Phys. Rev. X* **4**, 021026 (2014).
244. F. Shu *et al.*, "Electrically driven tunable broadband polarization states via active metasurfaces based on joule-heat-induced phase transition of vanadium dioxide," *Laser Photonics Rev.* **15**, 2100155 (2021).
245. J. King *et al.*, "Electrically tunable VO_2–metal metasurface for mid-infrared switching, limiting and nonlinear isolation," *Nat. Photonics* **18**, 74 (2024).
246. C. Wan *et al.*, "Limiting optical diodes enabled by the phase transition of vanadium dioxide," *ACS Photonics* **5**, 2688 (2018).
247. A. Tripathi *et al.*, "Nanoscale optical nonreciprocity with nonlinear metasurfaces," *Nat. Commun.* **15**, 5077 (2024).
248. M. Cotrufo *et al.*, "Passive bias-free non-reciprocal metasurfaces based on thermally nonlinear quasi-bound states in the continuum," *Nat. Photonics* **18**, 81 (2024).
249. T. Guo *et al.*, "Durable and programmable ultrafast nanophotonic matrix of spectral pixels," *Nat. Nanotechnol.* (2024).
250. S. Abdollahramezani *et al.*, "Tunable nanophotonics enabled by chalcogenide phase-change materials," *Nanophotonics* **9**, 1189 (2020).
251. S. R. Ovshinsky, "Reversible electrical switching phenomena in disordered structures," *Phys. Rev. Lett.* **21**, 1450 (1968).
252. K. Shportko *et al.*, "Resonant bonding in crystalline phase-change materials," *Nat. Mater.* **7**, 653 (2008).
253. B. J. Eggleton, B. Luther-Davies, and K. Richardson, "Chalcogenide photonics," *Nat. Photonics* **5**, 141 (2011).
254. M. Wuttig and N. Yamada, "Phase-change materials for rewriteable data storage," *Nat. Mater.* **6**, 824 (2007).
255. D. Lencer *et al.*, "A map for phase-change materials," *Nat. Mater.* **7**, 972 (2008).
256. Y. Zhang *et al.*, "Broadband transparent optical phase change materials for high-performance nonvolatile photonics," *Nat. Commun.* **10**, 4279 (2019).
257. P. Hosseini, C. D. Wright, and H. Bhaskaran, "An optoelectronic framework enabled by low-dimensional phase-change films," *Nature* **511**, 206 (2014).
258. M. A. Kats *et al.*, "Nanometre optical coatings based on strong interference effects in highly absorbing media," *Nat. Mater.* **12**, 20 (2013).
259. C. Ríos *et al.*, "Color depth modulation and resolution in phase-change material nanodisplays," *Adv. Mater.* **28**, 4720 (2016).
260. Y. Wang *et al.*, "Electrical tuning of phase-change antennas and metasurfaces," *Nat. Nanotechnol.* **16**, 667 (2021).
261. Y. Zhang *et al.*, "Electrically reconfigurable non-volatile metasurface using low-loss optical phase-change material," *Nat. Nanotechnol.* **16**, 661 (2021).
262. S. Abdollahramezani *et al.*, "Electrically driven reprogrammable phase-change metasurface reaching 80% efficiency," *Nat. Commun.* **13**, 1696 (2022).
263. S. Abdollahramezani *et al.*, "Reconfigurable multifunctional metasurfaces employing hybrid phase-change plasmonic architecture," *Nanophotonics* **11**, 3883 (2022).
264. C. C. Popescu *et al.*, "Electrically reconfigurable phase-change transmissive metasurface," *Adv. Mater.* **36**, 2400627 (2024).
265. P. R. Subramanian and L. Kacprzak, *Binary Alloy Phase Diagrams* (ASM International, 1990).
266. W. Dong *et al.*, "Wide bandgap phase change material tuned visible photonics," *Adv. Funct. Mater.* **29**, 1806181 (2019).
267. M. Delaney *et al.*, "A new family of ultralow loss reversible phase-change materials for photonic integrated circuits: Sb_2S_3 and Sb_2Se_3," *Adv. Funct. Mater.* **30**, 2002447 (2020).
268. Z. Fang *et al.*, "Non-volatile phase-change materials for programmable photonics," *Sci. Bull.* **68**, 783 (2023).
269. K. V. Sreekanth *et al.*, "Dynamic color generation with electrically tunable thin film optical coatings," *Nano Lett.* **21**, 10070 (2021).
270. P. Prabhathan *et al.*, "Electrically tunable steganographic nano-optical coatings," *Nano Lett.* **23**, 5236 (2023).
271. Z. Fang *et al.*, "Nonvolatile phase-only transmissive spatial light modulator with electrical addressability of individual pixels," *ACS Nano* **18**, 11245 (2024).
272. C. G. Granqvist, "Electrochromics for smart windows: oxide-based thin films and devices," *Thin Solid Films* **564**, 1 (2014).
273. Y. Wang, E. L. Runnerstrom, and D. J. Milliron, "Switchable materials for smart windows," *Annu. Rev. Chem. Biomol. Eng.* **7**, 283 (2016).
274. Y. Ke *et al.*, "Smart windows: electro-, thermo-, mechano-, photochromics, and beyond," *Adv. Energy Mater.* **9**, 1902066 (2019).
275. C. Gu *et al.*, "Emerging electrochromic materials and devices for future displays," *Chem. Rev.* **122**, 14679 (2022).
276. Y. Li *et al.*, "Dynamic tuning of gap plasmon resonances using a solid-state electrochromic device," *Nano Lett.* **19**, 7988 (2019).
277. E. Hopmann and A. Y. Elezzabi, "Plasmochromic nanocavity dynamic light color switching," *Nano Lett.* **20**, 1876 (2020).
278. Z. Wang *et al.*, "Towards full-colour tunability of inorganic electrochromic devices using ultracompact Fabry–Perot nanocavities," *Nat. Commun.* **11**, 302 (2020).
279. J. Eaves-Rathert *et al.*, "Dynamic color tuning with electrochemically actuated TiO_2 metasurfaces," *Nano Lett.* **22**, 1626 (2022).
280. L. Yang *et al.*, "Rechargeable metasurfaces for dynamic color display based on a compositional and mechanical dual-altered mechanism," *Research* **2022**, 9828757 (2022).
281. E. Kovalik *et al.*, "Low-power electrochemical modulation of silicon-based metasurfaces," *ACS Photonics* **11**, 445 (2024).

282. X. Duan, S. Kamin, and N. Liu, "Dynamic plasmonic colour display," *Nat. Commun.* **8**, 14606 (2017).
283. X. Duan and N. Liu, "Scanning plasmonic color display," *ACS Nano* **12**, 8817 (2018).
284. X. Duan and N. Liu, "Magnesium for dynamic nanoplasmonics," *Acc. Chem. Res.* **52**, 1979 (2019).
285. J. Li *et al.*, "Addressable metasurfaces for dynamic holography and optical information encryption," *Sci. Adv.* **4**, eaar6768 (2018).
286. P. Yu *et al.*, "Generation of switchable singular beams with dynamic metasurfaces," *ACS Nano* **13**, 7100 (2019).
287. J. Li *et al.*, "Magnesium-based metasurfaces for dual-function switching between dynamic holography and dynamic color display," *ACS Nano* **14**, 7892 (2020).
288. M. Huang *et al.*, "Voltage-gated optics and plasmonics enabled by solid-state proton pumping," *Nat. Commun.* **10**, 5030 (2019).
289. K. Xiong *et al.*, "Switchable plasmonic metasurfaces with high chromaticity containing only abundant metals," *Nano Lett.* **17**, 7033 (2017).
290. S. Chen *et al.*, "Tunable structural color images by UV-patterned conducting polymer nanofilms on metal surfaces," *Adv. Mater.* **33**, 2102451 (2021).
291. S. Chen *et al.*, "Conductive polymer nanoantennas for dynamic organic plasmonics," *Nat. Nanotechnol.* **15**, 35 (2020).
292. A. Karki *et al.*, "Electrical tuning of plasmonic conducting polymer nanoantennas," *Adv. Mater.* **34**, 2107172 (2022).
293. S. Lee *et al.*, "Plasmonic polymer nanoantenna arrays for electrically tunable and electrode-free metasurfaces," *J. Mater. Chem. A* **11**, 21569 (2023).
294. J. Karst *et al.*, "Electrically switchable metallic polymer nanoantennas," *Science* **374**, 612 (2021).
295. J. Ratzsch *et al.*, "Electrically switchable metasurface for beam steering using PEDOT polymers," *J. Opt.* **22**, 124001 (2020).
296. Y. Lee *et al.*, "Dynamic beam control based on electrically switchable nanogratings from conducting polymers," *Nanophotonics* **12**, 2865 (2023).
297. J. Karst *et al.*, "Electro-active metaobjective from metalenses-on-demand," *Nat. Commun.* **13**, 7183 (2022).
298. J. H. Ko *et al.*, "Sub-1-volt electrically programmable optical modulator based on active Tamm plasmon," *Adv. Mater.* **36**, 2310556 (2024).
299. Z. A. Boeva and V. G. Sergeyev, "Polyaniline: synthesis, properties, and application," *Polym. Sci. Ser. C* **56**, 144 (2014).
300. C. Barbero and R. Kötz, "Nanoscale dimensional changes and optical properties of polyaniline measured by in situ spectroscopic ellipsometry," *J. Electrochem. Soc.* **141**, 859 (1994).
301. R. Kaissner *et al.*, "Electrochemically controlled metasurfaces with high-contrast switching at visible frequencies," *Sci. Adv.* **7**, eabd9450 (2021).
302. Y. R. Leroux *et al.*, "Conducting polymer electrochemical switching as an easy means for designing active plasmonic devices," *J. Am. Chem. Soc.* **127**, 16022 (2005).
303. N. Jiang, L. Shao, and J. Wang, "(Gold nanorod core)/(polyaniline shell) plasmonic switches with large plasmon shifts and modulation depths," *Adv. Mater.* **26**, 3282 (2014).
304. J.-W. Jeon *et al.*, "Electrically controlled plasmonic behavior of gold nanocube@polyaniline nanostructures: transparent plasmonic aggregates," *Chem. Mater.* **28**, 2868 (2016).
305. W. Lu, N. Jiang, and J. Wang, "Active electrochemical plasmonic switching on polyaniline-coated gold nanocrystals," *Adv. Mater.* **29**, 1604862 (2017).
306. J. Peng *et al.*, "Scalable electrochromic nanopixels using plasmonics," *Sci. Adv.* **5**, eaaw2205 (2019).
307. W. Lu *et al.*, "Electrochemical switching of plasmonic colors based on polyaniline-coated plasmonic nanocrystals," *ACS Appl. Mater. Interfaces* **12**, 17733 (2020).
308. W. Lu *et al.*, "Active Huygens' metasurface based on in-situ grown conductive polymer," *Nanophotonics* **13**, 39 (2024).
309. D. De Jong *et al.*, "Electrically switchable metallic polymer metasurface device with gel polymer electrolyte," *Nanophotonics* **12**, 1397 (2023).
310. Y. Yao *et al.*, "Broad electrical tuning of graphene-loaded plasmonic antennas," *Nano Lett.* **13**, 1257 (2013).
311. Y. Yao *et al.*, "Electrically tunable metasurface perfect absorbers for ultrathin mid-infrared optical modulators," *Nano Lett.* **14**, 6526 (2014).
312. A. Basiri *et al.*, "Ultrafast low-pump fluence all-optical modulation based on graphene-metal hybrid metasurfaces," *Light Sci. Appl.* **11**, 102 (2022).
313. N. Dabidian *et al.*, "Electrical switching of infrared light using graphene integration with plasmonic Fano resonant metasurfaces," *ACS Photonics* **2**, 216 (2015).
314. N. Dabidian *et al.*, "Experimental demonstration of phase modulation and motion sensing using graphene-integrated metasurfaces," *Nano Lett.* **16**, 3607 (2016).
315. M. C. Sherrott *et al.*, "Experimental demonstration of >230° phase modulation in gate-tunable graphene–gold reconfigurable mid-infrared metasurfaces," *Nano Lett.* **17**, 3027 (2017).
316. W. Luo *et al.*, "Electrically switchable and tunable infrared light modulator based on functional graphene metasurface," *Nanophotonics* **12**, 1797 (2023).
317. M. D. Feinstein and E. Almeida, "Hybridization of graphene-gold plasmons for active control of mid-infrared radiation," *Sci. Rep.* **14**, 6733 (2024).
318. Z. Cai and Y. Liu, "Near-infrared reflection modulation through electrical tuning of hybrid graphene metasurfaces," *Adv. Opt. Mater.* **10**, 2102135 (2022).
319. C. Shi, I. J. Luxmoore, and G. R. Nash, "Gate tunable graphene-integrated metasurface modulator for mid-infrared beam steering," *Opt. Express* **27**, 14577 (2019).
320. Z. Sun, F. Huang, and Y. Fu, "Graphene-based active metasurface with more than 330° phase tunability operating at mid-infrared spectrum," *Carbon* **173**, 512 (2021).
321. X. Chen *et al.*, "Electrically tunable absorber based on a graphene integrated lithium niobate resonant metasurface," *Opt. Express* **29**, 32796 (2021).
322. R. Kumari *et al.*, "Tunable Van der Waal's optical metasurfaces (VOMs) for biosensing of multiple analytes," *Opt. Express* **29**, 25800 (2021).
323. S. Kim *et al.*, "Electronically tunable extraordinary optical transmission in graphene plasmonic ribbons coupled to subwavelength metallic slit arrays," *Nat. Commun.* **7**, 12323 (2016).
324. Z. H. Chen *et al.*, "Tunable metamaterial-induced transparency with gate-controlled on-chip graphene metasurface," *Opt. Express* **24**, 29216 (2016).
325. S. Han *et al.*, "Complete complex amplitude modulation with electronically tunable graphene plasmonic metamolecules," *ACS Nano* **14**, 1166 (2020).
326. Q. Wu *et al.*, "Dual-parameter controlled reconfigurable metasurface for enhanced terahertz beamforming via inverse design method," *Phys. Scr.* **99**, 065517 (2024).
327. F. Han *et al.*, "Tunable mid-infrared multi-resonant graphene-metal hybrid metasurfaces," *Adv. Opt. Mater.* **12**, 2303085 (2024).
328. M. Jablan, H. Buljan, and M. Soljacic, "Plasmonics in graphene at infrared frequencies," *Phys. Rev. B* **80**, 245435 (2009).
329. L. Ju *et al.*, "Graphene plasmonics for tunable terahertz metamaterials," *Nat. Nanotechnol.* **6**, 630 (2011).
330. F. H. L. Koppens, D. E. Chang, and F. Javier Garcia de Abajo, "Graphene plasmonics: a platform for strong light-matter interactions," *Nano Lett.* **11**, 3370 (2011).
331. Z. Fei *et al.*, "Gate-tuning of graphene plasmons revealed by infrared nano-imaging," *Nature* **487**, 82 (2012).
332. A. N. Grigorenko, M. Polini, and K. S. Novoselov, "Graphene plasmonics," *Nat. Photonics* **6**, 749 (2012).

333. T. Low and P. Avouris, "Graphene plasmonics for terahertz to mid-infrared applications," *ACS Nano* **8**, 1086 (2014).
334. P. A. Huidobro *et al.*, "Graphene as a tunable anisotropic or isotropic plasmonic metasurface," *ACS Nano* **10**, 5499 (2016).
335. Z. Fang *et al.*, "Gated tunability and hybridization of localized plasmons in nanostructured graphene," *ACS Nano* **7**, 2388 (2013).
336. Z. Fang *et al.*, "Active tunable absorption enhancement with graphene nanodisk arrays," *Nano Lett.* **14**, 299 (2014).
337. Z. Li *et al.*, "Graphene plasmonic metasurfaces to steer infrared light," *Sci. Rep.* **5**, 12423 (2015).
338. Z. Miao *et al.*, "Widely tunable terahertz phase modulation with gate-controlled graphene metasurfaces," *Phys. Rev. X* **5**, 041027 (2015).
339. H. Cheng *et al.*, "Dynamically tunable broadband infrared anomalous refraction based on graphene metasurfaces," *Adv. Opt. Mater.* **3**, 1744 (2015).
340. P. C. Wu, N. Papasimakis, and D. P. Tsai, "Self-affine graphene metasurfaces for tunable broadband absorption," *Phys. Rev. Appl.* **6**, 044019 (2016).
341. C. Wang *et al.*, "Dynamically tunable deep subwavelength high-order anomalous reflection using graphene metasurfaces," *Adv. Opt. Mater.* **6**, 1701047 (2018).
342. N. Mou *et al.*, "Hybridization-induced broadband terahertz wave absorption with graphene metasurfaces," *Opt. Express* **26**, 11728 (2018).
343. Q. Xing *et al.*, "Tunable graphene split-ring resonators," *Phys. Rev. Appl.* **13**, 041006 (2020).
344. D. Chen *et al.*, "Tunable polarization-preserving vortex beam generator based on diagonal cross-shaped graphene structures at terahertz frequency," *Adv. Opt. Mater.* **11**, 2300182 (2023).
345. H. Park *et al.*, "Electrically tunable THz graphene metasurface wave retarders," *Nanophotonics* **12**, 2553 (2023).
346. S. Wei *et al.*, "A varifocal graphene metalens for broadband zoom imaging covering the entire visible region," *ACS Nano* **15**, 4769 (2021).
347. Q. Hu *et al.*, "Graphene metapixels for dynamically switchable structural color," *ACS Nano* **15**, 8930 (2021).
348. J. Van De Groep *et al.*, "Exciton resonance tuning of an atomically thin lens," *Nat. Photonics* **14**, 426 (2020).
349. M. Li *et al.*, "Excitonic beam steering in an active van der Waals metasurface," *Nano Lett.* **23**, 2771 (2023).
350. X. Huang *et al.*, "Black phosphorus carbide as a tunable anisotropic plasmonic metasurface," *ACS Photonics* **5**, 3116 (2018).
351. M. C. Sherrott *et al.*, "Anisotropic quantum well electro-optics in few-layer black phosphorus," *Nano Lett.* **19**, 269 (2019).
352. S. Biswas *et al.*, "Broadband electro-optic polarization conversion with atomically thin black phosphorus," *Science* **374**, 448 (2021).
353. H. Mohammadi Dinani and H. Mosallaei, "Active tunable pulse shaping using MoS2-assisted all-dielectric metasurface," *Adv. Photonics Res.* **4**, 2200207 (2023).
354. H.-T. Chen *et al.*, "Active terahertz metamaterial devices," *Nature* **444**, 597 (2006).
355. K. Y. Lee *et al.*, "Multiple p-n junction subwavelength gratings for transmission-mode electro-optic modulators," *Sci. Rep.* **7**, 46508 (2017).
356. P. P. Iyer *et al.*, "III–V heterojunction platform for electrically reconfigurable dielectric metasurfaces," *ACS Photonics* **6**, 1345 (2019).
357. M. M. Salary, S. Farazi, and H. Mosallaei, "A dynamically modulated all-dielectric metasurface doublet for directional harmonic generation and manipulation in transmission," *Adv. Opt. Mater.* **7**, 1900843 (2019).
358. A. Forouzmand and H. Mosallaei, "A tunable semiconductor-based transmissive metasurface: dynamic phase control with high transmission level," *Laser Photonics Rev.* **14**, 1900353 (2020).
359. H. U. Chae *et al.*, "GaAs mid-IR electrically tunable metasurfaces," *Nano Lett.* **24**, 2581 (2024).
360. J. Park *et al.*, "Electrically tunable epsilon-near-zero (ENZ) metafilm absorbers," *Sci. Rep.* **5**, 15754 (2015).
361. T. Bhowmik *et al.*, "Dual-band electro-optic modulator based on tunable broadband metamaterial absorber," *Opt. Laser Technol.* **161**, 109129 (2023).
362. T. Bhowmik, A. K. Chowdhary, and D. Sikdar, "Polarization- and angle-insensitive tunable metasurface for electro-optic modulation," *IEEE Photonics Technol. Lett.* **35**, 879 (2023).
363. J. Park *et al.*, "Dynamic reflection phase and polarization control in metasurfaces," *Nano Lett.* **17**, 407 (2017).
364. A. Cala Lesina *et al.*, "Tunable plasmonic metasurfaces for optical phased arrays," *IEEE J. Sel. Top. Quantum Electron.* **27**, 1 (2021).
365. P. C. Wu *et al.*, "Near-infrared active metasurface for dynamic polarization conversion," *Adv. Opt. Mater.* **9**, 2100230 (2021).
366. M. R. Eskandari, M. Ali Shameli, and R. Safian, "Analysis of an electrically reconfigurable metasurface for manipulating polarization of near-infrared light," *J. Opt. Soc. Am. B* **39**, 145 (2022).
367. T. Bhowmik, J. Gupta, and D. Sikdar, "Electro-tunable metasurface for tri-state dynamic polarization switching at near-infrared wavelengths," *J. Phys. Condens. Matter* **35**, 395701 (2023).
368. Y.-W. Huang *et al.*, "Gate-tunable conducting oxide metasurfaces," *Nano Lett.* **16**, 5319 (2016).
369. G. K. Shirmanesh *et al.*, "Electro-optically tunable multifunctional metasurfaces," *ACS Nano* **14**, 6912 (2020).
370. J. Zhang *et al.*, "Gate-tunable optical filter based on conducting oxide metasurface heterostructure," *Opt. Lett.* **44**, 3653 (2019).
371. Y. Lee *et al.*, "High-speed transmission control in gate-tunable metasurfaces using hybrid plasmonic waveguide mode," *Adv. Opt. Mater.* **8**, 2001256 (2020).
372. Z. T. Xie *et al.*, "Tunable electro- and all-optical switch based on epsilon-near-zero metasurface," *IEEE Photonics J.* **12**, 4501510 (2020).
373. A. Forouzmand and H. Mosallaei, "Tunable two dimensional optical beam steering with reconfigurable indium tin oxide plasmonic reflectarray metasurface," *J. Opt.* **18**, 125003 (2016).
374. S. I. Kim *et al.*, "Two-dimensional beam steering with tunable metasurface in infrared regime," *Nanophotonics* **11**, 2719 (2022).
375. R. Sokhoyan *et al.*, "Electrically tunable conducting oxide metasurfaces for high power applications," *Nanophotonics* **12**, 239 (2023).
376. J. Kim *et al.*, "Dynamic control of nanocavities with tunable metal oxides," *Nano Lett.* **18**, 740 (2018).
377. A. Forouzmand and H. Mosallaei, "Real-time controllable and multifunctional metasurfaces utilizing indium tin oxide materials: a phased array perspective," *IEEE Trans. Nanotechnol.* **16**, 296 (2017).
378. C. A. Riedel *et al.*, "Nanoscale modeling of electro-plasmonic tunable devices for modulators and metasurfaces," *Opt. Express* **25**, 10031 (2017).
379. Y. Lee *et al.*, "Electrically tunable multifunctional metasurface for integrating phase and amplitude modulation based on hyperbolic metamaterial substrate," *Opt. Express* **26**, 32063 (2018).
380. Z. Wang, P. Zhou, and G. Zheng, "Electrically switchable highly efficient epsilon-near-zero metasurfaces absorber with broadband response," *Results Phys.* **14**, 102376 (2019).
381. J. Hwang and J. W. Roh, "Electrically tunable two-dimensional metasurfaces at near-infrared wavelengths," *Opt. Express* **25**, 25071 (2017).
382. A. Nemati *et al.*, "Ultra-high extinction-ratio light modulation by electrically tunable metasurface using dual epsilon-near-zero resonances," *Opto-Electron. Adv.* **4**, 200088 (2021).
383. T. Bhowmik and D. Sikdar, "Electrically tunable metasurface for dual-band spatial light modulation using the epsilon-near-zero effect," *Opt. Lett.* **47**, 4993 (2022).

384. S. J. Kim and M. L. Brongersma, "Active flat optics using a guided mode resonance," *Opt. Lett.* **42**, 5 (2017).
385. W. Ma *et al.*, "Active quasi-BIC metasurfaces assisted by epsilon-near-zero materials," *Opt. Express* **31**, 13125 (2023).
386. A. Forouzmand *et al.*, "A tunable multigate indium-tin-oxide-assisted all-dielectric metasurface," *Adv. Opt. Mater.* **6**, 1701275 (2018).
387. A. Forouzmand *et al.*, "Tunable all-dielectric metasurface for phase modulation of the reflected and transmitted light via permittivity tuning of indium tin oxide," *Nanophotonics* **8**, 415 (2019).
388. A. Forouzmand and H. Mosallaei, "Electro-optical amplitude and phase modulators based on tunable guided-mode resonance effect," *ACS Photonics* **6**, 2860 (2019).
389. A. Forouzmand and H. Mosallaei, "Tunable dual-band amplitude modulation with a double epsilon-near-zero metasurface," *J. Opt.* **22**, 094001 (2020).
390. R. Sabri, A. Forouzmand, and H. Mosallaei, "Multi-wavelength voltage-coded metasurface based on indium tin oxide: independently and dynamically controllable near-infrared multichannels," *Opt. Express* **28**, 3464 (2020).
391. R. Sabri, M. M. Salary, and H. Mosallaei, "Broadband continuous beam-steering with time-modulated metasurfaces in the near-infrared spectral regime," *APL Photonics* **6**, 086109 (2021).
392. G. Kafaie Shirmanesh *et al.*, "Dual-gated active metasurface at 1550 nm with wide (>300°) phase tunability," *Nano Lett.* **18**, 2957 (2018).
393. J. Park *et al.*, "All-solid-state spatial light modulator with independent phase and amplitude control for three-dimensional LiDAR applications," *Nat. Nanotechnol.* **16**, 69 (2021).
394. Y. Xiao, H. Qian, and Z. Liu, "Nonlinear metasurface based on giant optical Kerr response of gold quantum wells," *ACS Photonics* **5**, 1654 (2018).
395. J. Zhou *et al.*, "Kerr metasurface enabled by metallic quantum wells," *Nano Lett.* **21**, 330 (2021).
396. D. Li *et al.*, "Ultrafast tunable scattering of optical antennas driven by metallic quantum wells," *ACS Photonics* **9**, 2346 (2022).
397. H. Ma *et al.*, "Tunable metasurface based on plasmonic quasi bound state in the continuum driven by metallic quantum wells," *Adv. Opt. Mater.* **11**, 2202584 (2023).
398. L. Bibbò *et al.*, "Tunable narrowband antireflection optical filter with a metasurface," *Photonics Res.* **5**, 500 (2017).
399. A. Smolyaninov *et al.*, "Programmable plasmonic phase modulation of free-space wavefronts at gigahertz rates," *Nat. Photonics* **13**, 431 (2019).
400. A. Karvounis *et al.*, "Electro-optic metasurfaces based on barium titanate nanoparticle films," *Adv. Opt. Mater.* **8**, 2000623 (2020).
401. C. Damgaard-Carstensen *et al.*, "Electrical tuning of Fresnel lens in reflection," *ACS Photonics* **8**, 1576 (2021).
402. C. Damgaard-Carstensen, M. Thomaschewski, and S. I. Bozhevolnyi, "Electro-optic metasurface-based free-space modulators," *Nanoscale* **14**, 11407 (2022).
403. A. Hoblos *et al.*, "Low driving voltage lithium niobate metasurface electro-optical modulator operating in free space," *Opt. Express* **30**, 48103 (2022).
404. A. Weiss *et al.*, "Tunable metasurface using thin-film lithium niobate in the telecom regime," *ACS Photonics* **9**, 605 (2022).
405. Y. Ju *et al.*, "Hybrid resonance metasurface for a lithium niobate electro-optical modulator," *Opt. Lett.* **47**, 5905 (2022).
406. C. Damgaard-Carstensen and S. I. Bozhevolnyi, "Nonlocal electro-optic metasurfaces for free-space light modulation," *Nanophotonics* **12**, 2953 (2023).
407. Y. Ju *et al.*, "The electro-optic spatial light modulator of lithium niobate metasurface based on plasmonic quasi-bound states in the continuum," *Nanoscale* **15**, 13965 (2023).
408. D. Barton, M. Lawrence, and J. Dionne, "Wavefront shaping and modulation with resonant electro-optic phase gradient metasurfaces," *Appl. Phys. Lett.* **118**, 071104 (2021).
409. L. Wang and I. Shadrivov, "Electro-optic metasurfaces," *Opt. Express* **30**, 35361 (2022).
410. H. Xia, Z. Li, and C. Chen, "Toroidal dipole Fano resonances driven by bound states in the continuum of lithium niobate metasurface for efficient electro-optic modulation," *Opt. Commun.* **554**, 130178 (2024).
411. H. Weigand *et al.*, "Enhanced electro-optic modulation in resonant metasurfaces of lithium niobate," *ACS Photonics* **8**, 3004 (2021).
412. N. Xu *et al.*, "Electrically-driven zoom metalens based on dynamically controlling the Phase of barium titanate (BTO) column antennas," *Nanomaterials* **11**, 729 (2021).
413. T. Naeem *et al.*, "Engineering tunability through electro-optic effects to manifest a multifunctional metadevice," *RSC Adv.* **11**, 13220 (2021).
414. Y. Xu *et al.*, "Quasi-BIC based low-voltage phase modulation on lithium niobite metasurface," *IEEE Photonics Technol. Lett.* **34**, 1077 (2022).
415. Y. Ju *et al.*, "Polarization independent lithium niobate electro-optic modulator based on guided mode resonance," *Opt. Mater.* **148**, 114928 (2024).
416. D. N. Nikogosyan, *Nonlinear Optical Crystals: A Complete Survey* (Springer-Science, 2005).
417. J. Zhang *et al.*, "Electrical tuning of metal-insulator-metal metasurface with electro-optic polymer," *Appl. Phys. Lett.* **113**, 231102 (2018).
418. J. Zhang *et al.*, "High-speed metasurface modulator using perfectly absorptive bimodal plasmonic resonance," *APL Photonics* **8**, 121304 (2023).
419. J. Zhang *et al.*, "Active metasurface modulator with electro-optic polymer using bimodal plasmonic resonance," *Opt. Express* **25**, 30304 (2017).
420. X. Sun *et al.*, "Electro-optic polymer and silicon nitride hybrid spatial light modulators based on a metasurface," *Opt. Express* **29**, 25543 (2021).
421. X. Sun and F. Qiu, "Polarization independent high-speed spatial modulators based on an electro-optic polymer and silicon hybrid metasurface," *Photonics Res.* **10**, 2893 (2022).
422. X. Sun *et al.*, "Design and theoretical characterization of high speed metasurface modulators based on electro-optic polymer," *Opt. Express* **29**, 9207 (2021).
423. X. Sun *et al.*, "Manipulating dual bound states in the continuum for efficient spatial light modulator," *Nano Lett.* **22**, 9982 (2022).
424. L. Zhang *et al.*, "Plasmonic metafibers electro-optic modulators," *Light Sci. Appl.* **12**, 198 (2023).
425. I.-C. Benea-Chelmus *et al.*, "Electro-optic spatial light modulator from an engineered organic layer," *Nat. Commun.* **12**, 5928 (2021).
426. I.-C. Benea-Chelmus *et al.*, "Gigahertz free-space electro-optic modulators based on Mie resonances," *Nat. Commun.* **13**, 3170 (2022).
427. T. Zheng *et al.*, "Dynamic light manipulation via silicon-organic slot metasurfaces," *Nat. Commun.* **15**, 1557 (2024).
428. E. L. Wooten *et al.*, "A review of lithium niobate modulators for fiber-optic communications systems," *IEEE J. Sel. Top. Quantum Electron.* **6**, 69 (2000).
429. G. Poberaj *et al.*, "Lithium niobate on insulator (LNOI) for micro-photonic devices," *Laser Photonics Rev.* **6**, 488 (2012).
430. C. Wang *et al.*, "Integrated lithium niobate electro-optic modulators operating at CMOS-compatible voltages," *Nature* **562**, 101 (2018).
431. M. He *et al.*, "High-performance hybrid silicon and lithium niobate Mach-Zehnder modulators for 100 Gbit/s and beyond," *Nat. Photonics* **13**, 359 (2019).

432. D. Zhu *et al.*, "Integrated photonics on thin-film lithium niobate," *Adv. Opt. Photonics* **13**, 242 (2021).
433. W. P. Eaton and J. H. Smith, "Micromachined pressure sensors: review and recent developments," *Smart Mater. Struct.* **6**, 530 (1997).
434. J. W. Judy, "Microelectromechanical systems (MEMS): fabrication, design and applications," *Smart Mater. Struct.* **10**, 1115 (2001).
435. S. Trolier-McKinstry and P. Muralt, "Thin film piezoelectrics for MEMS," *J. Electroceramics* **12**, 7 (2004).
436. K. L. Ekinci and M. L. Roukes, "Nanoelectromechanical systems," *Rev. Sci. Instrum.* **76**, 061101 (2005).
437. R. Bogue, "Recent developments in MEMS sensors: a review of applications, markets and technologies," *Sens. Rev.* **33**, 300 (2013).
438. C. J. Chang-Hasnain and W. Yang, "High-contrast gratings for integrated optoelectronics," *Adv. Opt. Photonics* **4**, 379 (2012).
439. A. G. Krause *et al.*, "A high-resolution microchip optomechanical accelerometer," *Nat. Photonics* **6**, 768 (2012).
440. S. T. S. Holmstrom, U. Baran, and H. Urey, "MEMS laser scanners: a review," *J. Microelectromechanical Syst.* **23**, 259 (2014).
441. B.-W. Yoo *et al.*, "A 32 × 32 optical phased array using polysilicon sub-wavelength high-contrast-grating mirrors," *Opt. Express* **22**, 19029 (2014).
442. Z. Ren *et al.*, "Leveraging of MEMS technologies for optical metamaterials applications," *Adv. Opt. Mater.* **8**, 1900653 (2020).
443. J.-Y. Ou *et al.*, "An electromechanically reconfigurable plasmonic metamaterial operating in the near-infrared," *Nat. Nanotechnol.* **8**, 252 (2013).
444. K. Yamaguchi *et al.*, "Electrically driven plasmon chip: active plasmon filter," *Appl. Phys. Express* **7**, 012201 (2014).
445. D. Herle *et al.*, "Broadband mechanically tunable metasurface reflectivity modulator in the visible spectrum," *ACS Photonics* **10**, 1882 (2023).
446. J. Valente *et al.*, "Reconfiguring photonic metamaterials with currents and magnetic fields," *Appl. Phys. Lett.* **106**, 111905 (2015).
447. T. Shimura *et al.*, "Birefringent reconfigurable metasurface at visible wavelengths by MEMS nanograting," *Appl. Phys. Lett.* **113**, 171905 (2018).
448. H. Kwon, T. Zheng, and A. Faraon, "Nano-electromechanical tuning of dual-mode resonant dielectric metasurfaces for dynamic amplitude and phase modulation," *Nano Lett.* **21**, 2817 (2021).
449. H. Kwon, T. Zheng, and A. Faraon, "Nano-electromechanical spatial light modulator enabled by asymmetric resonant dielectric metasurfaces," *Nat. Commun.* **13**, 5811 (2022).
450. T. Zheng, H. Kwon, and A. Faraon, "Nanoelectromechanical tuning of high-Q slot metasurfaces," *Nano Lett.* **23**, 5588 (2023).
451. H. Kwon and A. Faraon, "NEMS-tunable dielectric chiral metasurfaces," *ACS Photonics* **8**, 2980 (2021).
452. J.-H. Song *et al.*, "Nanoelectromechanical modulation of a strongly-coupled plasmonic dimer," *Nat. Commun.* **12**, 48 (2021).
453. A. L. Holsteen, A. F. Cihan, and M. L. Brongersma, "Temporal color mixing and dynamic beam shaping with silicon metasurfaces," *Science* **365**, 257 (2019).
454. C. Meng *et al.*, "Dynamic piezoelectric MEMS-based optical metasurfaces," *Sci. Adv.* **7**, eabg5639 (2021).
455. P. C. V. Thrane *et al.*, "MEMS tunable metasurfaces based on gap plasmon or Fabry–Pérot resonances," *Nano Lett.* **22**, 6951 (2022).
456. C. Meng *et al.*, "Full-range birefringence control with piezoelectric MEMS-based metasurfaces," *Nat. Commun.* **13**, 2071 (2022).
457. Y. Deng *et al.*, "MEMS-integrated metasurfaces for dynamic linear polarizers," *Optica* **11**, 326 (2024).
458. F. Ding *et al.*, "Electrically tunable topological phase transition in non-Hermitian optical MEMS metasurfaces," *Sci. Adv.* **10**, eadl4661 (2024).
459. F. Monticone *et al.*, "Trapping light in plain sight: embedded photonic eigenstates in zero-index metamaterials," *Laser Photonics Rev.* **12**, 1700220 (2018).
460. A. Berkhout and A. F. Koenderink, "Perfect absorption and phase singularities in plasmon antenna array etalons," *ACS Photonics* **6**, 2917 (2019).
461. A. Krasnok *et al.*, "Anomalies in light scattering," *Adv. Opt. Photonics* **11**, 892 (2019).
462. M. Liu *et al.*, "Evolution and nonreciprocity of loss-induced topological phase singularity pairs," *Phys. Rev. Lett.* **127**, 266101 (2021).
463. Z. Sakotic *et al.*, "Topological scattering singularities and embedded eigenstates for polarization control and sensing applications," *Photonics Res.* **9**, 1310 (2021).
464. R. Colom *et al.*, "Crossing of the branch cut: the topological origin of a universal 2π-phase retardation in non-Hermitian metasurfaces," *Laser Photonics Rev.* **17**, 2200976 (2023).
465. M. Elsawy *et al.*, "Universal active metasurfaces for ultimate wavefront molding by manipulating the reflection singularities," *Laser Photonics Rev.* **17**, 2200880 (2023).
466. C. Guo *et al.*, "Singular topology of scattering matrices," *Phys. Rev. B* **108**, 155418 (2023).
467. M. Liu *et al.*, "Spectral phase singularity and topological behavior in perfect absorption," *Phys. Rev. B* **107**, L241403 (2023).
468. E. Mikheeva *et al.*, "Asymmetric phase modulation of light with parity-symmetry broken metasurfaces," *Optica* **10**, 1287 (2023).
469. Z. Sakotic *et al.*, "Non-Hermitian control of topological scattering singularities emerging from bound states in the continuum," *Laser Photonics Rev.* **17**, 2200308 (2023).
470. A. She *et al.*, "Adaptive metalenses with simultaneous electrical control of focal length, astigmatism, and shift," *Sci. Adv.* **4**, eaap9957 (2018).
471. T. Roy *et al.*, "Dynamic metasurface lens based on MEMS technology," *APL Photonics* **3**, 021302 (2018).
472. E. Arbabi *et al.*, "MEMS-tunable dielectric metasurface lens," *Nat. Commun.* **9**, 812 (2018).
473. C. A. Dirdal *et al.*, "MEMS-tunable dielectric metasurface lens using thin-film PZT for large displacements at low voltages," *Opt. Lett.* **47**, 1049 (2022).
474. Z. Han *et al.*, "MEMS-actuated metasurface Alvarez lens," *Microsyst. Nanoeng.* **6**, 79 (2020).
475. Z. Han *et al.*, "Millimeter-scale focal length tuning with MEMS-integrated meta-optics employing high-throughput fabrication," *Sci. Rep.* **12**, 5385 (2022).
476. S. Chen *et al.*, "Electromechanically reconfigurable optical nano-kirigami," *Nat. Commun.* **12**, 1299 (2021).
477. X. Hong *et al.*, "Manipulation of fractal nano-kirigami by capillary and electrostatic forces," *Adv. Opt. Mater.* **11**, 2202150 (2023).
478. Y. Han *et al.*, "Reprogrammable optical metasurfaces by electromechanical reconfiguration," *Opt. Express* **29**, 30751 (2021).
479. X. Liu *et al.*, "Reconfigurable plasmonic nanoslits and tuneable Pancharatnam-Berry geometric phase based on electromechanical nano-kirigami [Invited]," *Opt. Mater. Express* **11**, 3381 (2021).
480. Z. Han *et al.*, "MEMS cantilever–controlled plasmonic colors for sustainable optical displays," *Sci. Adv.* **8**, eabn0889 (2022).
481. J. Lu and J. Vučković, "Nanophotonic computational design," *Opt. Express* **21**, 13351 (2013).
482. K. Yao, R. Unni, and Y. Zheng, "Intelligent nanophotonics: merging photonics and artificial intelligence at the nanoscale," *Nanophotonics* **8**, 339 (2019).
483. Z. A. Kudyshev, V. M. Shalaev, and A. Boltasseva, "Machine learning for integrated quantum photonics," *ACS Photonics* **8**, 34 (2021).

484. Z. Liu *et al.*, "Tackling photonic inverse design with machine learning," *Adv. Sci.* **8**, 2002923 (2021).
485. Z. A. Kudyshev *et al.*, "Machine learning-assisted global optimization of photonic devices," *Nanophotonics* **10**, 371 (2020).
486. S. Krasikov *et al.*, "Intelligent metaphotonics empowered by machine learning," *Opto-Electron. Adv.* **5**, 210147 (2022).
487. M. K. Chen *et al.*, "Artificial intelligence in meta-optics," *Chem. Rev.* **122**, 15356 (2022).
488. J.-F. Masson, J. S. Biggins, and E. Ringe, "Machine learning for nanoplasmonics," *Nat. Nanotechnol.* **18**, 111 (2023).
489. I. Malkiel *et al.*, "Plasmonic nanostructure design and characterization via deep learning," *Light Sci. Appl.* **7**, 60 (2018).
490. S. So *et al.*, "Deep learning enabled inverse design in nanophotonics," *Nanophotonics* **9**, 1041 (2020).
491. P. R. Wiecha *et al.*, "Deep learning in nano-photonics: inverse design and beyond," *Photonics Res.* **9**, B182 (2021).
492. W. Ma *et al.*, "Deep learning for the design of photonic structures," *Nat. Photonics* **15**, 77 (2021).
493. S. Molesky *et al.*, "Inverse design in nanophotonics," *Nat. Photonics* **12**, 659 (2018).
494. Z. Liu *et al.*, "Generative model for the inverse design of metasurfaces," *Nano Lett.* **18**, 6570 (2018).
495. N. Wang *et al.*, "Intelligent designs in nanophotonics: from optimization towards inverse creation," *PhotoniX* **2**, 22 (2021).
496. Z. Li *et al.*, "Empowering metasurfaces with inverse design: principles and applications," *ACS Photonics* **9**, 2178 (2022).
497. Z. Lin *et al.*, "Topology-optimized multilayered metaoptics," *Phys. Rev. Appl.* **9**, 044030 (2018).
498. Z. Lin *et al.*, "Topology optimization of freeform large-area metasurfaces," *Opt. Express* **27**, 15765 (2019).
499. J. S. Jensen and O. Sigmund, "Topology optimization for nano-photonics," *Laser Photonics Rev.* **5**, 308 (2011).
500. R. E. Christiansen and O. Sigmund, "Inverse design in photonics by topology optimization: tutorial," *J. Opt. Soc. Am. B* **38**, 496 (2021).
501. T. Phan *et al.*, "High-efficiency, large-area, topology-optimized metasurfaces," *Light Sci. Appl.* **8**, 48 (2019).
502. R. Ramprasad *et al.*, "Machine learning in materials informatics: recent applications and prospects," *Npj Comput. Mater.* **3**, 54 (2017).
503. G. L. W. Hart *et al.*, "Machine learning for alloys," *Nat. Rev. Mater.* **6**, 730 (2021).
504. S. Zhang *et al.*, "Metasurfaces for biomedical applications: imaging and sensing from a nanophotonics perspective," *Nanophotonics* **10**, 259 (2021).
505. Z. Li *et al.*, "Metasurfaces for bioelectronics and healthcare," *Nat. Electron.* **4**, 382 (2021).
506. Y. Luo *et al.*, "Metasurface-based abrupt autofocusing beam for biomedical applications," *Small Methods* **6**, 2101228 (2022).
507. M. Pahlevaninezhad *et al.*, "Metasurface-based bijective illumination collection imaging provides high-resolution tomography in three dimensions," *Nat. Photonics* **16**, 203 (2022).
508. G.-Y. Lee *et al.*, "Metasurface eyepiece for augmented reality," *Nat. Commun.* **9**, 4562 (2018).
509. S. Lan *et al.*, "Metasurfaces for near-eye augmented reality," *ACS Photonics* **6**, 864 (2019).
510. J. Xiong *et al.*, "Augmented reality and virtual reality displays: emerging technologies and future perspectives," *Light Sci. Appl.* **10**, 216 (2021).
511. Y. Shi *et al.*, "Augmented reality enabled by on-chip meta-holography multiplexing," *Laser Photonics Rev.* **16**, 2100638 (2022).
512. W.-J. Joo and M. L. Brongersma, "Creating the ultimate virtual reality display," *Science* **377**, 1376 (2022).
513. A. S. Solntsev, G. S. Agarwal, and Y. S. Kivshar, "Metasurfaces for quantum photonics," *Nat. Photonics* **15**, 327 (2021).
514. F. Ding and S. I. Bozhevolnyi, "Advances in quantum meta-optics," *Mater. Today* **71**, 63 (2023).
515. J. Ma *et al.*, "Engineering quantum light sources with flat optics," *Adv. Mater.* **36**, 2313589 (2024).
516. J. Zhang and Y. Kivshar, "Quantum metaphotonics: Recent advances and perspective," *APL Quantum* **1**, 020902 (2024).
517. N. Somaschi *et al.*, "Near-optimal single-photon sources in the solid state," *Nat. Photonics* **10**, 340 (2016).
518. S. K. H. Andersen, S. Kumar, and S. I. Bozhevolnyi, "Ultrabright linearly polarized photon generation from a nitrogen vacancy center in a nanocube dimer antenna," *Nano Lett.* **17**, 3889 (2017).
519. T. T. Tran *et al.*, "Deterministic coupling of quantum emitters in 2D materials to plasmonic nanocavity arrays," *Nano Lett.* **17**, 2634 (2017).
520. S. I. Bogdanov *et al.*, "Ultrabright room-temperature sub-nanosecond emission from single nitrogen-vacancy centers coupled to nanopatch antennas," *Nano Lett.* **18**, 4837 (2018).
521. Y. Chen *et al.*, "Highly-efficient extraction of entangled photons from quantum dots using a broadband optical antenna," *Nat. Commun.* **9**, 2994 (2018).
522. J. Liu *et al.*, "A solid-state source of strongly entangled photon pairs with high brightness and indistinguishability," *Nat. Nanotechnol.* **14**, 586 (2019).
523. Y. Kan *et al.*, "Metasurface-enabled generation of circularly polarized single photons," *Adv. Mater.* **32**, 1907832 (2020).
524. C. Wu *et al.*, "Room-temperature on-chip orbital angular momentum single-photon sources," *Sci. Adv.* **8**, eabk3075 (2022).
525. G. Marino *et al.*, "Spontaneous photon-pair generation from a dielectric nanoantenna," *Optica* **6**, 1416 (2019).
526. L. Li *et al.*, "Metalens-array–based high-dimensional and multiphoton quantum source," *Science* **368**, 1487 (2020).
527. T. Santiago-Cruz *et al.*, "Photon pairs from resonant metasurfaces," *Nano Lett.* **21**, 4423 (2021).
528. J. Zhang *et al.*, "Spatially entangled photon pairs from lithium niobate nonlocal metasurfaces," *Sci. Adv.* **8**, eabq4240 (2022).
529. T. Stav *et al.*, "Quantum entanglement of the spin and orbital angular momentum of photons using metamaterials," *Science* **361**, 1101 (2018).
530. K. Wang *et al.*, "Quantum metasurface for multiphoton interference and state reconstruction," *Science* **361**, 1104 (2018).
531. P. Georgi *et al.*, "Metasurface interferometry toward quantum sensors," *Light Sci. Appl.* **8**, 70 (2019).
532. Q. Li *et al.*, "A non-unitary metasurface enables continuous control of quantum photon–photon interactions from bosonic to fermionic," *Nat. Photonics* **15**, 267 (2021).
533. Y.-J. Gao *et al.*, "Multichannel distribution and transformation of entangled photons with dielectric metasurfaces," *Phys. Rev. Lett.* **129**, 023601 (2022).
534. Z.-X. Li *et al.*, "High-dimensional entanglement generation based on a Pancharatnam–Berry phase metasurface," *Photonics Res.* **10**, 2702 (2022).
535. D. Zhang *et al.*, "All-optical modulation of quantum states by nonlinear metasurface," *Light Sci. Appl.* **11**, 58 (2022).
536. M. Wang *et al.*, "Characterization of orbital angular momentum quantum states empowered by metasurfaces," *Nano Lett.* **23**, 3921 (2023).
537. D. Komisar *et al.*, "Multiple channelling single-photon emission with scattering holography designed metasurfaces," *Nat. Commun.* **14**, 6253 (2023).
538. W. J. M. Kort-Kamp, A. K. Azad, and D. A. R. Dalvit, "Space-time quantum metasurfaces," *Phys. Rev. Lett.* **127**, 043603 (2021).
539. B. Leng *et al.*, "Meta-device: advanced manufacturing," *Light Adv. Manuf.* **5**, 117 (2024).
540. J.-S. Park *et al.*, "All-glass, large metalens at visible wavelength using deep-ultraviolet projection lithography," *Nano Lett.* **19**, 8673 (2019).

541. T. Hu *et al.*, "CMOS-compatible a-Si metalenses on a 12-inch glass wafer for fingerprint imaging," *Nanophotonics* **9**, 823 (2020).
542. L. Zhang *et al.*, "High-efficiency, 80 mm aperture metalens telescope," *Nano Lett.* **23**, 51 (2023).
543. J.-S. Park *et al.*, "All-glass 100 mm diameter visible metalens for imaging the Cosmos," *ACS Nano* **18**, 3187 (2024).
544. G. Yoon *et al.*, "Single-step manufacturing of hierarchical dielectric metalens in the visible," *Nat. Commun.* **11**, 2268 (2020).
545. G. Yoon *et al.*, "Printable nanocomposite metalens for high-contrast near-infrared imaging," *ACS Nano* **15**, 698 (2021).
546. V. J. Einck *et al.*, "Scalable nanoimprint lithography process for manufacturing visible metasurfaces composed of high aspect ratio TiO_2 meta-atoms," *ACS Photonics* **8**, 2400 (2021).
547. M. K. Chen *et al.*, "Chiral-magic angle of nanoimprint metadevice," *Nanophotonics* **12**, 2479 (2023).
548. J. Kim *et al.*, "Scalable manufacturing of high-index atomic layer–polymer hybrid metasurfaces for metaphotonics in the visible," *Nat. Mater.* **22**, 474 (2023).
549. E. Højlund-Nielsen *et al.*, "Plasmonic colors: toward mass production of metasurfaces," *Adv. Mater. Technol.* **1**, 1600054 (2016).
550. S. Murthy *et al.*, "Plasmonic color metasurfaces fabricated by a high speed roll-to-roll method," *Nanoscale* **9**, 14280 (2017).
551. Y. Zhai *et al.*, "Scalable-manufactured randomized glass-polymer hybrid metamaterial for daytime radiative cooling," *Science* **355**, 1062 (2017).
552. K.-T. Lin *et al.*, "Highly efficient flexible structured metasurface by roll-to-roll printing for diurnal radiative cooling," *eLight* **3**, 22 (2023).
553. C. Jung, E. Lee, and J. Rho, "The rise of electrically tunable metasurfaces," *Sci. Adv.* **10**, eado8964 (2024).